2010

Numerical modeling of free surface and rapid solidification for simulation and analysis of melt spinning

Chunbai Wang
Iowa State University

Recommended Citation

Wang, Chunbai, "Numerical modeling of free surface and rapid solidification for simulation and analysis of melt spinning" (2010). *Graduate Theses and Dissertations*. 11460.
https://lib.dr.iastate.edu/etd/11460

Numerical modeling of free surface and rapid solidification for simulation and analysis of melt spinning

by

Chunbai Wang

A dissertation submitted to the graduate faculty
in partial fulfillment of the requirements for the degree of
DOCTOR OF PHILOSOPHY

Major: Engineering Mechanics

Program of Study Committee:
Ambar K. Mitra, Major Professor
Hui Hu
Matthew J. Kramer
Ron M. Nelson
Tom I. Shih

Iowa State University
Ames, Iowa
2010

DEDICATION

to

my parents for their love, support, and encouragement.

TABLE OF CONTENTS

LIST OF FIGURES

LIST OF TABLES

NOMENCLATURE

Lower Case

a	immersed length in interfacial cell; base of water column in the broken dam problem
b	immersed length in interfacial cell; opening height of sluice gate; empirical constant in the Vogel-Fucher-Tammann approximation for dynamic viscosity
c	color function; weight parameter
d	diameter; weight parameter
e	enthalpy; sensible heat; internal energy per unit volume
f	source/sink rate of $\mathbf{A}$ in the conservation equation; shape factor; nondimensional stream function in the boundary layer theory
g	weight function; gravity constant
$\vec{g}$	the gravitational acceleration 981 cm/s^2 or 9.81 m/s^2
h	height; height function; thickness of thin layer across free surface; characteristic length, in cm, m, or $inch$; grid cell size; heat transfer coefficient, in W/m^2K; Planck's constant 6.626068×10^{-34} m^2kg/s
i, j	unit vectors of two orthogonal axes of 2D coordinate system
k	the Boltzmann constant $1.3806505 \times 10^{-23}$ J/K; thermal conductivity; convolution kernel function
n	normal vector; two components of normal vector; total number of nuclei formed in control volume

p	pressure, in $N/m^2,\ Pa,\ dynes/cm^2$, or $torr$
q	heat flux vector
r	radial coordinate in cylindrical coordinate system
s	surface area of control volume
s	surface area; arc length of planar surface curve
t	time, in s or ms; tangential vector
u	flow velocity, in cm/s or m/s; x-component of flow velocity
v	control volume in space
v	volume; velocity or speed; flow velocity relative to bore front in the undular bore problems; the y-component of flow velocity
x	characteristic length; position vector
x, y	coordinates of point in Cartesian coordinate system
z	z-direction coordinate in Cartesian coordinate system; longitudinal coordinate in cylindrical coordinate system; water front position in the broken dam problem

Upper Case

$\mathbf{A}$	physical quantity in the conservation equation
$\mathbf{B}$	function describing flux of $\mathbf{A}$ in the conservation equation
B	frequency
C	Courant number; contraction coefficient in the sluice gate problem
C_p	specific heat at constant pressure
D	wheel diameter; liquid self-diffusivity
F	force; volume force; surface force; volume of fluid function; smooth continuous free surface; melt pool length or ‘foot’ length

G	Gibbs free energy; distance between nozzle and spinning wheel
H	dimensionless residual top of water column; melt pool height in melt spinning
I	unit dyad or unit tensor of rank two
I	nucleation frequency or rate, in N/m^5 or N/m^4
J	index of cell in y-direction
K	convolution kernel mask or stencil; kinetic parameter for nucleation
L	distance; characteristic length; latent heat, in $Joule/kg$; length of squared control cell
M	convolution mask size
N	unit normal to free surface at $(\vec{x}, t)$; convolution mask size; the Avogadro's number 6.022×10^{23}
R	radius of curvature; radius of nucleus
S	entropy; surface of arbitrary control volume in fluid; surface contact area of nuclei; ribbon stay distance on wheel surface
$\mathbf{S}$	rate of strain tensor
T	temperature; dimensionless time
U	continuous growth rate of solid/liquid interface; velocity; dimensionless velocity; characteristic velocity in x-direction; spinning speed of wheel
V	volume; flow velocity vector; characteristic velocity in y-direction; ejection velocity of molten jet; arbitrary control volume in fluid
Z	orifice diameter in melt spinning; dimensionless front position in the broken dam problem

Greek Symbol

α	thermal diffusivity; upstream differencing parameter; ratio of water heights on two sides of bore front; dimensionless crystal-melt interface energy parameter; relaxation factor or weight parameter
γ	aspect ratio of water column in the broken dam problem
δ	spatial or temporal increment in numerical algorithms; ribbon thickness
ϵ	emissivity of material
ε	cooling rate
η	nondimensional variable in the flat plate boundary layer theory; residual height of water column in the broken dam problem
θ	contact angle of two immiscible fluids with solid wall; the inclined angle of planar free surface; wetting angle
κ	surface curvature
μ	dynamic viscosity of fluid, in g/cms or kg/ms
ν	kinematic viscosity of fluid, in cm^2/s ($poise$) or m^2/s; atomic jump frequency
ρ	fluid density, in g/cm^3 or kg/m^3
σ	fluid surface tension coefficient, in $dynes/cm$ or N/m; the Stefan-Boltzmann constant $5.67 \times 10^{-8}\ Wm^{-2}K^{-4}$
τ	dimensionless time; viscous stress
ξ	position of bore front in the undular bore problems
$\dot{\xi}$	traveling speed of bore front in the undular bore problems
π	mathematical constant, the ratio of a circle's circumference to its diameter in Euclidean geometry 3.1415926
ϕ	angle of rotation between two radial axes in cylindrical coordinate system

φ	interpolation function, e.g., B-spline
Γ	interface between two fluids

Dimensionless Parameter

Ca	Capillary number
Ec	Eckert number
Fr	Froude number
Ga	Galileo number
Pe	Peclet number
Pr	Prandtl number
Re	Reynolds number
Web	Weber number

Acronym

ALE	Arbitrary Lagrangian-Eulerian
CCT	Continuous Cooling Transformation
CFD	Computational Fluid Dynamics
CFL	Courant-Friedrichs-Lewy (condition)
CSF	Continuum Surface Force
DA	Direct Accurate (algorithm for free surface normal estimation)
FFT	Fast Fourier Transform
GG	Green-Gauss (gradient method)
H-N	Hirt-Nichols (algorithm for free surface evolution)
ICCG	Incomplete Cholesky Conjugate Gradient

LDV	Laser Doppler Velocimetry
LHS	Left-Hand Side
LSM	Level Set Method
MAC	Marker and Cell
PIV	Particle Image Velocimetry
PLIC	Piecewise Linear Interface Construction
PPE	Pressure Poisson Equation
RHS	Right-Hand Side
TTT	Temperature Time Transformation
VOF	Volume of Fluid

Subscript

$_\infty$	denotes infinity away flow field
$_0$	denotes initial conditions; reference or constant value
$_{1/2}$	denotes interfaces of two neighboring grid cells for both orthogonal directions
$_1$, $_2$	denote two fluids separated by free surface or two sides of interface, respectively; incident and departing flows on two sides of bore front, respectively
$_2$	denotes the *venna contracta* downstream sluice gate
$_a$	denotes atomic, molar, or per mole; amorphous state
$_\mathrm{a}$	denotes an ambient vapor phase on one side of an interface
$_\mathrm{b}$	denotes body or buoyancy force
$_c$	denotes contraction; critical value; crystalline or crystallization
$_{cr}$	denotes critical value

d	denotes ribbon delivery velocity or ribbon casting rate
f	denotes fluid
g	denotes glass state
i,j	denote grid cell (i, j) along x- and y-directions, respectively; indices of tensor
j	denotes jet flow in melt spinning
k	denotes index of tensor or column matrix
loss	denotes heat loss on free surface
m	denotes equilibrium melt temperature; molecular
n, n	denotes normal direction to solid wall or free surface; nozzle; nucleation
r	denotes radial direction in cylindrical coordinate system
s	denotes point at interfacial surface; surface of integration for fluid volume
s	denotes surface; solidified fraction; per unit area
sa	denotes free surface force per unit area
sv	denotes surface volume force due to surface tension
t, t	denotes tangential direction along solid wall or free surface
t	denotes temporal component of normal vector $\vec{N}(\vec{x}, t)$; partial derivatives with respect to time t
v	denotes per unit volume or volumetric; volume
v	denotes fluid volume of integration
w, w, wall	denote various conditions on solid boundary; wheel
x	denotes spatial component of normal vector $\vec{N}(\vec{x}, t)$

x, y	denote partial derivatives with respect to x and y, respectively; two components of dependent variables along x- and y-directions, respectively
z	denotes axis of rotation in cylindrical coordinate system
B	denotes the Boltzmann constant
B, T, L, R	denote bottom, top, left, and right side of control volume, respectively
L	denotes liquidus or liquid phase of material
M	denotes moving or dynamic contact angle in wall adhesion
S	denotes solidus or solid phase of material
S	denotes free surface; static contact angle in wall adhesion
SB	denotes the Stefan-Boltzmann constant

Superscript

$*$	denotes normalized or dimensionless physical variable, e.g., time, coordinates, velocity, pressure, density, viscosity, surface tension coefficient, and etc.
$\prime$	denotes intermediate variable, physical properties or offset coordinate; variable of integration or convolution; derivative of function
2	denotes B-spline function of degree 2
(l)	denotes degree of B-spline function φ
n	denotes time level; normal component of vector
(L)	denotes liquidus or liquid phase of material
(S)	denotes solidus or solid phase of material
T	denotes transpose of vector or tensor matrix

δ	denotes Cartesian geometry when equals to 0; cylindrical geometry when equals to 1

Overbar

$\bar{\ }$	denotes average value
$\dot{\ }$	denotes rate of change
$\hat{\ }$	denotes unit vector in orthogonal coordinate system
$\tilde{\ }$	denotes intermediate value in solving equations; mollified function
$\vec{\ }$	denotes vector

Delimiter

$\vert\ \vert$	denotes absolute value or modulus
$\llbracket\ \rrbracket$	denotes difference of variable between two sides of free surface
$\langle\ \rangle$	denotes average of variable between two sides of free surface

Mathematical Symbol

$\cdot$	dot product
$:$	double inner product of tensor
∇	Hamilton or nabla operator
∂	partial derivative symbol
Δ	characteristic length; difference of physical properties or variables between solid and liquid states
$*$	convolution of two functions

ACKNOWLEDGMENT

Acknowledgment is gratefully made to the Department of Aerospace Engineering at Iowa State University for the financial support and research facilities it provided during my Ph.D. pursuit, and Ames National Lab of the U.S. Department of Energy for providing computer resources.

I express my sincere gratitude to my advisors, Dr. Ambar Mitra and Dr. Suleyman Biner. Their expertises, academic advice, guidances, passions, and patience helped me throughout this work. I am also extremely grateful to Dr. Hui Hu and Dr. Tom Shih from our Department, Dr. Matthew Kramer from the Department of Materials Science and Engineering and Ames Lab, and Dr. Ron Nelson from the Department of Mechanical Engineering, for serving as members of my POS committee. I am indebted to Dr. Matthew Kramer for interpretations of the experiment results and photograph reprint permissions. Many thanks also to the faculty and staff of our department.

My appreciation is also expressed to Dr. John Hochstein from the Department of Mechanical Engineering at the University of Memphis, and Dr. Douglas Kothe from Oak Ridge National Laboratory of the U.S. Department of Energy, for their enlightening technical discussions with me.

I would also like to extend my thanks to my best friends for their help.

Finally, this thesis is dedicated to my parents and brother, whose love, affection, and unconditional support always make my achievement.

ABSTRACT

The work provides methodologies for studying, designing, and optimizing melt spinning processes of fiber manufacture. Amorphous metallic materials can be created through melt spinning processes, in which a highly spinning wheel undercools a jet of molten metal or alloy below the equilibrium melting and the nucleation temperatures. Free-jet melt spinning employs a larger nozzle-wheel gap compared to planar flow casting. The instability of melt pool formation in a free-jet melt spinning will allow the variability of ribbon production. In general, a stable delivery of amorphous materials depends simultaneously on various control parameters, such as wheel speed, molten flow viscosity, surface tension force, and heat transfer. To analyze dynamical and thermodynamical characteristics of a free-jet melt spinning, two mathematical models, free surface and rapid solidification, have been established by means of Computational Fluid Dynamics. Based on the nucleation theory, I have predicted the nucleation temperature and the critical cooling rate for an alloy Fe_{75}-Si_{10}-B_{15} (at.%). The applications of these crystalline solidification properties in the simulation and analysis help the researchers gain insight into the processes. The research focuses on a novel simple and second-order accurate algorithm for computing surface normal and curvature in the Volume of Fluid method; it reconstructs the continuum surface force model to eliminate spurious currents. A computer program has been developed with the enhanced numerical schemes and the capability of heat transfer for two-dimensional laminar Newtonian surface flows. It conducted numerical simulations of impingement of a melt stream against a highly rotating wheel, and explains the complicated processes with numerical results of velocity and temperature in melt pools. The analytical estimates of ribbon thickness presented in the thesis agree with the experimental observation of the alloy. An in-depth investigation of the melt spinning process was performed to develop benchmarks of process variables for amorphous material production.

CHAPTER 1 INTRODUCTION

In this work, mathematical models are established for free surface and rapid solidification in accordance with the physical principles. Some numerical approaches are developed to simulate, study, and design free-jet melt spinning for amorphous production of an alloy Fe_{75}-Si_{10}-B_{15} (at.%).

1.1 Background

In a melt spinning process, as illustrated in Figure 1.1, a metallic melt jet undercools on a quench spinning wheel before crystallization is activated. As a result, a thin amorphous ribbon with disordered microstructures rapidly solidifies, exhibiting some mechanical, magnetic or chemical properties that the crystalline solid does not possess.

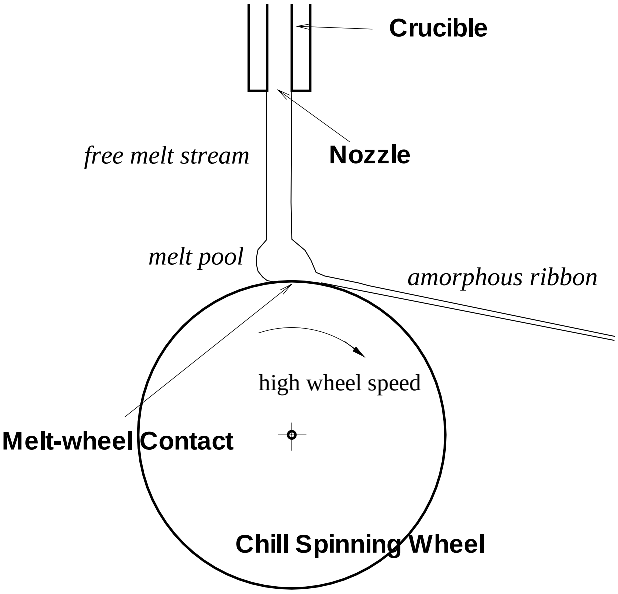

Figure 1.1 Schematic of free-jet melt spinning

Melt spinning, also known as spin casting, has long found utility in amorphous material manufacture. The commencement of metallic glasses (materials in an amorphous state) by quenching of the liquid alloys dates to the 1960's, when it originated in United States universities[1]. Thin slabs of steel ($\sim 200\ mm$) have been manufactured since 1989 and thin aluminum and steel ribbons ($\sim 1\ mm$) were produced in the late 1990's[2].

To produce desired atomic-scale structures, rapid solidification with a cooling rate greater than $10^2\ K/s$[3] is often applied in practice by imposing (1) a high undercooling prior to solidification, (2) a high velocity of advance during continuous solidification, and/or (3) a high cooling rate during solidification[4]. Rapid solidification processing can be realized utilizing spray methods, chill methods, weld methods, or consolidation and fabrication methods[4]. Accordingly, melt spinning is a chill method and falls into the category of imposing a high cooling rate during solidification.

There are two varieties of melt spinning, planar flow casting and free-jet; application of which differs in the gap between nozzle and wheel surface. Free-jet (or called chill block) melt spinning has a larger gap than planar flow casting (not shown in the figure). In a properly operated free-jet melt spinning process (see Figure 1.1), the melt jet strikes the moving wheel surface with a certain velocity after traveling some distance. It reduces stability in the formation of melt pool, and results in a weak control of shape and quality of amorphous production[5, 6].

Both planar flow casting and free-jet melt spinning proceed high momentum and thermal transport, free surface with strong surface tension force, and phase transformation from liquid to solid. Other process parameters include:

- the ejection melt flow rate;
- the pressure stability and temperature of molten alloy in crucible;
- wheel asperities;
- chamber gas pressure and composition;
- pressure differential between the crucible and the wheel;
- melt purity.

As illustrated in Figure 1.1, the interface between the molten flow and chamber gas, if the chamber is not vacuum, is a free surface evolving essentially under momentum and surface tension force of the flow. In the normal direction of a free surface, it undergoes sharp transitions in density, viscosity, and pressure; whereas in the tangential direction, those physical properties and flow variables remain unchanged or continuous, and the configuration of free surface changes smoothly. Unlike pressure, surface velocity varies continuously across the interface. It is difficult to impose the boundary conditions on a varying free surface in a numerical simulation.

1.2 Literature Reviews and Unresolved Issues

Respectively, Kothe et al[7], Scardovelli et al[8], and Floryan et al[9] summarize the history of numerical methods for solving interfacial flow under surface tension force. Among those Computational Fluid Dynamics (CFD) models are Hirt and Nichols' Volume of Fluid (VOF) method (with the H-N algorithm)[10], Osher and Sethian's Level Set Method (LSM)[11–13], and Brackbill's Continuum Surface Force (CSF) model[14]. Kothe et al[15, 16] have developed the computer program RIPPLE for two-dimensional (2D) incompressible laminar Newtonian surface flows with using VOF method, the H-N algorithm, the CSF model, and finite difference and volume methods. Lafaurie et al[17] introduced surfacee tension stress tensor, also called capillary pressure tensor, in the Continuous Surface Stress (CSS) model. Finite element method is also employed for free boundary problems like in the Stefan problem[18]. The LSM, established in the 1980's, tracks the motion of a free surface by embedding the interface as the zero level set of a signed distance function, level set function, in an Eulerian frame. These numerical models are currently implemented in engineering research and design.

Kothe[19] points out that accurate estimation of surface normal and curvature for further computation of surface tension force still remains an unresolved issue. For the local surface normal and curvature, Brackbill et al[14] offer two schemes, Marker and Cell (MAC)[20] and arbitrary Lagrangian-Eulerian (ALE)[21, 22], which belong to the Green-Gauss (GG)[7] gradient method. Various methods of surface normal estimation have been reported in [7, 23, 24] for free surface simulation using the VOF method or the LSM[11, 12]. Some require more computing time and give unsatisfactory results.

Spurious or parasitic currents that exist in the neighborhood of interface were first observed in the Lattice-Boltzmann method[25], and then in other surface tension models including the CSF model and Lafaurie's conservative method[17]. Those undesirable currents are created by some defects inherently hidden in the CSF model. Attempts have been made[23, 24, 26, 27] to reduce or eliminate such man-made parasitic currents. The researchers have employed various methods, such as reconstructing free surface, re-evaluating curvature, developing new approaches for surface pressure, and remodeling surface tension force; however, none successfully eliminated the spurious currents induced in the simulation of a circular free surface in equilibrium with zero initial velocity.

Melt spinning not only casts thin ribbons or slabs, but also elicits considerable attention from researchers. However, most of them focused on planar flow casting. Berger and Ai[28] have developed a mathematical model for planar flow casting melt spinning based on a 2D steady-state condition and the conservation laws. Steen and Karcher[2, 29, 30] present a kinetic analysis of spin casting of metals. Gutierrez et al[6] found a recirculating flow inside the melt puddle that relates to the regularly-spaced powder of visualization near the top of the ribbons observed by Zielinski et al[31]. The ribbon thickness has been documented to vary inversely with wheel speed by a power index from 0.5 to 1[2, 5, 32, 33]. The researchers[2, 5, 34, 35] inclined to use the boundary layer theory in the estimation of ribbon thickness. Strictly speaking, viscous force plays such an important role that the melt pool cannot be treated as a potential flow. The viscosity in the ribbon as well as in the melt pool grows exponentially when it rapidly solidifies on the quench wheel surface.

Other researchers[35–38] have investigated heat transfer and solidification of melt spinning. By best fitting the measured temperature, Takeshita et al[37] found the heat transfer coefficients range between 10^5 and 10^6 W/m^2K and vary with the the contact area of molten jet with wheel surface; they also found another heat transfer coefficient is independent of the wetting condition. In their 2D numerical simulations, Bussmann stipulated the heat transfer coefficient of the melt-wheel boundary as 10^6 W/m^2K[39]. Clyne[40] considered the latent heat as a heat source in the energy equation growing at a crystal front rate. Pryds et al[41] implemented the idea into a one-dimensional (1D) heat source form. Clyne and Pryds chose a sphere with 10 *micro* radius as the control volume in the nucleation temperature calculation. According to [42], this droplet sample originated in the forced convective cooling environment of the Pratt and Whitney centrifugal atomization process[43]. However, the spherical diameter used is not applicable for any other materials because the atomic diameters differ greatly.

Two or three-dimensional (3D) numerical modeling and simulations for planar casting flow have been reported in [35, 44–47]. Bussmann et al[39] conducted a 2D numerical study of steady flow within a molten puddle in planar flow casting using RIPPLE. Exponential increases in a molten metallic flow with temperature drops require that the time step in numerical simulations be less than an unacceptable degree. The stability restrictions to an explicit scheme often create numerical difficulties because the wheel speed is extremely high compared with the jet ejection velocity at the nozzle. The momentum by the highly spinning wheel surface to the molten stream was omitted in the previous numerical simulations of melt spinning.

Using high digital camera, Kramer et al[5] revealed amorphous alloy formation and found a characteristic critical length scale for the ribbon thickness. Both Kramer and Davies[48] present a critical cooling rate of $10^5 \sim 10^6$ K/s for Fe-Si-B. Kramer observed that the alloy is glowing red-hot after separation from the quench wheel for lower wheel speeds that are above 7.5 m/s. Some crystals grow from the ribbon bottom and quenched in the half way to the top surface[37] and the crystallization occurs on the air-side of ribbon when the wheel speed is lower than a certain value[5]. Napolitano et al[49] found upper and lower limits for melt spinning rates for glass formation after examining melt pool behavior in free-jet melt spinning. Wang et al[50] provide experimental determination of the interfacial heat transfer between molten metal droplets and metallic substrate.

In practice, many experimental techniques such as Laser Doppler Velocimetry (LDV) and Particle Image Velocimetry (PIV) are unable to measure and visualize the molten metallic flow velocity. High-speed digital imaging technique has some restrictions in recording temperature within the molten stream, because the temperature changes up to hundreds of degrees in *milliseconds* while the ribbon is spun out as thin as 10^{-2} mm.

Some issues discussed in the reviews will be my research emphases which follow:

- inaccurate algorithms for surface normal and curvature;
- spurious currents created by the CSF model;
- the thermodynamical properties of the alloy for numerical simulation;
- the momentum transferred by the highly spinning wheel;
- strong viscous force due to the exponential temperature-dependent viscosity;
- the capability of heat transfer.

To comprehensively analyze a typical melt spinning process for an alloy using CFD methods, one should establish a mathematical model for melt spinning to deal with complicated surface flows, surface tension force, heat transfer, and phase changes.

1.3 Current Research

Through numerical and theoretical methods, some vigorous analysis of free-jet melt spinning in dynamics and thermodynamics with the support of experimental measurements is intended in the research to reveal the underlying principles of the melt spinning process, and to help identify the key control parameters for the amorphous metallic production.

A computer program has been developed using the improved numerical approach and it has been verified by some famous examples in various senses. The simulations of free-jet melt spinning have provided us visualization of velocity, pressure, and temperature in the flow field.

A new second-order accurate algorithm for normal and curvature has been developed from Taylor's series expansion. Based on the mathematical equations and physical principles, surface tension is reconstructed within an interfacial layer to reproduce the pressure jump as in Laplace's formula and eliminate spurious currents. I propose a novel idea of immersed length in the estimations of density and surface tension force at the control cell center. Incorporation of the thermal-energy equation into the system of governing equations will exercise for further thermal analysis. I will present a new convolution function for mollifying color function. The temperature-dependent viscosity of molten alloy flow is applied in the simulation.

In summary, my research is mainly composed of ten parts as follows:

1. a second-order accurate algorithm for computing surface normal and curvature;
2. an introduction of immersed length and classification of cells;
3. modifications in the CSF model and the pressure approach;
4. enhancement the dynamical simulation with the thermal-energy equation;
5. scaling-up of the system of governing equations;
6. incorporation of the translation terms in the governing equations;
7. prediction of nucleation temperature and critical cooling rate for the alloy;
8. computations of ribbon thickness, cooling rate, and heat transfer coefficient on the wheel surface;
9. simulation and analysis of the melt spinning process;

10. investigation of the melt spinning process mechanism and the control parameters.

In addition, in the prediction of nucleation and critical cooling rate, the magnitude of a characteristic length for control volume or area is chosen more generally so that it is applicable to other metals or alloys in the determination of nuclei appearance per unit volume per unit time.

1.4 Thesis Structure

The work begins with the conservation law across an interface of discontinuity. In Chapter 2, the kinematic, dynamic, and thermal jump conditions across a free surface are derived by virtue of the conservation law. Section 2.1 relates free surface evolutions with the jump conditions. Section 2.2 lists the simplified boundary conditions on free surfaces under various assumptions.

Chapter 3 contains the system of 2D governing equations, the VOF method, the H-N algorithm, and the CSF model (Sections 3.1 through 3.4). Grid generation and numerical stabilities are consecutively reviewed in Section 3.5 and Section 3.6 followed by Section 3.7 for the formulation of wall adhesion.

The modeling of a free surface flow with energy, heat transfer, solidification, and phase changes is discussed in Chapter 4. Along with the formulation of surface temperature gradients in Section 4.2, the incorporation of the energy equation as given in Section 4.1 enables us to compute temperature distribution in surface flows. The rapid solidification and nucleation theory in Section 4.3 details the determination of nucleation temperature and critical cooling rate.

Chapter 5 presents my contribution to the numerical algorithms for two-phase flows. A new method for calculating mollified color function from the image processing theory is enunciated in Section 5.1. I will derive a simple Direct Accurate (DA) algorithm to compute surface normal and curvature in Section 5.2. Section 5.3 introduces the concept of immersed length, the classifications of grid and control cells, and the reconstructed CSF model. Section 5.4 explores the modified pressure approach. The translation terms are added into the equations as referred to Section 5.5 and the system of equations is scaled up as discussed in Section 5.6, both of which enhance the computer program to simulate a melt pool formation on a highly moving wheel surface.

In Chapter 6, the improved numerical models are interrogated by two example calculations − broken dam in Section 6.1 and undular bore in Section 6.2. An example calculation of sluice gate flow in Section 6.3 validates the normalization of the system of equation. The DA algorithm provides accurate normals and curvatures for an inclined planar and a circular free surface as shown in Section 6.4. The strategy proposed in Section 6.5 eliminates the spurious currents found in an inclined plane and a circular droplet; both surfaces are in equilibrium and with zero initial velocity.

Chapter 7 is dedicated to the dynamical and thermal analysis of melt spinning; it reveals the mechanisms of melt spinning and amorphous alloy formation. In Section 7.1, physical and thermodynamical properties of an alloy Fe_{75}-Si_{10}-B_{15} (at.%) are prepared. In Section 7.2, I estimate the nucleation temperature and critical cooling rate in two ways for the alloy. After a free-jet melt spinning process is introduced in Section 7.3, some consideration of 2D simulation is made in Section 7.4 for the 3D free-jet melt spinning process. The simulation of a jet impingement on a rotating wheel in Section 7.5 also confirms the modifications of the governing equations and offers dynamical and thermal details of pool formation. Ribbon thickness of melt spinning is predicted in Section 7.6; whereas Sections 7.7 through 7.10 apply a 1D heat conduction problem to the investigation of the correlations of process parameters with amorphous alloy formation.

Chapters 8 and 9 include some conclusion and recommendations, respectively.

Appendixes A through C offer some numerical algorithms for reference.

CHAPTER 2 MATHEMATICS OF INTERFACIAL FLOWS

The conservation laws and the jump condition across a surface of discontinuity are demonstrated in Section 2.1. From the jump condition, we can find some kinematic, dynamic, and thermal boundary conditions on an interface in association with evolutions of the free surface[8]. Section 2.2 discusses the simplified boundary conditions under various assumptions or given conditions.

2.1 Conservation Laws and Jump Conditions

A free surface Γ as shown in Figure 2.1 is defined as a smooth interface between two immiscible fluids with no mass across it. Using a function F (refer to Section 3.2 of Chapter 3), it can be represented as

$$F(\vec{x}, t) = 0, \tag{2.1}$$

where $\vec{x}$ is the position vector of flow field and t is time. In the tangential direction of a free surface, the fluxes of mass, momentum, and energy are continuous[11].

In fluid mechanics, the conservation law for a physical quantity $\mathbf{A}$ is described in an integral form

$$\frac{\partial}{\partial t}\int_{\mathrm{v}} \mathbf{A} dv + \int_{\mathrm{s}} \mathbf{B} \cdot \hat{n} ds = \int_{\mathrm{v}} f dv, \tag{2.2}$$

in an arbitrary but fixed control volume v with control surface s and surface unit normal $\hat{n}$, or in a differential form

$$\frac{\partial \mathbf{A}}{\partial t} + \nabla \cdot \mathbf{B} = f, \tag{2.3}$$

where function $\mathbf{B}$ contains the flux of $\mathbf{A}$ across the surface s and other associated surface physical quantities, and f is the source or sink rate of $\mathbf{A}$. In the equations, $\mathbf{A}$ is a scalar, and $\mathbf{B}$ is a vector as in the mass or energy equation; $\mathbf{A}$ is a vector, and $\mathbf{B}$ is a tensor of rank two or a dyadic as in the momentum equation with no dot product '$\cdot$'. In general, the RHS term of the equations f vanishes in the mass equation, unless there is a mass source/sink in the flow field. f stands for body force in the momentum equation, whereas it contains heat source/sink terms in the energy equation (refer to Table 2.1, Section 3.1 of Chapter 3, and Section 4.1 of Chapter 4).

	$\mathbf{A}$	$\mathbf{B}$	f
Mass	ρ	$\rho\vec{V}$	
Momentum	$\rho\vec{V}$	$\rho\vec{V}\vec{V} + p\mathbf{I} - \tau$	$\rho\vec{g} + \vec{F}_\mathrm{b}$
Energy	e	$\vec{V}e + \vec{q}$	$-p\nabla \cdot \vec{V} + \tau : \nabla\vec{V}$

Table 2.1 Variables in the conservation laws

According to the Reynolds transport theorem, the jump conditions[11, 51–53] for conservation laws across a smooth surface Γ is derived in terms of unit normal $\hat{n}$ to the free surface and normal velocity v_n of the interface (see Figure 2.1)

$$[\![\mathbf{A}]\!]_1^2 v_n = [\![\mathbf{B} \cdot \hat{n}]\!]_1^2, \tag{2.4}$$

where $[\![\ ]\!]_1^2$ denotes the difference of quantity $\mathbf{A}$ or $\mathbf{B}$ between side '2' and side '1' across the interface Γ; for example, $[\![\mathbf{A}]\!]_1^2 \equiv \mathbf{A}_2 - \mathbf{A}_1$.

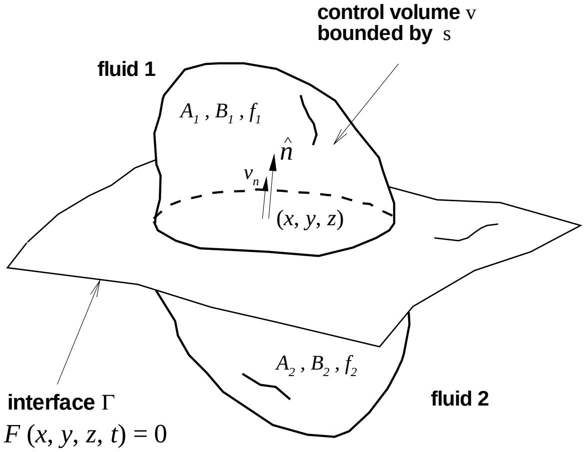

Figure 2.1 Illustration of a control volume separated by an interface Γ

If no fluid particle crosses through the continuous free surface Γ, the normal velocity of free surface evolution is equal to the flow velocity

$$v_n = \vec{V} \cdot \hat{n}, \tag{2.5}$$

namely, the application of Eq. (2.4) to the mass conservation. Eq. (2.5) becomes

$$v_n = -\left.\frac{\partial F}{\partial t}\right/ |\vec{n}| \,, \tag{2.6}$$

where $\vec{n}$ is the normal vector to free surface Γ (refer to Eqs. (2.1), (3.22), (3.11), and (3.12)). Eq. (2.4) is thus written relating with F:

$$[\![\mathbf{A}]\!]_1^2 \frac{\partial F}{\partial t} + [\![\mathbf{B}]\!]_1^2 \cdot \vec{n} = 0, \tag{2.7}$$

or

$$[\![\mathbf{A}]\!]_1^2 N_t + [\![\mathbf{B}]\!]_1^2 \cdot \vec{N}_x = 0, \tag{2.8}$$

where N_t and $\vec{N}_x$ are temporal and spatial components of the unit normal vector $\vec{N}$ in $(\vec{x}, t)$, respectively, as follows:

$$N_t = \frac{\dfrac{\partial F}{\partial t}}{\sqrt{\left(\dfrac{\partial F}{\partial t}\right)^2 + |\vec{n}|^2}} \qquad \text{and} \qquad \vec{N}_x = \frac{\vec{n}}{\sqrt{\left(\dfrac{\partial F}{\partial t}\right)^2 + |\vec{n}|^2}}. \tag{2.9}$$

Notice that the subscripts t and x in Eq. (2.9) denote the temporal and spatial components of $\vec{N}$, respectively, other than partial derivatives. Eq. (2.8) is also referred to as *Rankine-Hugoniot jump conditions* in [54]. The RHS's of Eqs. (2.7) and (2.8) are non-zero if there is a source or sink of f along the interface Γ.

2.2 Boundary Conditions on Free Surface

2.2.1 Kinematic Boundary Condition

From the conservation of mass, the kinematic boundary condition on free surface is derived as

$$\frac{\partial F}{\partial t} + \left(\vec{V} \cdot \nabla\right) F = 0, \tag{2.10}$$

if we are given in Eq. (2.7):

$$\mathbf{A} = \rho, \qquad \mathbf{B} = \rho \vec{V}, \tag{2.11}$$

where ρ is fluid density and $\vec{V}$ is the flow velocity vector. Eq. (2.10) describes the evolution of free surface. It is identical to Eq. (3.22), which has been used to compute the normal velocity v_n as in Eqs. (2.5) and (2.6).

For momentum conservation, we have that

$$\mathbf{A} = \rho \vec{V}, \qquad \mathbf{B} = \rho \vec{V}\vec{V} + p\mathbf{I} - \tau, \qquad f = \rho \vec{g} + \vec{F}_{\mathrm{b}}, \tag{2.12}$$

where p is flow pressure, τ viscous tensor, $\vec{g}$ gravitational acceleration, $\vec{F}_\mathrm{b}$ body force, and $\mathbf{I}$ unit dyad (see Eq. (3.2)). Then Eq. (2.7) becomes

$$\frac{\partial F}{\partial t} + \left(\vec{V} \cdot \nabla\right) F = \frac{|\vec{n}|}{v_n(\rho_2 - \rho_1)} \left\{-(p_2 - p_1) + \hat{n} \cdot [(\tau_2 - \tau_1)\hat{n}] + \sigma\kappa\right\}, \tag{2.13}$$

if it is projected along the normal direction $\hat{n}$, and

$$\frac{\partial F}{\partial t} + \left(\vec{V} \cdot \nabla\right) F = \frac{|\vec{n}|}{v_t(\rho_2 - \rho_1)} \left\{\hat{t} \cdot [(\tau_2 - \tau_1)\hat{n}] + \left(\frac{\partial \sigma}{\partial s}\right)\right\}, \tag{2.14}$$

if it is projected along the tangential direction $\hat{t}$, where σ is the surface tension coefficient, κ surface curvature, s surface curve length, and v_t the tangential velocity of free surface.

Surface tension force arises when the interface between two immiscible fluids has a curved configuration as in Eq. (2.13), or the surface tension coefficient varies along the interface as in Eq. (2.14). Throughout this work, the term **'fluid 2'**, for brevity, is specifically referred to as a fluid, usually a liquid, having greater density and stronger surface tension coefficient, while **'fluid 1'** represents the other fluid, which can be a liquid or a gas (see Figure 2.1).

Notice viscous friction force between two fluids is ignored in Eq. (2.14) so that the tangential velocity is given by

$$v_t = \vec{V} \cdot \hat{t}. \tag{2.15}$$

Eqs. (2.5) and (2.15) present that free surface evolves with flows.

For energy conservation, the variables in Eq. (2.4) are given from Eq. (4.1):

$$\mathbf{A} = e, \qquad \mathbf{B} = \vec{V}e + \vec{q}, \qquad f = -p\nabla \cdot \vec{V} + \tau : \nabla\vec{V}, \tag{2.16}$$

where e is enthalpy, thermal energy per unit mass (also referred to as *sensible heat*). $\vec{q}$ in Eq. (2.16) is heat flux vector,

$$\vec{q} = -k\nabla T, \tag{2.17}$$

where T is temperature, and k is the heat conductivity coefficient. Eq. (2.7) is then rewritten as

$$\frac{\partial F}{\partial t} + \left(\vec{V} \cdot \nabla\right) F = -\frac{(\vec{q}_2 - \vec{q}_1) \cdot \vec{n}}{e_2 - e_1}. \tag{2.18}$$

Notice the LHS's of Eqs. (2.13), (2.14), and (2.18) are all in the form of the kinematic boundary equation.

The kinematic boundary condition is expressed in the form of height function as seen later in Eq. (3.21). It also appears in the transport equation of LSM.

2.2.2 Dynamic Boundary Condition

Comparing Eqs. (2.13) and (2.14) with Eq. (2.10), we have the dynamic boundary condition of free surface,

$$-(p_2 - p_1) + \hat{n} \cdot [(\tau_2 - \tau_1)\hat{n}] + \sigma\kappa = 0 \tag{2.19}$$

which is the pressure jump, namely Laplace's formula in the normal direction, and

$$\hat{t} \cdot [(\tau_2 - \tau_1)\hat{n}] + \left(\frac{\partial \sigma}{\partial s}\right) = 0, \tag{2.20}$$

in the tangential direction to free surface. Eq. (2.19) can be rewritten as follows:

$$p_2 = p_1 + \sigma\kappa + \hat{n} \cdot [(\tau_2 - \tau_1)\hat{n}]. \tag{2.21}$$

The pressure jump as in Eq. (2.21) simply comes from concavity-dependent surface tension and viscous force on free surface.

As shown in Figure 2.2, if the viscous effect is assumed to be negligible compared with the surface tension force, namely if the *capillary number* **Ca**, as defined later in Eq. (3.39), is very small, Eq. (2.21) reduces to Laplace's formula,

$$p_2 = p_1 + \sigma\kappa, \tag{2.22}$$

where p_1 is the ambient pressure and $p_\mathrm{s} = \sigma\kappa$ is called the surface tension-induced pressure jump across the interface.

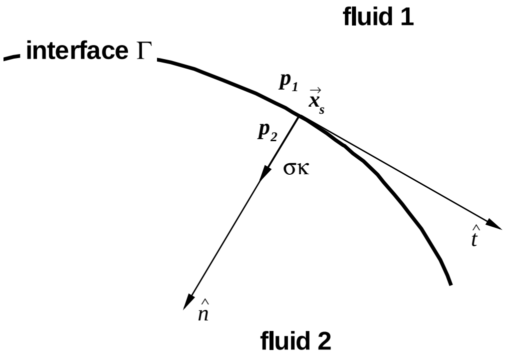

Figure 2.2 Illustration of Laplace's formula on a free surface Γ

If the surface tension coefficients vary along free surface, e.g., in thermocapillary phenomena, the dynamic boundary condition in the tangential direction of free surface, namely Eq. (2.20) in the gradient form, is taken into account,

$$\hat{t} \cdot [(\tau_2 - \tau_1)\hat{n} + \nabla\sigma] = 0. \tag{2.23}$$

Furthermore, if the surface tension coefficients are constant along free surface, Eq. (2.23) reduces to

$$\hat{t} \cdot [(\tau_2 - \tau_1)\hat{n}] = 0 \tag{2.24}$$

at any point on free surface, which means the viscous force in the tangential direction of free surface is always in equilibrium between the two fluids no matter how small the viscosity one fluid has. Finally, we may have

$$\tau_2 = \tau_1, \tag{2.25}$$

if we invoke Eq. (2.24) and assume the viscous force is negligible in the normal direction across free surface, namely $\hat{n} \cdot [(\tau_2 - \tau_1)\hat{n}] = 0$. Eq. (2.25) demonstrates the viscous stress tensors are continuous across free surface under the assumptions of high surface tension and the constant surface tension coefficient in a surface flow.

2.2.3 Thermal Boundary Condition

From Eqs. (2.10) and (2.18), we conclude that

$$(\vec{q}_2 - \vec{q}_1) \cdot \hat{n} = 0. \tag{2.26}$$

Eq. (2.26) shows the vector of heat flux jump on a free surface always directs along the free surface with no heat flux across the free surface, as illustrated in Figure 2.3.

If radiation and heat convection are considered to be the major methods of heat loss or gain for **fluid 2** on free surface Γ, according to *Newton's law of cooling* and the *Stefan-Boltzmann law*, Eq. (2.26) becomes

$$-k_2\nabla T_2 \cdot \hat{n} = -k_1\nabla T_1 \cdot \hat{n} = -q_{\text{loss}} = -h(T_2 - T_1) - \epsilon\sigma_{\text{SB}}(T_2^4 - T_1^4), \tag{2.27}$$

where h is the heat transfer coefficient (kW/m^2K), emissivity of **fluid 2** $\epsilon \leqslant 1$, and the *Stefan-Boltzmann constant* $\sigma_{\text{SB}} = 5.67 \times 10^{-8}\ W/m^2K^4$.

In addition, a given heat flux can also be imposed on free surface for q_{loss} such that Eq. (2.27) becomes

$$-k\nabla T_2 \cdot \hat{n} = q_{\text{s}}(\vec{x}, t), \quad \text{or} \quad -k\nabla T_2 = \vec{q}_{\text{s}}(\vec{x}, t), \tag{2.28}$$

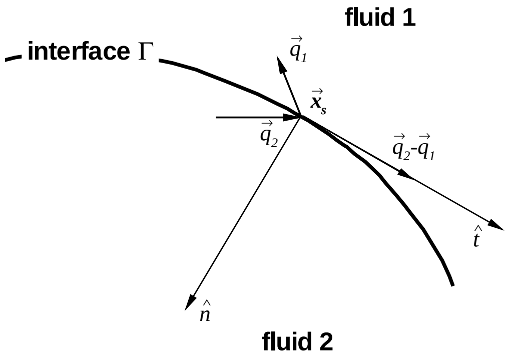

Figure 2.3 Illustration of heat flux directions on a free surface Γ

where $\vec{q}_{\mathrm{s}}(\vec{x},t) = q_{\mathrm{s}}(\vec{x},t)\hat{n}$ is the heat flux vector imposed on free surface. In particular, if **fluid 2** is a thermal insulation system, Eq. (2.28) reduces to

$$-k\nabla T_2 \cdot \hat{n} = 0, \tag{2.29}$$

which is an adiabatic boundary condition on free surface. Eq. (2.29) shows that the temperature gradient or the heat flux direction of **fluid 2** on a free surface is tangential to it.

A given constant temperature may be specified on free surface:

$$T_2 = T_{\mathrm{s}}, \tag{2.30}$$

which is an isothermal boundary condition on free surface with $q_{\mathrm{loss}} = 0$.

The subscript 2 of thermal conductivity k is ignored for **fluid 2** in Eqs. (2.28) and (2.29). Henceforth in the work, any properties or variables without subscripts in the governing equations are those referred to as **fluid 2**, unless otherwise stated.

CHAPTER 3 FREE SURFACE MODEL AND NUMERICAL ALGORITHMS

The numerical methodology are reviewed in the chapter. The readers may skip this context if familiar with the numerical models.

3.1 System of Governing Equations

The numerical model for a 2D incompressible free surface flow is established in an Eulerian frame based on a system of continuity and momentum equations, namely

$$\nabla \cdot \vec{V} = 0, \tag{3.1}$$

and

$$\frac{\partial \vec{V}}{\partial t} + \nabla \cdot \left(\vec{V}\vec{V} \right) = -\frac{1}{\rho}\nabla p + \frac{1}{\rho}\nabla \cdot \tau + \vec{g} + \frac{1}{\rho}\vec{F}_{\mathrm{b}}. \tag{3.2}$$

The velocity field $\vec{V}$ in the equations is a vector variable having two components of u and v in two orthogonal directions of space, respectively, varying with time,

$$\vec{V}\left(\vec{x}, t\right) = r^{\delta} u\left(x, y, t\right)\hat{\imath} + v\left(x, y, t\right)\hat{\jmath}, \tag{3.3}$$

where $\hat{\imath}$ and $\hat{\jmath}$ are two unit vectors of the orthogonal directions, and the fixed points $\vec{x}$ are expressed in either Cartesian,

$$\vec{x} = x\hat{\imath} + y\hat{\jmath}, \tag{3.4}$$

or cylindrical coordinates,

$$\vec{x} = r\hat{\imath} + z\hat{\jmath}. \tag{3.5}$$

The operator ∇ in Eqs. (3.1) and (3.2), and throughout this work is expressed as

$$\nabla = \frac{1}{r^{\delta}}\frac{\partial}{\partial x}\hat{\imath} + \frac{\partial}{\partial y}\hat{\jmath}, \tag{3.6}$$

where superscript δ on the radius r (also in Eq. (3.3)) is a constant equal to 1 in cylindrical or 0 in Cartesian geometry.

The viscous stress tensor τ in the momentum equation Eq. (3.2) is written for Newtonian flow as follows:

$$\tau = 2\mu\mathbf{S}, \qquad \mathbf{S} = \frac{1}{2}\left[\left(\nabla\vec{V}\right) + \left(\nabla\vec{V}\right)^{\mathrm{T}}\right], \tag{3.7}$$

where $\mathbf{S}$ is the rate-of-strain tensor, and μ is the fluid dynamic viscosity.

The surface tension coefficient σ is presumed to remain constant in the CSF model. In addition to other body forces, a volume force $\vec{F}_{\mathrm{sv}}$ is modeled for surface tension effect in Eq. (3.2) (see Eq. (3.26))[16],

$$\vec{F}_{\mathrm{b}} = \vec{F}_{\mathrm{sv}} \qquad \text{and} \qquad \vec{F}_{\mathrm{sv}} = \sigma\kappa\left(\vec{x}\right)\nabla F g(\vec{x}), \tag{3.8}$$

where F is VOF function, and $g(\vec{x})$ is a weight function:

$$g(\vec{x}) = 1 \qquad \text{or} \qquad F/\left\langle F\right\rangle, \tag{3.9}$$

with $\langle F\rangle = 1/2$ being the average of the colors for two liquids $(c_1 + c_2)/2$ (as defined in Eq. (3.23)). κ in Eq. (3.8) is the local free surface curvature computed from

$$\kappa = -\nabla\cdot\hat{n} = \frac{1}{|\vec{n}|}\left[\left(\frac{\vec{n}}{|\vec{n}|}\cdot\nabla\right)|\vec{n}| - \left(\nabla\cdot\vec{n}\right)\right], \tag{3.10}$$

where the unit normal $\hat{n}$ is obtained from the normal vector $\vec{n}$ to free surface:

$$\hat{n} = \frac{\vec{n}}{|\vec{n}|}, \tag{3.11}$$

and

$$\vec{n} = \nabla F. \tag{3.12}$$

The normal defined in Eq. (3.12) customarily points from **fluid 1** to **fluid 2**, as does the unit normal $\hat{n}$. Therefore, a negative sign in Eq. (3.10) guarantees a positive curvature for a convex free surface with respect to **fluid 2** (as shown in Figure 2.2). Notice we assume **fluid 2** has greater density.

Surface curvature is defined as the inverse radius of curvature from the mathematic point of view,

$$\kappa(\vec{x}_{\mathrm{s}}) = \frac{1}{R(\vec{x}_{\mathrm{s}})}, \tag{3.13}$$

where the subscript s denotes free surface. In 3D problems, the curvature in Eq. (3.13) becomes

$$\kappa(\vec{x}_{\mathrm{s}}) = \frac{1}{R_1(\vec{x}_{\mathrm{s}})} + \frac{1}{R_2(\vec{x}_{\mathrm{s}})}, \tag{3.14}$$

where $R_1(\vec{x}_\mathrm{s})$ and $R_2(\vec{x}_\mathrm{s})$ are two principal radii of curvature at point $\vec{x}_\mathrm{s}$.

As discussed in Eqs. (2.19) and (2.20), the dynamic condition on a free surface is found in the tensor form as follows[55, 56]:

$$(p_1 - p_2 + \sigma\kappa)\,\hat{n}_i = (\tau_{1,ik} - \tau_{2,ik})\,\hat{n}_k + \frac{\partial \sigma}{\partial x_i}, \tag{3.15}$$

where $\hat{n}_i$ represents unit normal $\hat{n}$ toward **fluid 2** in Figure 2.2.

Boundary and initial conditions are specified prior to solving the governing equations to give an enclosure to a hydrodynamics or aerodynamics problem. For any rigid walls emerging in flow field, viscous velocity boundary conditions are either no-slip,

$$\vec{V} = 0 \tag{3.16}$$

or free-slip (no penetration),

$$\hat{n}_\mathrm{wall} \cdot \vec{V} = 0 \tag{3.17}$$

where $\hat{n}_\mathrm{wall}$ is the wall unit normal.

The initial conditions of velocity $\vec{V}(\vec{x}, 0)$, pressure $p(\vec{x}, 0)$, and function $F(\vec{x}, 0)$ at time $t = 0$ are stipulated to the input for the computer program:

$$\begin{aligned} \vec{V}(\vec{x}, 0) &= \vec{V}_0 \\ p(\vec{x}, 0) &= p_0 \\ F(\vec{x}, 0) &= F_0. \end{aligned} \tag{3.18}$$

At $t = 0$, the initial configuration of a free surface is given by specifying a number of conic functions. The computer program initializes the free surface in a minimal energy configuration and smooth the VOF function so that F_0 in Eq. (3.18) is computed and the surface curvature is estimated for each cell of the flow domain.

3.2 Volume of Fluid (VOF) Method

Free surface can be treated as a special case of a *tangential discontinuity*[55] with continuous surface velocity in the normal and tangential directions, but discontinuous densities in the normal direction. A numerical model for free surface used in the computer program is so-called ‘Volume-of-Fluid’ (VOF) method, performing as a scheme to locate the surface, an algorithm to track the surface as a sharp interface moving through a computational grid, and an approach to apply boundary conditions at the surface.

In the VOF method, continuous free surfaces are tracked by means of a scalar variable $F(\vec{x}, t)$, where a unity value of F corresponds to a finite small area or volume occupied by **fluid 2**; otherwise, a zero value indicates a void area/volume. Thus, a fractional value of F between zero and unity within a discrete mesh cell represents a segment of the interfacial region of two fluids:

$$F\left(\vec{x},t\right)=\begin{cases} 1, & \text{in the fluid;} \\ >0,<1, & \text{at the free surface;} \\ 0, & \text{in the void.} \end{cases} \tag{3.19}$$

F is a scalar step function behaving like a Heaviside characteristic function in the normal direction[11]. For an incompressible flow, $F(\vec{x},t)$ might be defined in the normalization of density,

$$F(\vec{x},t)=\frac{\rho(\vec{x},t)}{\rho_f}, \tag{3.20}$$

where ρ_f is the constant fluid density of **fluid 2**, and ρ is the density contained in a grid cell if **fluid 1** is assumed to have zero density. F delineates the existence of fluids in such a way that the $F=1/2$ contour is regarded as the free surface of flow.

In contrast to the VOF method, the height function method employs a height function in the kinematic boundary condition,

$$\frac{\partial h}{\partial t}+u\frac{\partial h}{\partial x}-v=0, \tag{3.21}$$

where $y=h(x,t)$ is the height function; for example, for a 2D water wave. Eq. (3.21) has the same form as Eq. (2.1) if $F=y-h(x,t)$. It follows that the instantaneous rate of variation of F for a surface-particle must be zero provided that the flow is continuous and there is no flow of fluid across the free surface. Thus, we have[51, 57]

$$\frac{\partial F}{\partial t}+\left(\vec{V}\cdot\nabla\right)F=0 \tag{3.22}$$

where $\vec{V}$ is the velocity of fluid in the interfacial region with respect to a reference coordinate system. The physical explanation of Eq. (3.22) is that any particle lying in the surface only moves tangentially to the surface or remains still relative to it[58].

Like the algorithm for the momentum equation in Section 3.4, the VOF function is solved in two steps[10]. The Hirt-Nichols (H-N) algorithm is employed for the advection of VOF function. A donor-acceptor approximation for the fluxes in the H-N algorithm retains VOF function's discontinuous nature without smearing the function. The method is applicable to both 2D and 3D free surface problems and its advantage of minimum storage requirements is highly valuable compared with the marker particle method or other free surface tracking methods. However, the VOF method is a piecewise linear and stair-stepped algorithm[59].

3.3 Continuum Surface Force (CSF) Model

Surface tension force is believed to result from molecular interactions within a very thin transitional region between two fluids. When a water strider stands or walks on a water surface, the water surface supports the insect by surface tension force, which is distributed over the deformed area. The surface tension force is thus modeled as a continuous volume force existing only over the curved area to a very thin depth.

We define a characteristic *color function* $c(\vec{x})$ to distinguish two fluids:

$$c(\vec{x}) = \begin{cases} c_1, & \text{in fluid 1;} \\ c_2, & \text{in fluid 2;} \\ > c_1, < c_2, & \text{at the interface.} \end{cases} \tag{3.23}$$

A mollified color function $\tilde{c}(\vec{x})$ varies smoothly over a thickness h across the interface, if it is obtained by convolving the characteristic function $c(\vec{x})$ with an interpolation function φ:

$$\tilde{c}(\vec{x}) = \frac{1}{h^3} \int_V c(\vec{x'})\varphi(\vec{x} - \vec{x'})dx'^3, \tag{3.24}$$

where φ is a normalized bounded and differentiable interpolation function, e.g., B-spline function[60] according to [14]. The color functions satisfy

$$\lim_{h \to 0} \tilde{c}(\vec{x}) = c(\vec{x}). \tag{3.25}$$

Therefore, the volumetric surface tension force $\vec{F}_{\text{sv}}$ is given:

$$\vec{F}_{\text{sv}}(\vec{x}) = \sigma\kappa(\vec{x}) \frac{\nabla\tilde{c}(\vec{x})}{[\![c]\!]}, \tag{3.26}$$

where the jump of color between two fluids $[\![c]\!]$ is equal to 1.0 if $c = F$[16].

Lafaurie et al[17] designed a surface tension tensor similar to the viscous tensor in the Navier-Stokes equation.

In the CSF model, the sharp color function c is mitigated to be a smoothed function $\tilde{c}$ using Eq. (3.24). Then the mollified color function $\tilde{c}$ is optionally used in finite difference schemes for calculating surface normal and curvature, and surface tension force. In the computations, $\hat{n}$ is calculated by setting $\tilde{c} = \rho$ and κ is calculated by setting either $\tilde{c} = \rho$ or $\tilde{c} = \tilde{\rho}$, where $\tilde{\rho}$ is a smoothed density convolved with quadratic B-spline $\varphi^{(l)}$ of degree l. Notice $\tilde{c} = \rho$ is equivalent to $\tilde{c} = F$ from Eq. (3.20).

B-spline function with second degree $\varphi^{(2)}(|\vec{x} - \vec{x}'|; h)$ is chosen in RIPPLE[16] to estimate the smoothed density at cell (i, j) by interpolating the densities at the eight neighboring cell centers with the one at the grid cell center itself:

$$\tilde{\rho}_{i,j} = \sum_{i',j'=-M,-N}^{M,N} \rho_{i',j'} \varphi^{(2)}(|x_{i,j} - x_{i',j'}|; h) \varphi^{(2)}(|y_{i,j} - y_{i',j'}|; h), \tag{3.27}$$

where $\varphi^{(2)} \neq 0$ for $|\vec{x} - \vec{x}'| < (l+1)h/2 = 3h/2$ and h is the thickness across the interface as shown in Figure 5.5. The convolution kernel function in Eq. (3.27) $\varphi^{(2)}(|x_{i,j} - x_{i',j'}|; h)\varphi^{(2)}(|y_{i,j} - y_{i',j'}|; h)$ gives weight parameters in the density interpolation at cell (i, j); for example, the 3×3 stencil matrix in Eq. (B.23). Unfortunately, the mollified color function by Eq. (B.23) is unable to yield accurate evaluations for surface normal, surface curvature, and integral continuous surface tension force, and so is the mollified VOF function.

3.4 Numerical Approach

We solve the governing equations using finite difference approximations, which are second-order accurate in space and first-order accurate in time. A two-step projection method is adopted to solve Eqs. (3.1) and (3.2). The momentum equation, namely Eq. (3.2), is thus split into two parts through a dump velocity $\tilde{\vec{V}}$:

$$\frac{\tilde{\vec{V}} - \vec{V}^{\mathrm{n}}}{\delta t} = -\nabla \cdot \left(\vec{V}\vec{V}\right)^{\mathrm{n}} + \frac{1}{\rho^{\mathrm{n}}} \nabla \cdot \tau^{\mathrm{n}} + \vec{g}^{\mathrm{n}} + \frac{1}{\rho^{\mathrm{n}}} \vec{F}_{\mathrm{b}}^{\mathrm{n}}, \tag{3.28}$$

and

$$\frac{\vec{V}^{\mathrm{n}+1} - \tilde{\vec{V}}}{\delta t} = -\frac{1}{\rho^{\mathrm{n}}} \nabla p^{\mathrm{n}+1}. \tag{3.29}$$

The combination of Eq. (3.29) and the continuity equation,

$$\nabla \cdot \vec{V}^{\mathrm{n}+1} = 0, \tag{3.30}$$

produces the pressure Poisson equation (PPE),

$$\nabla \cdot \left[\frac{1}{\rho^{\mathrm{n}}} \nabla p^{\mathrm{n}+1}\right] = \frac{\nabla \cdot \tilde{\vec{V}}}{\delta t}. \tag{3.31}$$

The procedure to reach the solution of flow field by advancing one time step δt is shown in Figure 3.1 and outlined briefly as follows:

1. In the first step, $\tilde{\vec{V}}$ is computed as a result of advection, viscous force, gravitational acceleration, and body forces (see Eq. (3.28)) from the previous time level n or the initial conditions.

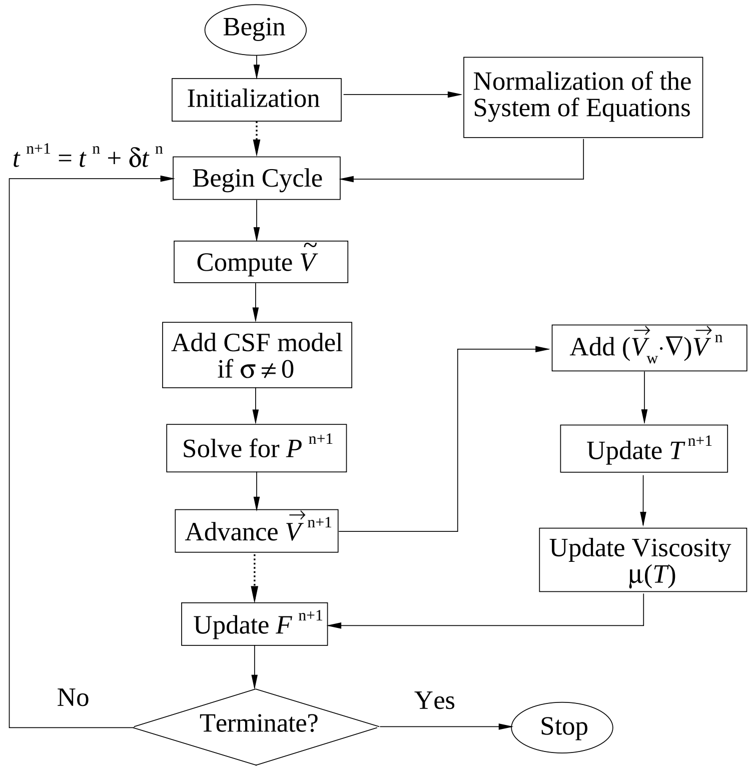

Figure 3.1 Flow chart of the numerical approach

2. In the second step, the velocity field of $\tilde{\vec{V}}$ is projected onto a zero-divergence vector field by Eq. (3.31); the pressure at the time level n+1 is thus obtained via a robust incomplete Cholesky conjugate gradient (ICCG) technique. Then the velocity field at the time level n+1 is updated from the previous time level by solving Eq. (3.29).

3. In the third step, if temperature is desired in the simulation, Eq. (4.2) is solved. The viscosity is then updated for the alloy using the Vogel-Fulcher-Tammann formula Eq. (4.24).

4. Meanwhile, F is updated by solving Eq. (3.22). The surface configuration is represented by the updated F; accordingly, surface normal and curvature are computed for the next time level from the gradients of F by Eqs. (3.12), (3.11), and (3.10).

Repetition of these steps utilizing explicit schemes will present the variation of flow field. Prior to each time advance, a new time step is chosen to meet the requirements of numerical stability (discussed later in Section 3.6).

3.5 Grid Generation

A collection of discrete points in a physical field should be properly selected to allow finite difference schemes or other numerical methods to yield convergent numerical solutions to the flow. A layer of fictitious cells, namely ‘ghost’ cells, as shown in Figure 3.2, is generated around the meshes of the computational domain, with particular velocity and pressure distributions in accordance with the desired boundary conditions.

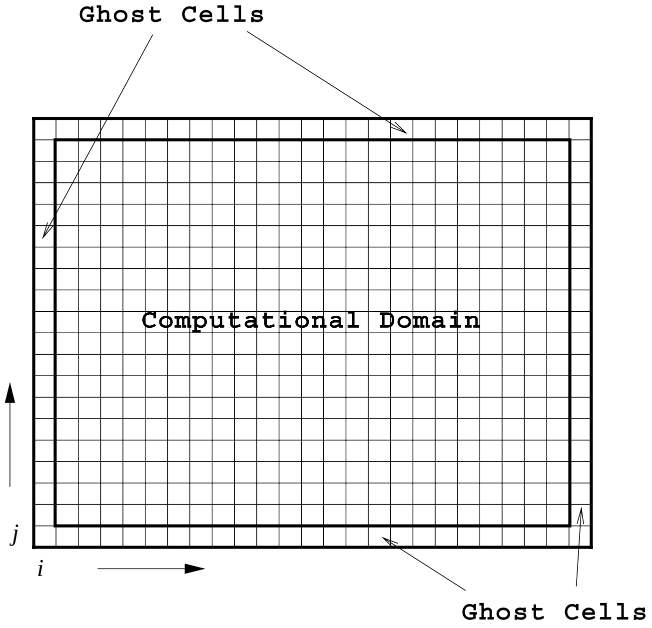

Figure 3.2 Diagram of grids and fictitious cells

In the simulation, structured grids are generated using an algebraic method, in which the cell spacing is quadratically incremented on both sides from a so-called convergence point. The grid spacing for a cell directly adjacent to the convergence point is equal to the user-specified minimum value. Other grid spacings depend on the desired cell number. The submeshes are separately generated between two convergence points, which are assigned by users in advance so that linking these submeshes can achieve arbitrary variable cell spacings. This enables us to generate finer meshes in the subregions where flow is expected to change abruptly so that the numerical solutions may reflect the actual flow variation with economical storage and computation. However, large disparities in cell spacing should be avoided across submeshes and within a submesh itself. In general, the difference of adjacent cells must be less than 10 $\sim$ 20% and cell aspect ratios $(\delta x/\delta y)$ are restricted to between 1/2 and 2. A uniformly spaced mesh can also be generated. The grid cell size is given as

$$\delta x_i = x_{i+1/2} - x_{i-1/2}, \qquad \delta y_j = y_{j+1/2} - y_{j-1/2}, \tag{3.32}$$

where i and j are indices along the x- and y-directions, respectively, and $x_{i+1/2}$, $x_{i-1/2}$, $y_{j+1/2}$, and $y_{j-1/2}$ indicate the right, left, top, and bottom face of a grid cell, respectively.

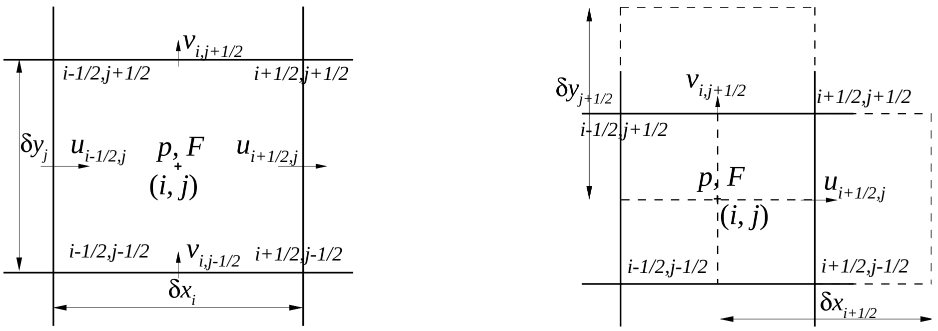

(a) Location of flow variables and VOF function in a grid cell (i, j)

(b) Control volumes on a staggered grid

Figure 3.3 Illustration of a grid cell and a control cell

We adopt staggered grid for flow field, on which p and F are located at the center of a grid cell (i, j) (also called mass control volume) and the velocities $(u, v)^{\mathrm{T}}$ are located on the face of a grid cell other than at the center as shown in Figure 3.3. The horizontal and vertical momentum control volumes are sketched in the dashed lines, respectively, in Figure 3.3(b). Accordingly, the momentum control volumes in the two orthogonal directions have

$$\delta x_{i+1/2} = \frac{1}{2}(\delta x_i + \delta x_{i+1/2}), \qquad \delta y_{j+1/2} = \frac{1}{2}(\delta y_j + \delta y_{j+1/2}), \tag{3.33}$$

respectively, which are not identical to the grid cell size if the grid spacings are not uniform in each direction.

Harlow and Welch[20] first implemented staggered grid; it can not only prevent a wavy velocity field and checkerboarding[61], it also yields relatively high accuracy[62].

Sensitivity analysis of a solution to the grid is intended to seek an acceptable grid on account of computing time, memory requirements, and numerical stability.

3.6 Numerical Stability

Only based on a stable scheme is a plausible numerical solution able to explain a given engineering problem. Errors from truncation, round-off, or any other sources are not allowed to grow or oscillate largely and frequently in space, time, or both in any CFD simulation. To obtain a stable numerical solution, certain restrictions must be imposed in choosing the mesh increments δx_i and δy_j, the time increment δt, and the upstream differencing parameter α (see [16]). The time restrictions to the explicit algorithms in the numerical approach are outlined as follows.

(1) The limitation of finite difference approximation that fluxes of momentum and F only take place between adjacent cells finds the famous *Courant-Friedrichs-Lewy condition* (CFL) in which a *Courant number* C must be less than unity. Time step must satisfy the following constraint in the both directions of a cell:

$$\delta t = \min\left(C\left[\frac{\delta x_i}{|u_{ij}|}\right],\ C\left[\frac{\delta y_j}{|v_{ij}|}\right] \right), \tag{3.34}$$

where Courant number C is defaulted to 0.3 in the computer codes or altered by the user to any value less than 1.0. The CFL condition requires that the analytic domain of influence lie within the numerical domain of influence[63], or that the numerical advancing time step is small enough for a fluid and its free surface will travel only within a mesh cell.

(2) The momentum due to viscous force diffuses no more than one cell for the same reason implied in finite difference approximation. The explicit treatment of viscous stress tensor evaluation subject to a linear stability analysis gives time step

$$\delta t < \min\left(\frac{1}{2\nu}\frac{\delta x_i^2 \delta y_j^2}{\delta x_i^2 + \delta y_j^2} \right), \tag{3.35}$$

where $\nu = \mu/\rho$ is non-zero kinematic viscosity, and the fractional value 1/2 can be set to 1 or less, e.g., 1/3, for a more conservative estimation of time increment.

(3) In the CSF model, the surface tension at time t^{n} as a body force is represented by surface tension; it satisfies the following inequality for a time step marching so that the linear stability is maintained in resolving the propagation of capillary waves:

$$\delta t < \min \left[\frac{\rho \delta x_i^{3/2} \delta y_j^{3/2}}{4\pi\sigma} \right]^{1/2} . \tag{3.36}$$

Implicit surface tension algorithms are investigated by Williams[64] and Hou[65] to alleviate the restrictive constraint of surface tension[19].

(4) If thermal-energy within the flow field is considered, the time increments are evaluated based on non-zero thermal diffusivity analogous to the restriction in (2)[39] as follows:

$$\delta t < \min \left(\frac{1}{2\alpha} \frac{\delta x_i^2 \delta y_j^2}{\delta x_i^2 + \delta y_j^2} \right), \tag{3.37}$$

where the fractional value 1/2 can be any value less than 1.0 and α is thermal diffusivity.

3.7 Wall Adhesion

Wall adhesion refers to surface force exertion on a fluid interface at the contact line where two immiscible fluids and a solid meet together. Wall adhesion force is estimated in the same manner as in Eq. (3.8) for volumetric force of surface tension. A boundary condition is applied to the free surface with a contact angle θ:

$$\hat{n} = \hat{n}_{\mathrm{w}} \cos\theta + \hat{t}_{\mathrm{w}} \sin\theta, \tag{3.38}$$

where θ can be a static or a dynamic contact angle, and $\hat{n}_{\mathrm{w}}$ and $\hat{t}_{\mathrm{w}}$ are wall unit normal and tangential, respectively, as shown in Figure 3.4. The normal and curvature in Eq. (3.8) are accordingly adjusted at a contact line.

Obviously, a moving contact angle θ_{M} is more appropriate to a moving contact line. However, we assume in the simulations that θ remains constant, namely the moving contact angle θ_{M} is equal to the static contact angle θ_{S}. The error of wall adhesion is tolerable only when θ_{S} or the difference between θ_{S} and θ_{M} is small.

In reality, the contact angle θ varies with the local wall and fluid conditions, i.e., velocity, viscosity, and surface tensions. The moving angle is at least correlated to the static contact angle[57, 66, 67] and capillary number

$$\mathbf{Ca} \equiv \frac{U\mu}{\sigma}, \tag{3.39}$$

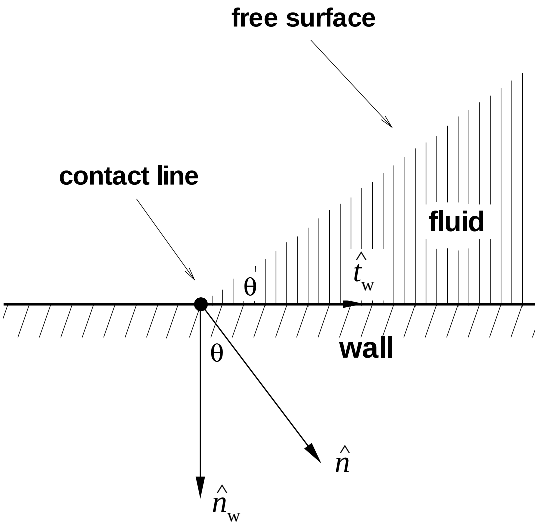

Figure 3.4 Wall adhesion boundary condition

where U is the contact line velocity. Hoffman (1975)[66] gave an empirical correlation for θ_{M} with $\mathbf{Ca}$ and θ_{S}. Dussan points out that Hoffman's correlation does not agree with the data of Blake & Haynes (1969)[68]. A more accurate moving contact angle is desired to be well characterized in computations.

CHAPTER 4 HEAT TRANSFER AND RAPID SOLIDIFICATION OF ALLOY

Section 4.1 presents the thermal-energy equation and various thermal boundary conditions on a solid wall. A formula is discussed in Section 4.2 for computing temperature gradients on the faces of interfacial cells. Section 4.3 prepares the homogeneous and heterogeneous nucleation theory for predicting the nucleation temperature and critical cooling rate in Chapter 7.

4.1 Thermal-Energy Equation

The thermal-energy equation can be written as follows[69, 70]:

$$\frac{\partial e}{\partial t} + \nabla \cdot (\vec{V} e) = -p \nabla \cdot \vec{V} + \tau : \nabla \vec{V} - \nabla \cdot \vec{q}, \tag{4.1}$$

where $e = \rho C_p T$ is the internal energy per unit volume, C_p is the specific heat of fluid, and the symbol ':' denotes a double inner product of tensor. For an incompressible Newtonian flow far from free surface, Eq. (4.1) reduces to

$$\frac{\partial T}{\partial t} + \nabla \cdot (\vec{V} T) = \left(\frac{2\nu}{C_p} \right) \mathbf{S} : \nabla \vec{V} + \alpha \nabla^2 T \tag{4.2}$$

where $\mathbf{S}$ is the rate-of-strain tensor (see Eq. (3.7)). The thermal diffusivity α in Eq. (4.2) has the same unit of fluid kinematic viscosity ν and

$$\alpha \equiv \frac{k}{\rho C_p} \tag{4.3}$$

where k is heat conductivity. In Eq. (4.2), the heat flux vector $\vec{q}$ obeys Fourier's heat-conduction law for an isotropic flow such that

$$\vec{q} = -k \nabla \cdot T. \tag{4.4}$$

Notice that in Eq. (4.2) the work due to deformation of fluid $-p\nabla \cdot \vec{V}$ vanishes simply because of the assumption of incompressibility (see Eq. (3.1)). A dimensionless parameter *Prandtl number* **Pr** describes the ratio of kinematic viscosity to thermal diffusivity:

$$\mathbf{Pr} \equiv \frac{\nu}{\alpha}. \tag{4.5}$$

Two explicit finite difference schemes are given in Appendix A for both conservative and nonconservative forms of heat convection in Eq. (4.2) at a grid cell fully occupied with **fluid 2**. In the numerical schemes, the temperature T is located at the center of each grid cell as shown in Figure 4.1. Unlike in the algorithms for momentum convection, grid cells are chosen as the control volumes to estimate heat convection.

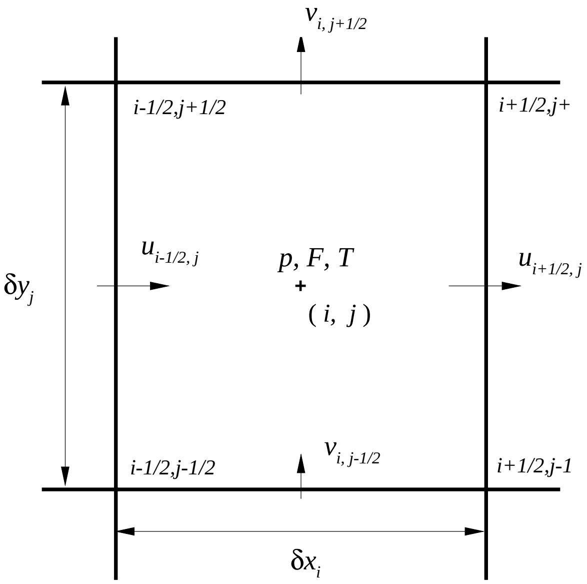

Figure 4.1 Temperature at center of a grid cell (i, j)

The thermal initial condition to Eq. (4.2) is

$$T(\vec{x}, 0) = T_0(\vec{x}). \tag{4.6}$$

Various thermal boundary conditions are listed in Table 4.1 according to Newton's law of cooling,

$$q_{\text{wall}} = -k\frac{\partial T}{\partial n} = h\left(T_{\text{w}} - T_{\infty}\right), \tag{4.7}$$

where n represents the wall normal.

The velocity gradients $\partial u/\partial x$ and $\partial v/\partial y$, for example, in the viscous dissipation terms as in Eqs. (4.2), (5.54), (C.1), and in the rate-of-strain tensor $\mathbf{S}$ as in Eq. (3.7) are estimated at the center of each grid, whereas $\partial u/\partial y$ and $\partial v/\partial x$ are computed by averaging those at four vertices of each grid.

KTB KTT KTL KTR	Thermal Boundary Condition
1	Applied wall temperature T_{w}
2	Applied heat flux (may be zero)
3	Given heat transfer coefficient
4	Continuative temperature (zero heat flux) $\partial T/\partial n = 0$

Table 4.1 Values of flags (KTB, KTT, KTL, and KTR) and the corresponding types of thermal boundary condition

Some formulations of the thermal-energy equation and boundary conditions on free surface in the Cartesian and cylindrical coordinate systems are shown in Appendix C.

4.2 Formulation of Temperature Gradients in Interfacial Cells

The thermal boundary conditions on free surface Eq. (2.27) are applied in the computation of temperature gradients for the thermal-energy equation. Eq. (2.27) is written in vector form,

$$-k\nabla T = -\vec{q}_{\mathrm{loss}}, \tag{4.8}$$

where $\vec{q}_{\mathrm{loss}}$ is given:

$$\vec{q}_{\mathrm{loss}} = [h(T - T_{\mathrm{a}}) + \epsilon\sigma_{\mathrm{SB}}(T^4 - T_{\mathrm{a}}^4)]\hat{n}, \tag{4.9}$$

with a known ambient temperature T_{a}.

Because the temperature is continuous within a flow, the temperature gradient at a control cell center is computed using finite difference scheme between two immersed grid cell centers. On the face of an interfacial cell as shown in Figure 5.7 in the x-direction, for example, the temperature gradient is evaluated as follows:

$$\frac{\partial T}{\partial x} = \frac{1}{k}[h(T - T_{\mathrm{a}}) + \epsilon\sigma_{\mathrm{SB}}(T^4 - T_{\mathrm{a}}^4)]\hat{n}_x, \tag{4.10}$$

where T is the temperature at the control cell center. Likewise, in the y-direction it is estimated by

$$\frac{\partial T}{\partial y} = \frac{1}{k}[h(T - T_{\mathrm{a}}) + \epsilon\sigma_{\mathrm{SB}}(T^4 - T_{\mathrm{a}}^4)]\hat{n}_y. \tag{4.11}$$

T in Eqs. (4.10) and (4.11) can approximately be equal to the temperature at the neighboring immersed grid cell center if the grid cell center is not immersed. $\hat{n}_x$ and $\hat{n}_y$ in Eqs. (4.10) and (4.11) can be computed by the DA algorithm introduced in Section 5.2 of Chapter 5.

Then the temperature over the entire flow field is estimated by an explicit upwind finite approximation in Appendix A. All the temperature is imposed to be T_{a} at those grid cell centers having $F < 0.5$.

4.3 Rapid Solidification and Nucleation Theory

It is widely accepted that a phase change from liquid to solid, *solidification*, involves heat (and also mass) transfer, release of latent heat, changes in thermophysical properties, and surface effects[52]. Associated with latent heat, first-order phase transitions are characterized by specific volume and discontinuous change in specific entropy or enthalpy at a transition point, e.g., the equilibrium melting temperature T_m in solidification. The latent heat of fusion L is extracted in solidification or absorbed by material while melting at T_m:

$$\rho L = e_L(T_m) - e_S(T_m), \tag{4.12}$$

where e is the enthalpy of a liquid or solid state. In equilibrium solidification, the latent heat can also be derived by the jump of *Gibbs free energy* between two states[71],

$$\rho L = \Delta S T_m, \tag{4.13}$$

where ΔS is the entropy of fusion.

In a crystalline solid, the atoms or other particles are arranged in a repetitive lattice structure over a long range in the atomic scales. Unlike a crystalline solid, an amorphous (glass) or non-crystalline solid has a disordered microstructure, upon which it exhibits some different desirable properties, such as corrosion resistance and catalysis. Amorphous materials form only when crystallization is suppressed. Rapid cooling is among those means of manufacturing an amorphous material because it reduces the mobility of atoms or molecules before they move into the solid lattice structure.

An *undercooled* (also called *supercooled*) liquid is found, for example, when a molten metal or alloy remains a liquid state below T_m with no solid formation. The interfaces between liquid and solid states in undercooling appear as transitional regions with non-zero thickness and the microstructures range among columnar, dendritic, and amorphous forms depending on external solidification conditions, surface tension and curvature (*Gibbs-Thomson effect*), and material properties. The morphologies of undercooling liquid/solid interface differ from those of pure materials in equilibrium solidification. The latter can be approximated as planar and with negligible thickness.

The undercooled melt with an undercooling amount $\Delta T = T_m - T$ is a thermodynamically metastable system with higher free energy than the solid state at equilibrium temperature T_m. The difference in free energy ΔG provides a kinetic (also called driving force) for the system to solidify:

$$\Delta G = G^{(L)} - G^{(S)} \tag{4.14}$$

where G is Gibbs free energy and the superscripts (L) and (S) denote liquid and solid states, respectively[71].

However, ΔG might not be expected to result in solidification unconditionally. The melt must cool enough to overcome the nucleation barrier before it creates a stable growth process of solidification. All crystallization processes start with a nucleation event in liquid. A critical free energy difference ΔG_c can be derived theoretically for homogeneous nucleation process in absence of impurities:

$$\Delta G_c = \left(\frac{16\pi\sigma_{LS}^3 T_m^2}{3\rho^2 L^2}\right) \cdot \frac{1}{\Delta T^2} \tag{4.15}$$

where σ_{LS} is the surface tension or surface energy per unit area of the melt at the interface between liquid and solid. It can be estimated using latent heat of fusion L in J/mol, as follows[72–74]:

$$\sigma_{LS} = \frac{\alpha L}{N^{\frac{1}{3}} V_a^{\frac{2}{3}}}, \tag{4.16}$$

where $\alpha = 0.46 \sim 0.64$ is a dimensionless parameter for crystal/melt interfacial energy, the Avogadro's number $N = 6.022 \times 10^{23}$, and V_a is the atomic volume of melt. α is the number of monolayers/area of crystal, which would be melted by an amount of heat equivalent to σ_{LS} in physics[74].

If the Gibbs free energy is greater than ΔG_c, a spherical nucleus forms in the undercooled melt with a radius greater than the corresponding critical value R_c:

$$R_c = \frac{2\sigma_{LS} T_m}{\rho L} \frac{1}{\Delta T}. \tag{4.17}$$

For heterogeneous nucleation as shown in Figure 4.2, the activation energy barrier ΔG_c is lowered by a shape factor $f(\theta)$:

$$\Delta G_c = \left(\frac{16\pi\sigma_{LS}^3 T_m^2}{3\rho^2 L^2}\right) \cdot \frac{1}{\Delta T^2} \cdot f(\theta) \tag{4.18}$$

where $f(\theta) < 1$ is given in the form of a wetting angle (or called contact angle) θ with the container wall or a substrate:

$$f(\theta) = \frac{1}{4}(1 - \cos\theta)^2(2 + \cos\theta). \tag{4.19}$$

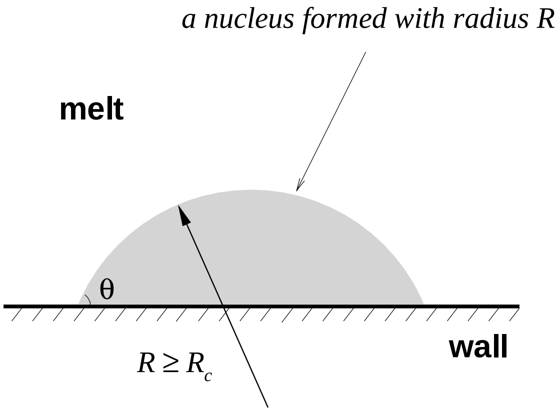

Figure 4.2 Heterogeneous nucleation due to container wall

Eqs. (4.15), (4.17), (4.18), and (4.19) show the energy barrier ΔG_c is greatly lowered by larger undercooling ΔT, foreign particles, or container walls.

Once the melt begins to nucleate, a nucleus grows very quick. It takes 10^{-4} s for alloy Fe_{75}-Si_{10}-B_{15} (at.%) to form crystalline state of the material, for instance, as illustrated in Figures 7.3 and 7.2.

The nucleation frequency or rate I_v (number of nuclei appearing per unit volume in unit time) takes a Boltzmann form from the viewpoint of statistical mechanics[4, 75]:

$$I_v = N_v \nu_a \exp\left[-\frac{\Delta G_c}{k_{\mathrm{B}} T}\right] \tag{4.20}$$

where $N_v = N/V_a$ is the number of atoms (or molecules) per unit volume, the Boltzmann constant $k_{\mathrm{B}} = 1.3806505 \times 10^{-23}$ J/K, and ν_a atomic jump frequency. ν_a can be estimated by the the Stokes-Einstein relation:

$$\nu_a = \frac{k_{\mathrm{B}} T}{3\pi d_m^3 \mu}, \tag{4.21}$$

where d_m is the effective molecular diameter to be approximated as a molecular jump distance or interatomic spacing.

Eq. (4.20) takes another form as follows after the magnitude estimation of the prefactor:

$$I_v = \frac{K_v}{\mu(T)} \exp\left[-\frac{\Delta G_c}{k_{\mathrm{B}}T}\right] \tag{4.22}$$

where K_v is the kinetic parameter for nucleation (10^{39} N/m^5[42, 73, 74]).

Also, for a heterogeneous nucleation with a surface contact area of nuclei S, the nucleation rate becomes

$$I_s = \frac{K_s}{\mu(T)} \exp\left[-\frac{\Delta G_c}{k_{\mathrm{B}}T}\right] \tag{4.23}$$

where K_s is the kinetic parameter for nucleation (10^{29} N/m^4[42, 73, 74]). With the properties in Section 7.1 of Chapter 7, K_v and K_s can be estimated to be of the same order as above, respectively. The dynamic viscosity $\mu(T)$ in Eqs. (4.21), (4.20), and (4.23) is approximated by the Vogel-Fulcher-Tammann formula,

$$\mu = \mu_0 \exp\left(\frac{bT_m}{T - T_g}\right), \tag{4.24}$$

where μ_0, b, and T_g are empirical constants and T_g is the so-called glass temperature. μ_0 is the high temperature limit of viscosity given by

$$\mu_0 = \frac{h}{V_a/N} \tag{4.25}$$

where h is Planck's constant (6.626068×10^{-34} m^2kg/s) and V_a/N is the volume of an atom of liquid[76].

According to [4] and [77], the dynamic viscosities of metallic melts experience a substantial discontinuous increase over 20 orders of magnitude on crystallization, whereas they vary continuously from $1 \sim 0.1$ kg/ms above T_m in liquidus states to 10^{12} kg/ms in glass formation when supercooling near amorphous temperature T_a or glass temperature T_g. The solid state is defined arbitrarily to have greater than 10^{14} kg/ms viscosity[77].

Estimation of the critical or the minimum cooling rate and nucleation temperature can be performed based on the nucleation frequency I associated with Eq. (4.22) or (4.23) and the integral follows:

$$n = \int_{T_m}^{T_n} \frac{I(T)}{\dot{T}} dT = \int_0^{t_n} I dt = 1 \tag{4.26}$$

where n is the total number of nuclei formed in the undercooled volume of V during time t_n when the temperature drops to the nucleation temperature T_n, and

$$I = I_v V \qquad \text{or} \qquad I = I_s S = \left(\frac{S}{V}\right) I_s V, \tag{4.27}$$

where V is the spherical volume of a molten drop. The nucleation temperature T_n can be defined as the temperature at which at least one nucleation event should take place in a unit volume of the undercooled melt. It is the onset temperature at which the melt begins to solidify. The ratio $S/V\ m^{-1}$ and the radius of 10 μm for the spherical volume V have been given in [42, 43]. In this work, the characteristic volume is chosen as

$$V = \frac{V_a}{N \times 1\%} = 100 \times \frac{1}{6}\pi d_m^3 \tag{4.28}$$

which is equivalent to the volume occupied by 100 atoms or molecules of the material (see Eq. (7.2)). Then the nucleation temperature is regarded as the temperature at which 1% of the atom or molecule per unit volume begins to nucleate. Accordingly, the catalyst contact area S can be computed by

$$S = V^{\frac{2}{3}} = \Delta x^2, \tag{4.29}$$

where Δx is the characteristic length relating to the characteristic area S (see Figure 7.1). It is found that Δx is approximately four times the effective molecular diameter d_m since $\Delta x = 3.741 d_m$ from Eqs. (4.28) and (4.29). The characteristic length Δx of control area or volume ranges between $4 \sim 5\ d_m$ as in Table 4.2. For a circular or spherical control area/volume, we often choose the diameter as the characteristic length Δx. Notice Δx has nothing to do with the critical radius R_c.

Control area or volume	Δx
Squared or cubic	$3.741 d_m$
Circular	$4.234 d_m$
Spheric	$4.642 d_m$

Table 4.2 Characteristic lengths for various geometries of control volume

If the control area or volume is integrated by time using $\Delta x = Ut$, T_n can also be found as the 'nose' location in a curve called the Temperature Time Transformation (TTT) diagram and plotted by the integration as

$$x = \frac{1}{3}\pi I_v U^3 t^4, \tag{4.30}$$

where x is a fraction crystallized with time to some lower limit of detectability of crystallization, e.g., $x = 10^{-6}$[4, 78] or 1%[79], and U is the growth rate of crystallization. The TTT diagram can also be obtained from experiments. The critical cooling rate is computed from either TTT diagram or Continuous Cooling Transformation (CCT) diagram. The power index of t in Eq. (4.30) is given $1 \sim 4$ according to [78].

The classical continuous growth U of the crystal front in Eq. (4.30) is given from the atomistic theories[4] or experiments[80]:

$$U = \frac{D_L}{d_m}\left[1 - \exp\left(-\frac{V_a \rho L \Delta T}{N k_{\mathrm{B}} T T_m}\right)\right], \tag{4.31}$$

where D_L is the liquid self-diffusivity calculated using

$$D_L = \nu_a d_m^2. \tag{4.32}$$

The driving force in Eq. (4.31) is proportional to the undercooling ΔT and the latent heat L. From Eqs. (4.31), (4.32), and (4.21), one may find the reason an alloy easily forms an amorphous phase in contrast with the pure metal. An alloy has lower crystal growth rate than the pure metal simply because it has greater viscosity and larger d_m. Accordingly, if the grain growth of an alloy from the substrate is unable to keep up with the imposed solidification rate, namely undercooling, crystallization by the grain growth will not occur even when the undercooling is not high[1].

CHAPTER 5 IMPROVEMENTS IN THE NUMERICAL APPROACH

From the image processing and Fourier transform theories, as discussed in Section 5.1, a new interpolation function convolving with VOF or color function improves the accuracy and facilitates the computation. Then a direct accurate algorithm for surface normal and curvature of free surface is developed in Section 5.2. Grid and control cells are classified into empty, interfacial, sublayer, and interior cells according to their distances to free surface in Section 5.3. Immersed length is introduced in the estimations of density and volumetric surface tension force at the control cell center. The section also discusses an estimation of viscous force on free surface. In Section 5.4, I make some corrections to the approach for solving pressure on interfacial cells. Additional translation terms that emerge in a moving Eulerian system appear in Section 5.5. These terms are necessary in the numerical simulation of melt spinning. Finally, scalings of the equation system and the boundary and the initial conditions are contained in Section 5.6.

5.1 Convolution in Image Processing

In the image processing theory, *Whittaker Shannon sampling theorem* [81–83] states that a 2D continuous bandlimited function with frequency B_x and B_y, respectively, can be fully specified by samples on a grid with spacings, if satisfying

$$\delta x \leqslant \frac{1}{2B_x} \quad \text{and} \quad \delta y \leqslant \frac{1}{2B_y}, \tag{5.1}$$

where δx and δy are samples' spacings in the two directions. Quantity $1/2\delta x$ is called *Nyquist frequency* in the x-direction, and so is $1/2\delta y$ in the y-direction. Apparently, the Nyquist frequencies increase when the grids are refined; then the edge of an image or a free surface is enhanced.

Like a signal, a sharp image edge and a free surface are both seen to have higher frequencies on the frequency domain by *Fourier transform* (see Eq.(6.20)). In fact, it is impossible to fully reconstruct a zero-thickness free surface by a series of discrete samples, because the band limits B_x and B_y are otherwise infinite and the free surface is no longer bandlimited. If the transitional thickness is zero, Eq. (5.1) is not satisfied and no grid can be found for a discrete F to describe such a free surface. It demonstrates that a discrete function of 2D fractional area, for example, F is unable to represent a continuous line segment before this line is approximated as a very thin band of area, as shown in Figures 5.1 and 5.5. In the CSF model, F actually describes a thin band of area in the transitional region so that the continuum surface force per unit volume in 3D, or per unit area in 2D, can substitute a surface tension force per unit length.

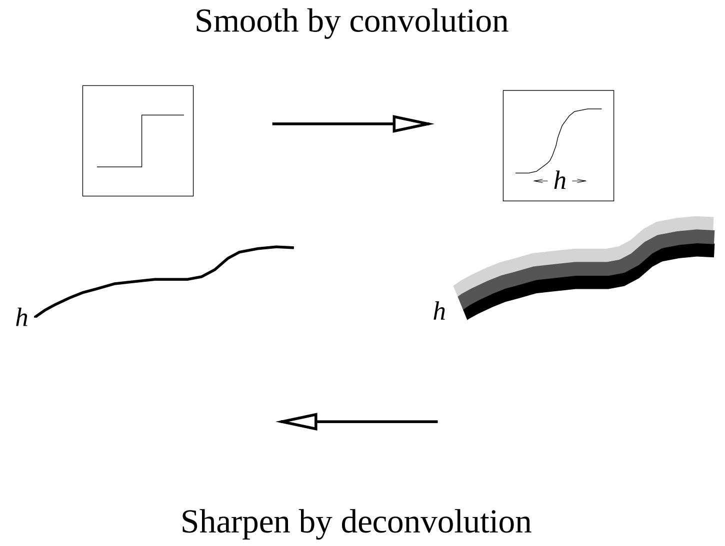

Figure 5.1 Image processing: convolution and deconvolution

Even if a free surface is modeled as a thin transitional layer, which can be represented by a bandlimited continuous function, e.g., F function, the grid sizes δx and δy are chosen from CFD criteria such as the CFL condition and other restrictions as in Section 3.6 of Chapter 3, other than from B_x and B_y in Eq. (5.1). Therefore Eq. (5.1) may not be satisfied and a folding back phenomenon, called *aliasing* in image processing, may occur and incur *spurious currents.* To preclude aliasing one may either choose smaller grid sizes or narrow frequency bandlimits.

Obviously, blocking higher frequency is an efficient way of reducing the spurious currents caused by aliasing errors. The operation of blocking higher frequency is called *blurring* or *smoothing* an image, which can be manipulated by a lowpass filter or averaging the local grey level in image processing. Blurring or smoothing the discrete F or c may in turn broaden the transitional layer up to a number of cell sizes; thus it may lower the frequency bandlimits of free surface. Meanwhile, the smoothed VOF and color functions may yield better finite difference approximations in the evaluations of surface normal and curvature. VOF and color functions are believed to inherently produce some noises because they are not smoothed in the normal direction. However, in the inclined surface example, by convolution with some selected functions, the sharpness and periodicity of VOF function can be alleviated. A kernel function is thus chosen to convolve with density, color, and VOF functions as shown in Figure 5.1.

Various lowpass filters are qualified to meet the design requirements essentially from the convolution theorem (refer to [81–83]). The 2D discrete form of convolution of two functions is written to approximate the convolution integration as follows:

$$\tilde{c}_{i,j} = c_{i,j} * k_{i,j} = \sum_{i',j'=-\infty}^{\infty} c_{i',j'} K(\vec{x}_{i,j} - \vec{x}_{i',j'}), \tag{5.2}$$

where $K(\vec{x} - \vec{x}')$ is called *convolution mask* or *stencil.* Because the convolution function vanishes beyond a finite region, various sizes with equal finite number of discrete samples in each direction $N \times N$ is instead selected for the convolution mask and the summation in Eq. (5.2).

Then different types of transfer functions can create various filters[82, 84]. Fast Fourier Transform (FFT) technique is applied in the numerical computation of $\tilde{c}(x, y)$. An exponential transfer function is often implemented because exponential functions (also called Gaussian functions) remain in identical form in spatial and frequency domains. However, an efficient and simple smoothing commonly used in blurring images is neighborhood averaging, which can also be introduced in blurring free surface. If 3×3 is given for the local average mask size, the constant $1/9$ is yielded as the convolution function K in Eq. (5.2), which follows

$$\frac{1}{9}\begin{array}{|c|c|c|}\hline 1 & 1 & 1 \\ \hline 1 & 1 & 1 \\ \hline 1 & 1 & 1 \\ \hline \end{array}. \tag{5.3}$$

Undoubtedly, the mollified color function by Eq. (5.3) is the mean value of 3×3 cells.

The mask for lowpass filter can be extended to any size of $N \times N$. In fact, it is not desired to be greater than 15×15 for the sake of computation. The convolution of color function $c(\vec{x})$ with 1×1 smooth kernel is the discretization of Heaviside function.

The orientation and the curvature of an image or free surface are not destroyed by convolution. Using a 3 × 3 smoothing mask, namely Eq. (5.3), the MAC and ALE schemes yield good results, which are more accurate with a 9 × 9 smoothing mask.

Conversely, deconvolution of smoothed grey level can enhance the image edge (see Figure 5.1).

5.2 Accurate Evaluation of Surface Normal and Curvature

VOF function in the normal direction of a free surface is a step function, whose derivative is the Dirac delta function or impulse function with infinite height and infinitesimal spatial or temporal interval[81]. The direct accurate (DA) algorithm is derived and the gradient of VOF function in the normal direction is found a rectangular pulse function, which is an approximate to the impulse function.

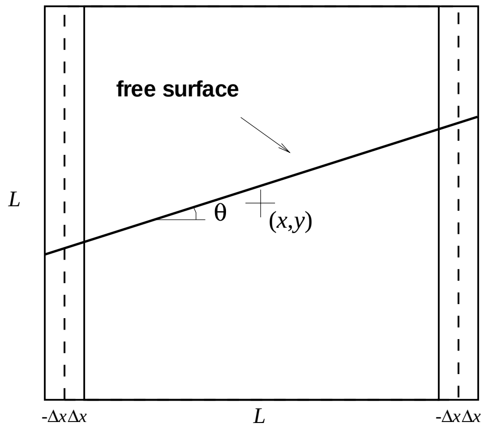

Figure 5.2 A free surface inclined in a control cell

In Figure 5.2, we model a free surface using Piecewise Liner Interface Construction (PLIC) method[7, 85]. Less strictly, a cell side is called ‘wet’ if it is intersected with a free surface. In an $L \times L$ squared control cell, for example, we suppose that the free surface is horizontally oriented, i.e., $-45° \leqslant \theta \leqslant 45°$ and both left and right sides are wet as shown in Figure 5.2. We have Taylor’s series expansion of VOF function about the center (x, y),

$$\frac{F(x+\Delta x, y) - F(x-\Delta x, y)}{2\Delta x} = \left(\frac{\partial F}{\partial x}\right)_{(x,y)} + \mathcal{O}(\Delta x^2), \tag{5.4}$$

where Δx is a small deviation in the x-direction off point (x, y). Meanwhile, it can be derived from the piecewise-approximation of free surface:

$$\frac{F(x+\Delta x, y) - F(x-\Delta x, y)}{2\Delta x} = \frac{\tan\theta}{L} = \frac{1}{L}\left[-\left(\frac{\partial F}{\partial x}\right) \Bigg/ \left(\frac{\partial F}{\partial y}\right)\right]_{(x,y)}, \tag{5.5}$$

since $F(x+\Delta x, y) - F(x-\Delta x, y) = (2\Delta x)L\tan\theta/L^2$.

Therefore, we have a new formula to evaluate gradients of VOF function at the center of a control cell for a horizontally-oriented free surface from Eqs. (5.4) and (5.5):

$$\begin{aligned} \left(\frac{\partial F}{\partial x}\right)_{(x,y)} &= \frac{F(x+\delta x/2, y) - F(x-\delta x/2, y)}{\delta x} \\ \left(\frac{\partial F}{\partial y}\right)_{(x,y)} &= -\frac{1}{N\delta y}, \end{aligned} \tag{5.6}$$

where $\delta x = 2\Delta x$ is the mesh size of the x-direction and N is the number of δy for one control cell size, namely $L = N\delta y$. It demonstrates that Eq. (5.6) is a different fashion from those MAC and ALE-like schemes; for instance, if the free surface is horizontally-oriented and $L = \delta y$, the gradient of F in the y-direction is equal to $-1/\delta y$.

From Eq. (5.6), the formulation for surface normal computed using $N = 1$ and VOF function, namely $\tilde{c} = c = \tilde{F} = F$, is derived as follows if the grid is not uniform:

$$\begin{aligned} \left(\frac{\partial F}{\partial x}\right)_{i+1/2,j} &= \frac{F_{i+1,j} - F_{i,j}}{\frac{1}{2}(\delta x_i + \delta x_{i+1})} \\ \left(\frac{\partial F}{\partial y}\right)_{i+1/2,j} &= \left(\frac{\partial F}{\partial y}\right)_{i-1/2,j} = \pm\frac{1}{\delta y_j} \end{aligned} \tag{5.7}$$

and

$$\begin{aligned} \left(\frac{\partial F}{\partial x}\right)_{i,j+1/2} &= \left(\frac{\partial F}{\partial x}\right)_{i,j-1/2} = \frac{1}{2}\left[\left(\frac{\partial F}{\partial x}\right)_{i+1/2,j} + \left(\frac{\partial F}{\partial x}\right)_{i-1/2,j}\right] \\ \left(\frac{\partial F}{\partial y}\right)_{i,j+1/2} &= \left(\frac{\partial F}{\partial y}\right)_{i,j-1/2} = \pm\frac{1}{\delta y_j} \end{aligned} \tag{5.8}$$

for horizontally-oriented free surface as shown in Figure 5.3. Likewise, we have a formulation for vertically-oriented free surface (not shown in the figure). The negative signs in Eqs. (5.7) to (5.8) are chosen when **fluid 2** is lower than **fluid 1**; otherwise, they can be replaced by the positive signs.

All the formulations above are valid only when the corresponding sides of a cell are wet; for example, the horizontally-oriented free surface as noted in Figure 5.3. The wetting condition can be met by averaging color or VOF function (see Section 5.1).

The orientation of free surface at one control cell is roughly predetermined by the ALE algorithm or by the VOF functions distributed surrounding the control cell center.

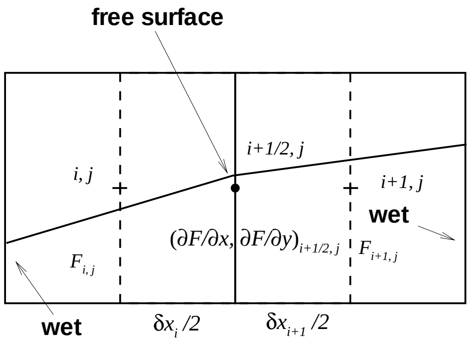

Figure 5.3 Side wetting and horizontally inclined free surface

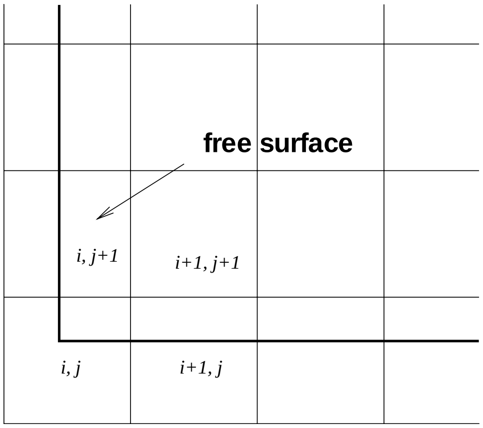

Figure 5.4 Illustration of a corner-shaped configuration of free surface

Under some certain circumstances when a free surface is not continuous as shown in Figure 5.4, a specific angle is simply imposed at the corner cell. In reality, these right-angle free surfaces will evolve physically to be continuous under surface tension.

From Eq. (5.6), we can find the relationship between the gradients of F and $\tilde{F}$ functions,

$$\frac{\partial F}{\partial x} = N\left(\frac{\partial \tilde{F}}{\partial x}\right)_{N\times N} \qquad \text{and} \qquad \frac{\partial F}{\partial y} = N\left(\frac{\partial \tilde{F}}{\partial y}\right)_{N\times N}, \tag{5.9}$$

which means the accuracy of surface normal cannot be improved by the averaging mask of Eq. (5.3).

The gradient values in ∇F at each cell center can be computed by averaging four components at the midpoints of four faces (refer to Figure 5.3). Then from Eqs. (3.12) and (3.11), we can have unit normals at the grid center and the midpoint of each grid face. The unit normal at the cell center can either be computed by averaging those at the face midpoints, for example, at the grid cell (i, j),

$$\hat{n}_{i,j} = \frac{1}{4}\left(\hat{n}_{i+1/2,j} + \hat{n}_{i-1/2,j} + \hat{n}_{i,j+1/2} + \hat{n}_{i,j-1/2}\right). \tag{5.10}$$

The discrete form of Eq. (3.10) is presented for computing surface curvature as follows:

$$\kappa_{i,j} = -\left(\frac{\hat{n}_{xi+1/2,j} - \hat{n}_{xi-1/2,j}}{\delta x_i} + \frac{\hat{n}_{yi,j+1/2} - \hat{n}_{yi,j-1/2}}{\delta y_j}\right). \tag{5.11}$$

Notice surface curvature is not evaluated directly from ∇F.

5.3 Estimation of Density and Reformulation of Tension Force

In the reconstructed CSF model, the surface tension force is restricted within a narrow region of $\mathcal{O}(h)$ as shown in Figure 5.5, because the effect of surface tension force diminishes to zero inside fluids in physics.

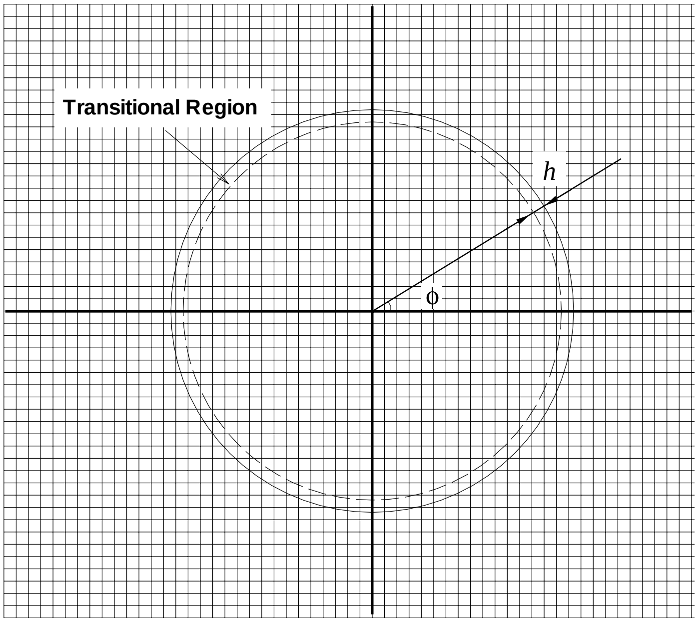

Figure 5.5 A circular droplet with a transitional region of thickness h

Apparently, an empty grid cell has zero VOF function, whereas an interfacial cell can be defined as having non-zero VOF function and at least one empty neighboring grid cell. Then we have three types of interfacial cell with $0 < F \leqslant 1.0$ as shown in

Figure 5.6:

$$F(\vec{x},t) = \begin{cases} > 0.5 \text{ and } \leqslant 1.0 & \text{with the center immersed in free surface;} \\ 0.5 & \text{with the center on free surface;} \\ > 0 \text{ and } < 0.5 & \text{with the center outside free surface.} \end{cases} \tag{5.12}$$

If $F = 0.5$, the grid cell center always lies on the free surface no matter what the tilting angle of free surface is, simply because the cell is rectangular and the free surface within the cell is constructed by PLIC. The center is outside **fluid 2** when $F < 0.5$ and it is immersed in **fluid 2** if $F > 0.5$.

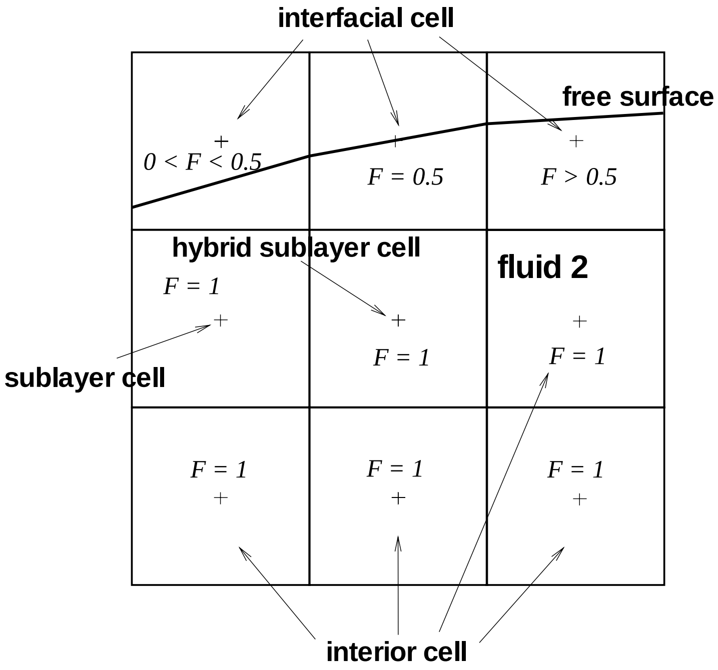

Figure 5.6 Categories of empty, interfacial, sublayer, and interior cells

Inside **fluid 2**, an interior grid cell is strictly defined as having unity VOF function and distance from the center to free surface greater than one grid size h. Between an interfacial grid cell and an interior grid cell, there may be a sublayer grid cell also having unity VOF function but distance to free surface less than h in Figure 5.6. Nevertheless, a sublayer cell becomes an interfacial cell if it has an empty neighboring cell (not shown). This is why an interfacial cell may have unity VOF function.

Hence, we have the categories of empty cell ($F = 0$), interfacial cell ($0 < F \leqslant 1.0$), sublayer cell ($F = 1.0$), and interior cell ($F = 1.0$) as illustrated in Figures 5.5 and 5.6.

Likewise, in order to estimate surface tension at control cell centers, we need to classify *control cells* into three types: interfacial, sublayer, and interior control cells, as shown in Figure 5.8. An interfacial control cell of one direction has distance from the control cell center to free surface less than $h/2$ in the direction, whereas an interior control cell has distance to free surface greater than $3h/2$. A sublayer control cell has distance to free surface between $h/2$ and $3h/2$.

In Eq. (3.2), the density at the center of a control cell $(i + 1/2, j)$, for example, is estimated by interpolating the densities of two adjacent grid cells given in [16]. As a matter of fact, RIPPLE[16] failed in the simulation of a stationary inclined plane perpendicular to gravity (see Figures 6.24 through 6.26). The static pressures inside the inclined planar surface are erroneous. The linear interpolation of density in an interfacial cell is neither physical nor accurate. Thus it is believed to be a source of spurious currents.

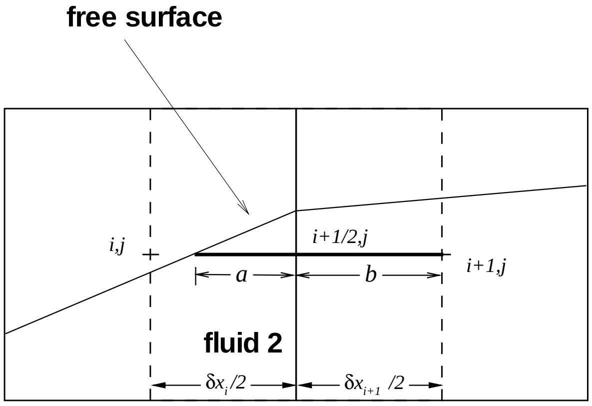

Figure 5.7 Estimation of density between two interfacial cells

In this work, a new way to compute the density on interfacial control cells is proposed as follows; for example, in the x-direction for a control cell $(i + 1/2, j)$ as bounded in the dashed lines in Figure 5.7:

$$\rho_{i+1/2,j} = \frac{a+b}{\frac{1}{2}(\delta x_i + \delta x_{i+1})}\rho_f, \tag{5.13}$$

where $a+b$ is the *immersed* portion between two grid centers also shown in the figure. If both centers (i,j) and $(i+1,j)$ are immersed, namely $a+b = (\delta x_i + \delta x_{i+1})/2$, Eq. (5.13) reduces to $\rho_{i+1/2,j} = \rho_f$. The immersed length is computed in the light of the surface normal vector and F function.

Consistent with the concept of immersed length, the volumetric tension force at the interfacial control cell $(i+1/2,j)$, for example, is

$$F_{\mathrm{sv}xi+1/2,j} = \frac{\sigma\kappa_{i,j}\left(\dfrac{\partial F}{\partial x}\right)_{i,j} a + \sigma\kappa_{i+1,j}\left(\dfrac{\partial F}{\partial x}\right)_{i+1,j} b}{\frac{1}{2}(\delta x_i + \delta x_{i+1})}, \tag{5.14}$$

where $a+b$ is the same as that in Eq. (5.13) shown in Figure 5.7.

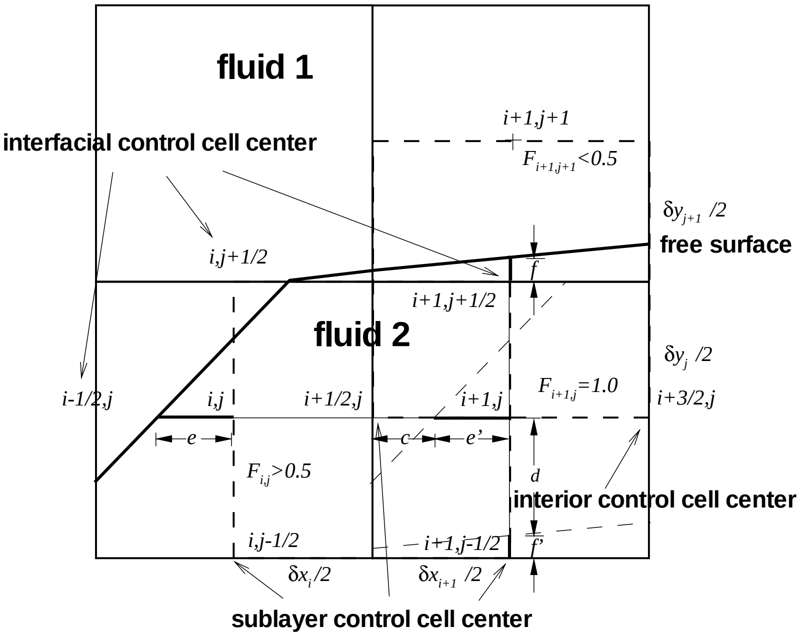

Figure 5.8 Estimation of surface tension force in the x- and y-directions

At an interior control cell center, the surface tension effect vanishes. For example, at $(i+3/2, j)$ in Figure 5.7:

$$F_{\mathrm{sv}xi+3/2,j} = 0 \tag{5.15}$$

for the x-component volumetric surface tension estimation.

For control cell $(i+1/2, j)$ and $(i+1, j-1/2)$ in Figure 5.7, which are two sublayer control cell centers, we have, respectively, with some modifications to Eq. (5.14):

$$F_{\mathrm{sv}xi+1/2,j} = \frac{\sigma\kappa_{i,j}\left(\dfrac{\partial F}{\partial x}\right)_{i,j}\dfrac{\delta x_i}{2} + \sigma\kappa_{i+1,j}\left(\dfrac{\partial F}{\partial x}\right)_{i+1,j} c}{\dfrac{1}{2}\left(\delta x_i + \delta x_{i+1}\right)} \tag{5.16}$$

and

$$F_{\mathrm{sv}yi+1,j-1/2} = \frac{\sigma\kappa_{i+1,j}\left(\dfrac{\partial F}{\partial y}\right)_{i+1,j} d}{\dfrac{1}{2}\left(\delta y_j + \delta y_{j+1}\right)}. \tag{5.17}$$

The weight parameters c and d in Eq. (5.17) are computed as

$$c = \frac{\delta x_{i+1}}{2} - a\frac{\delta x_{i+1}}{\delta x_i}, \qquad d = \frac{\delta y_j}{2} - b\frac{\delta y_j}{\delta y_{j+1}}, \tag{5.18}$$

where $0 \leqslant a \leqslant \delta x_i/2$ and $0 \leqslant b \leqslant \delta y_{j+1}/2$, respectively, as shown in Figure 5.8. Notice in Figure 5.8, the dashed lines are plotted parallel to the free surface one h away in the two directions inside **fluid 2**.

Eq. (5.16) is also applicable to the sublayer control cell $(i, j-1/2)$, though in the y-component form. Because the control cell center $(i+1, j-1/2)$ has a distance greater than h to free surface in the y-direction, the contribution by grid cell $(i+1, j-1)$ to the volumetric surface tension at $(i+1, j-1/2)$ vanishes in Eq. (5.17).

h is the sole length scale of the transitional region, a uniform grid with equal spacings is accordingly preferred to generate for surface tension estimation. Hence we have $\delta x_i = \delta y_j = h$, $e' = e$, and $f' = f$ in Eq. (5.18).

On the free surface where $F < 1$, the concept of immersed length is also applied in the computation of the velocity gradients; for example, if the horizontal centerline of a grid is not immersed $\partial u/\partial x = 0$ in the computation of the viscous dissipation term. However, the immersed length is not used as a weight parameter in the viscous force because it appears in both viscous tensor and density estimations.

For a surface flow, if the surface tension is stronger than the viscous effect in the normal direction and the surface tension coefficient is constant, Eq. (2.25) can be implemented in the calculation of viscous force on free surface. As shown in Figure 5.9, the viscous contribution in $\tilde{u}_{i+1/2,j}$ vanishes in Eq. (3.28) because of Eq. (2.25), whereas the viscous force is estimated for $\tilde{u}_{i+3/2,j}$. Obviously, the viscous effect is not considered in the computation of $\tilde{u}_{i-1/2,j}$ because **fluid 1** has negligible viscosity. Likewise, the vertical dump velocity on free surface is estimated in the same way that the viscous friction effect is neglected on free surface, namely Eq. (2.25).

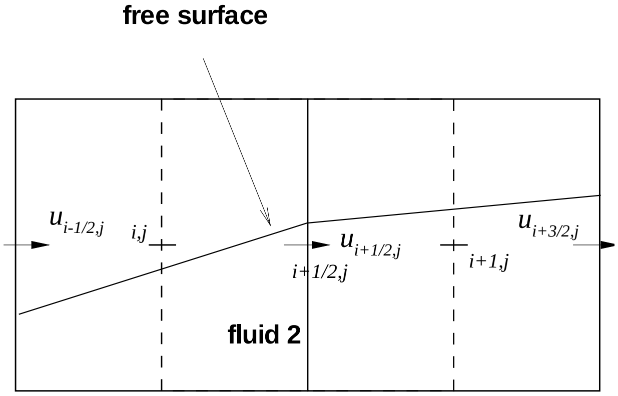

Figure 5.9 Illustration of viscous force estimation on free surface

5.4 Enforcement of Pressure in Interfacial Cells

In the modified approach for pressure solution, we impose the ambient pressure as the boundary conditions on grid cells where $F = 0.5$ such that

$$p = p_1, \tag{5.19}$$

as shown in Figure 5.10(a). If the center of a grid cell is not immersed, namely $F < 0.5$, Eq. (5.19) is also applicable, obviously.

Only on those cells having $F > 0.5$ as shown in Figure 5.10(a), the pressure is sought in solving the PPE, i.e., Eq. (3.31), simply because the pressure varies with flow and surface tension. Notice in Figure 5.10, p_2 is unknown, and p_1 is a given ambient pressure. From Figure 5.10(a), the modified boundary condition for the PPE compresses the interfacial region of two fluids, compared with the approach in RIPPLE in Figure 5.10(b).

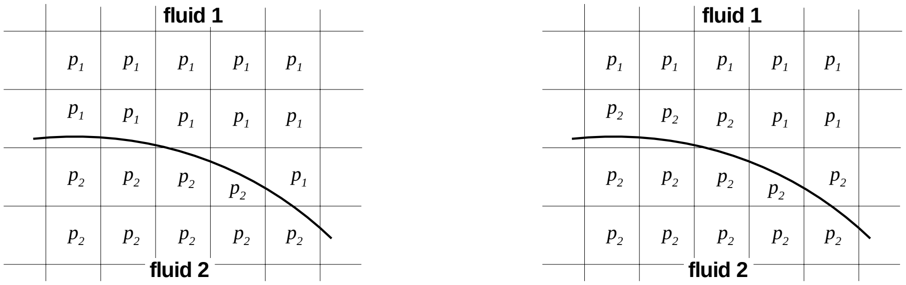

(a) Modified dynamic boundary condition

(b) Dynamic boundary condition in RIPPLE

Figure 5.10 Pressure enforced on interfacial cells

The criterion of 0.5 VOF value for an immersed grid center is still valid in 3D as long as rectangular parallelepiped grid cells are generated and free surface is piecewise reconstructed by planes. More computation is required to determine whether a grid cell immersed or not, depending on local curvature if the free surface is reconstructed by quadratic or spline approximation in both 2D and 3D computations. Apparently, the criteria are then no longer a constant. They may be less than 0.5 for a concave free surface and greater than 0.5 for a convex free surface.

Nevertheless, there is an issue of velocity on the face between two interfacial grid cells both having less than 0.5 F functions as shown in Figure 5.11. According to the modified approach in this section, at these two grid cell centers the pressures are both p_1 (see cells (i, j) and $(i+1, j)$ in Figure 5.11). Then the velocity at the center of control cell $(i+1/2, j)$ is computed to be zero because the pressures are equal, so **fluid 1** is motionless. However, we notice that velocities in both normal and tangential directions continuously change across the free surface unlike pressure and density. **Fluid 1** accelerates so quickly and moves at the same velocity with **fluid 2** because the density and viscosity of **fluid 1** are both negligibly small. Thus, we simply give

$$u_{i+1/2,j} = u_{i+1/2,j-1} \tag{5.20}$$

where $u_{i+1/2,j}$ is the velocity between two grid cells both with VOF function less than 0.5 next to **fluid 2**, and the vertical velocity at the control center $(i, j+1/2)$ also as

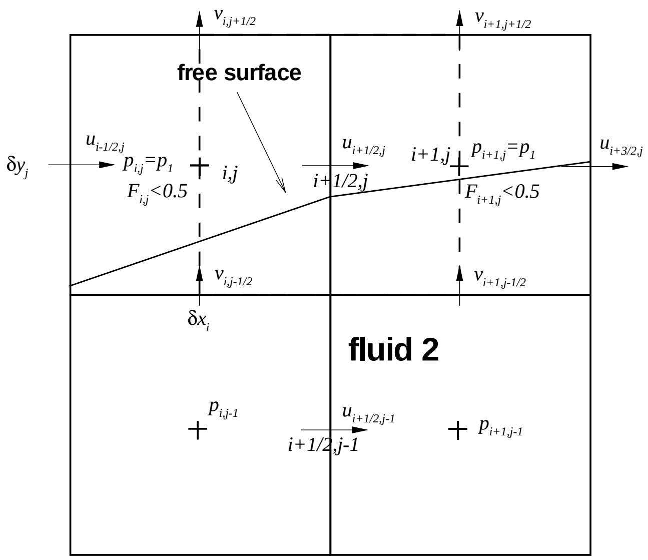

Figure 5.11 Velocity rectification outside free surface

shown in Figure 5.11,

$$v_{i,j+1/2} = v_{i,j-1/2} + \frac{\delta y_j}{\delta x_i}\left(-u_{i,j+1/2} + u_{i,j-1/2}\right), \tag{5.21}$$

to ensure mass conservation. Likewise, $v_{i+1,j+1/2}$ can be computed in the same way as Eq. (5.21).

A paradox that a non-zero velocity exists between the points both having p_1 arises in the modified approach because **fluid 1** is oversimplified to be a vacuum with pressure p_1. Eqs. (5.20) and (5.21), however, rectify the simplification of **fluid 1**.

5.5 Translation Terms in Equations

A molten alloy is injected from the nozzle to the rotating wheel, as shown in Figure 1.1. In the simulation of melt spinning, there are two coordinate systems, which are fixed to the nozzle and the spinning wheel, respectively (see Figure 5.12).

Although the grids generated in these two systems coincide with each other at every time level, they have a relative motion of velocity U_{w}, the wheel linear speed. Thus, we

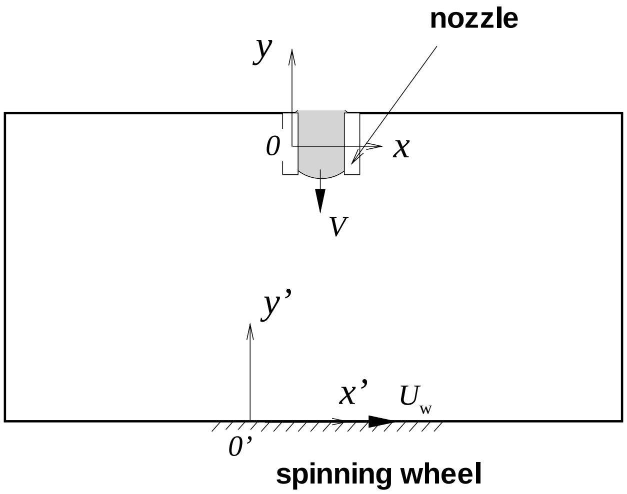

The two coordinate systems have a relative velocity of U_w.

Figure 5.12 Two coordinate systems in melt spinning

have velocity relation

$$\vec{V}_{\mathrm{j/n}} = \vec{V}_{\mathrm{j/w}} + \vec{V}_{\mathrm{w/n}} \quad \text{and} \quad \vec{V}_{\mathrm{w/n}} = U_{\mathrm{w}}\hat{\imath}, \tag{5.22}$$

where the subscript j represents the jet flow and n represents the nozzle. Henceforward, we ignore the subscript j/n for simplicity. Substitution of $\vec{V}_{\mathrm{j/w}}$ with $\vec{V}_{\mathrm{j/n}}$ in the governing equations, Eqs. (3.1), (3.2), and (4.2), respectively, gives

$$\nabla \cdot \vec{V} = 0, \tag{5.23}$$

$$\frac{\partial \vec{V}}{\partial t} + \nabla \cdot \left(\vec{V}\vec{V}\right) = \left(\vec{V}_{\mathrm{w/n}} \cdot \nabla\right)\vec{V} - \frac{1}{\rho}\nabla p + \frac{1}{\rho}\nabla \cdot \tau + \vec{g} + \frac{1}{\rho}\vec{F}_{\mathrm{b}}, \tag{5.24}$$

$$\frac{\partial T}{\partial t} + \nabla \cdot (\vec{V}T) = \left(\vec{V}_{\mathrm{w/n}} \cdot \nabla\right) T + \left(\frac{2\nu}{C_p}\right) \mathbf{S} : \nabla\vec{V} + \alpha\nabla^2 T. \tag{5.25}$$

Eq. (5.23) remains unchanged because $\vec{V}_{\mathrm{w/n}}$ is a constant vector. Eq. (5.24) has an extra term on the RHS regarding the translation (convection) momentum that the spinning wheel exerts on the molten jet, and so does Eq. (5.25). These extra terms necessarily appear in the equations after the jet impinges on the wheel. In updating velocity, the extra convection term is added in Eq. (3.29) so that

$$\vec{V}^{\mathrm{n}+1} = \tilde{\vec{V}} - \frac{\delta t}{\rho}\nabla p^{\mathrm{n}+1} + \delta t(\vec{V}_{\mathrm{w/n}} \cdot \nabla)\vec{V}^{\mathrm{n}}. \tag{5.26}$$

A complete upwind finite difference scheme is adopted to calculate the gradient of velocity in Eq. (5.26). The upwind scheme is also used in updating temperature due to the thermal convection by the moving wheel:

$$T^{\mathrm{n}+1} = \tilde{T} + \delta t \left(\vec{V}_{\mathrm{w/n}} \cdot \nabla\right) T^{\mathrm{n}}, \tag{5.27}$$

where $\tilde{T}$ is contributed by thermal convection, viscous dissipation, and diffusion terms. Notice in Eqs. (5.26) and (5.27) δt is chosen from Eqs. (3.34) to (3.37).

5.6 Normalization of Formulation

In many engineering problems such as a melt spinning, physical domains often have large aspect ratios and the velocity in one direction is often larger than that in the other by one or more orders of magnitude. If the governing equations are transformed into nondimensional forms based on some deliberately selected reference quantities, it may not only permit the flow variables to be properly scaled in computation but also yield a group of important dimensionless parameters revealing general underlying similarities. On the transformed computational domain, the grid can be generated with a desirable aspect ratio, and a suitable time increment can be selected.

The advection of VOF function is invariant in the scaling because F is already normalized:

$$\frac{\partial F}{\partial t^*} + \left(\vec{V}^* \cdot \nabla\right) F = 0, \tag{5.28}$$

where t^* is dimensionless time defined in Eq. (5.29).

By selecting proper quantities for reference lengths L_x and L_y, velocities U and V, the ambient pressure p_{a}, and the fluid density ρ_f, we have 2D dimensionless variables as follows in asterisks:

$$\begin{aligned}
x^* &= \frac{x}{L_x}, \qquad y^* = \frac{y}{L_y}, \\
u^* &= \frac{u}{U}, \qquad v^* = \frac{v}{V}, \qquad t^* = \frac{t}{L_x/U}, \\
p^* &= \frac{p - p_{\mathrm{a}}}{\rho_f U^2}, \qquad \rho^* = \frac{\rho}{\rho_f}, \\
F^*_{\mathrm{b}x} &= \frac{F_{\mathrm{b}x}}{\rho_f U^2/L_x}, \qquad F^*_{\mathrm{b}y} = \frac{F_{\mathrm{b}y}}{\rho_f V^2/L_y} \\
g^*_x &= \frac{g_x}{U^2/L_x}, \qquad g^*_y = \frac{g_y}{V^2/L_y},
\end{aligned} \tag{5.29}$$

where the dimensionless density $\rho^* = 1$ on any interior cells and consistent with the definition of VOF function in Eq. (3.20). Eqs. (5.23) to (5.25) are normalized by introducing the above dimensionless variables in 2D forms as follows:

$$\frac{\partial u^*}{\partial x^*} + \frac{\partial v^*}{\partial y^*} = 0, \tag{5.30}$$

$$\begin{aligned}
\frac{\partial u^*}{\partial t^*} + u^* \frac{\partial u^*}{\partial x^*} + v^* \frac{\partial u^*}{\partial y^*} =& U^*_{\mathrm{w}} \frac{\partial u^*}{\partial x^*} - \frac{1}{\rho^*} \frac{\partial p^*}{\partial x^*} + \\
& \frac{1}{\mathbf{Re}} \left[\frac{\partial^2 u^*}{\partial x^{*2}} + \left(\frac{L_x}{L_y} \right)^2 \frac{\partial^2 u^*}{\partial y^{*2}} \right] + \frac{1}{\rho^*} F^*_{\mathrm{b}x} + g^*_x,
\end{aligned} \tag{5.31}$$

$$\begin{aligned}
\frac{\partial v^*}{\partial t^*} + u^* \frac{\partial v^*}{\partial x^*} + v^* \frac{\partial v^*}{\partial y^*} =& U^*_{\mathrm{w}} \frac{\partial v^*}{\partial x^*} - \left(\frac{L_x}{L_y} \right)^2 \left(\frac{1}{\rho^*} \frac{\partial p^*}{\partial y^*} \right) + \\
& \frac{1}{\mathbf{Re}} \left[\frac{\partial^2 v^*}{\partial x^{*2}} + \left(\frac{L_x}{L_y} \right)^2 \frac{\partial^2 v^*}{\partial y^{*2}} \right] + \frac{1}{\rho^*} F^*_{\mathrm{b}y} + g^*_y,
\end{aligned} \tag{5.32}$$

where $\vec{V}^* = u^* \hat{\imath} + v^* \hat{\jmath}$ and the inverse of the dimensionless kinematic viscosity ν^* is *Reynolds number* **Re**, namely

$$\frac{1}{\nu^*} = \mathbf{Re} \equiv \frac{L_x U}{\nu}. \tag{5.33}$$

If the characteristic velocity U is chosen as the wheel speed U_{w}, $U^*_{\mathrm{w}} = 1$ in Eqs. (5.31) and (5.32).

The continuity equation remains unchanged (compare Eq. (3.1) with (5.30)) because the relation as follows is applied:

$$\frac{U}{L_x} = \frac{V}{L_y}. \tag{5.34}$$

The advection terms in Eqs. (5.31) and (5.32) remain the same as their dimensional counterparts in Eq. (3.2). The viscous stress tensor matrix in Eq. (3.7) becomes

$$[\tau] = \frac{U\mu}{L_x} \begin{bmatrix} 2\dfrac{\partial u^*}{\partial x^*} & \left(\dfrac{L_x}{L_y}\right)\dfrac{\partial u^*}{\partial y^*} + \left(\dfrac{L_y}{L_x}\right)\dfrac{\partial v^*}{\partial x^*} \\ \left(\dfrac{L_y}{L_x}\right)\dfrac{\partial v^*}{\partial x^*} + \left(\dfrac{L_x}{L_y}\right)\dfrac{\partial u^*}{\partial y^*} & 2\dfrac{\partial v^*}{\partial y^*} \end{bmatrix} \tag{5.35}$$

from which the viscous terms in Eqs. (5.31) and (5.32) are derived. From Eq. (3.8), we have dimensionless volumetric surface tension forces in the x- and y-directions, respectively,

$$F^*_{\mathrm{b}x} = F^*_{\mathrm{sv}x} = \sigma^* \kappa^* \frac{\partial F}{\partial x^*} g(\vec{x}) \tag{5.36}$$

and

$$F^*_{\mathrm{b}y} = F^*_{\mathrm{sv}y} = \sigma^* \kappa^* \left(\frac{L_x}{L_y}\right)^2 \frac{\partial F}{\partial y^*} g(\vec{x}) \tag{5.37}$$

where σ^* is a dimensionless surface tension coefficient:

$$\sigma^* = \frac{\sigma}{\rho_f U^2 L_x} \tag{5.38}$$

and the inverse is *Weber number*,

$$\frac{1}{\sigma^*} = \mathbf{Web} \equiv \frac{\rho_f U^2 L_x}{\sigma}. \tag{5.39}$$

From Eqs. (5.33), (5.39), and (3.39), we have

$$\mathbf{Ca} = \frac{\mathbf{Web}}{\mathbf{Re}}. \tag{5.40}$$

We define dimensionless surface normal vector as follows:

$$\vec{n}^* = \frac{\partial F}{\partial x^*}\hat{\imath} + \left(\frac{L_x}{L_y}\right)\frac{\partial F}{\partial y^*}\hat{\jmath}, \tag{5.41}$$

such that

$$\vec{n}^* = \vec{n} L_x \qquad \text{and} \qquad \hat{n}^* = \hat{n}. \tag{5.42}$$

The dimensionless curvature in Eqs. (5.36) and (5.37) is then given as follows:

$$\kappa^* = \kappa L_x \qquad \text{and} \qquad \kappa^* = -\left[\frac{\partial \hat{n}^*_x}{\partial x^*} + \left(\frac{L_x}{L_y}\right)\frac{\partial \hat{n}^*_y}{\partial y^*}\right]. \tag{5.43}$$

$g(\vec{x})$ in Eqs. (5.36) and (5.37) is equal to either 1 or $2F$ which is normalized.

The normalized PPE is derived from Eq. (3.31):

$$\left[\frac{\partial}{\partial x^*}\left(\frac{1}{\rho^{*\mathrm{n}}}\frac{\partial p^{*\mathrm{n}+1}}{\partial x^*}\right)+\left(\frac{L_x}{L_y}\right)^2\frac{\partial}{\partial y^*}\left(\frac{1}{\rho^{*\mathrm{n}}}\frac{\partial p^{*\mathrm{n}+1}}{\partial y^*}\right)\right]=\frac{\nabla\cdot\vec{\tilde{V}}^*}{\delta t^*} \tag{5.44}$$

where the dimensionless tilde velocity $\vec{\tilde{V}}^* = \tilde{u}^*\hat{\imath}+\tilde{v}^*\hat{\jmath}$ is normalized by two characteristic velocities U and V, respectively:

$$\tilde{u}^*=\frac{\tilde{u}}{U},\qquad \tilde{v}^*=\frac{\tilde{v}}{V}. \tag{5.45}$$

Substitution of the dimensionless variables gives the normalized Eq. (3.29) in scalar forms:

$$\frac{u^{*\mathrm{n}+1}-\tilde{u}^*}{\delta t^*}=U^*_{\mathrm{w}}\frac{\partial u^{*\mathrm{n}}}{\partial x^*}-\frac{1}{\rho^{*\mathrm{n}}}\frac{\partial p^{*\mathrm{n}+1}}{\partial x^*} \tag{5.46}$$

and

$$\frac{v^{*\mathrm{n}+1}-\tilde{v}^*}{\delta t^*}=U^*_{\mathrm{w}}\frac{\partial v^{*\mathrm{n}}}{\partial x^*}-\frac{1}{\rho^{*\mathrm{n}}}\left(\frac{L_x}{L_y}\right)^2\frac{\partial p^{*\mathrm{n}+1}}{\partial y^*}. \tag{5.47}$$

According to the transformations in Eq. (5.29), the normalized boundary conditions can be simply expressed as follows:

$$\vec{V}^*=0 \quad \text{or} \quad \vec{V}^*=\vec{V}^*_{\mathrm{wall}} \tag{5.48}$$

for no-slip boundary conditions, and

$$\hat{n}^*_{\mathrm{wall}}\cdot\vec{V}^*=0 \tag{5.49}$$

for slip-free (no penetration) boundary conditions at any solid wall, where $\hat{n}^*_{\mathrm{wall}}$ is the unit normal to the wall in the transformed system $(\vec{x}^*, t^*)$. The normalized pressure jump across the interface between liquid and gas is

$$p^*_s=p^*-p^*_v=\sigma^*\kappa^*. \tag{5.50}$$

In the normalization of initial conditions, according to the transformation Eq. (5.29), velocity, pressure, and VOF function can be specified as follows:

$$\begin{aligned}\vec{V}^*(\vec{x}^*,0)&=\vec{V}^*_0\\ p^*(\vec{x}^*,0)&=p^*_0\\ F(\vec{x}^*,0)&=F_0\end{aligned} \tag{5.51}$$

where F is not asterisked because it is a normalized variable.

Scaling is also applied to the thermal-energy Eq. (4.2). In a 2D Cartesian system, we have:

$$\begin{aligned}\frac{\partial T^*}{\partial t^*}+\frac{\partial(u^*T^*)}{\partial x^*}+\frac{\partial(v^*T^*)}{\partial y^*} =& U_{\mathrm{w}}^*\frac{\partial T^*}{\partial x^*}+2\frac{\mathbf{Ec}}{\mathbf{Re}}\left(\mathbf{S}^*:\nabla^*\vec{V}^*\right)+\\ &\frac{1}{\mathbf{Pe}}\left[\frac{\partial^2 T^*}{\partial x^{*2}}+\left(\frac{L_x}{L_y}\right)^2\frac{\partial^2 T^*}{\partial y^{*2}}\right],\end{aligned} \tag{5.52}$$

where **Ec** is called *Eckert number*, defined as:

$$\mathbf{Ec}\equiv\frac{U^2}{C_p(T_\infty-T_{\mathrm{w}})} \tag{5.53}$$

and the viscous dissipation term is

$$\mathbf{S}^*:\nabla^*\vec{V}^*=\left(\frac{\partial u^*}{\partial x^*}\right)^2+\frac{1}{2}\left[\left(\frac{L_x}{L_y}\right)\frac{\partial u^*}{\partial y^*}+\left(\frac{L_y}{L_x}\right)\frac{\partial v^*}{\partial x^*}\right]^2+\left(\frac{\partial v^*}{\partial y^*}\right)^2, \tag{5.54}$$

with the transformations in Eq. (5.29) and dimensionless temperature

$$T^*=\frac{T-T_{\mathrm{w}}}{T_\infty-T_{\mathrm{w}}}. \tag{5.55}$$

A dimensionless parameter analogous to Reynolds number *Peclet number* appears on the RHS of Eq. (5.52):

$$\mathbf{Pe}\equiv\frac{UL_x}{\alpha}. \tag{5.56}$$

We know Prandtl number is the ratio of Peclet number to Reynolds number,

$$\mathbf{Pr}=\frac{\mathbf{Pe}}{\mathbf{Re}}. \tag{5.57}$$

The normalized initial conditions for temperature are modified to be

$$T^*(\vec{x}^*,0)=T_0^*. \tag{5.58}$$

Finally, the normalized temperature boundary conditions on free surface are

$$\frac{\partial T^*}{\partial x^*}=\frac{L_x}{k}[hT^*+\epsilon\sigma_{\mathrm{SB}}T^*(T+T_{\mathrm{a}})(T^2+T_{\mathrm{a}}^2)]\hat{n}_x^*, \tag{5.59}$$

in the x-direction and

$$\frac{\partial T^*}{\partial y^*}=\frac{L_y}{k}[hT^*+\epsilon\sigma_{\mathrm{SB}}T^*(T+T_{\mathrm{a}})(T^2+T_{\mathrm{a}}^2)]\hat{n}_y^* \tag{5.60}$$

in the y-direction, respectively, where $(T+T_{\mathrm{a}})(T^2+T_{\mathrm{a}}^2)$ is computed based on the temperature at the previous time level.

CHAPTER 6 NUMERICAL VERIFICATION

The broken dam problem in Section 6.1 is chosen to test the computer program in the comprehensive sense of quantitative accuracy; whereas the numerical results of undular bore in Section 6.2 show the gravitational force simulation. The sluice gate problem in Section 6.3 is a trial to the scalings of the equation system, which is discussed in Section 5.6 of Chapter 5. Section 6.4 discusses accurate calculations of surface normal and curvature for two examples using the DA algorithm. Sections 6.4 and 6.5 show that capillary currents occur if the surface curvatures are not equal along free surface. The spurious currents have been thoroughly eliminated by the efforts made in the work.

For the test problems, the experimental data are quoted and the analytical solutions have been derived to compare with the numerical simulations. Also, sensitivity assessment of grid resolution helps us seek solutions independent of grid resolution in each test problem. Using Tecplot I have created some animation to imitate these hydrodynamic and capillary phenomena.

6.1 Broken Dam Problem

2D broken dam flow is an approximation to the motion of a rectangular column of water onto a dry rigid horizontal ground after a sudden destruction of the confining wall, as show in Figure 6.1. It is not only of practical interest but also a good example of validation with relatively simple boundary and initial conditions.

Martin and Moyce[86] have performed an experimental study, examining 2D collapses of rectangular and semicircular sections, and an axially symmetrical collapse of vertical circular cylinders. After a sudden heavy electrical current melted the container of waxed paper diaphragm, motions of the water surge front and residual height of the water column were recorded by a high-speed camera at a series of selected time intervals.

Table 6.1 lists the tests, the asterisked of which have been simulated in the work (see Table 6.2). γ in the tables is defined as aspect ratio of the initial water height h versus the initial base of water column a, namely $\gamma = h/a$, as noted in Figure 6.1.

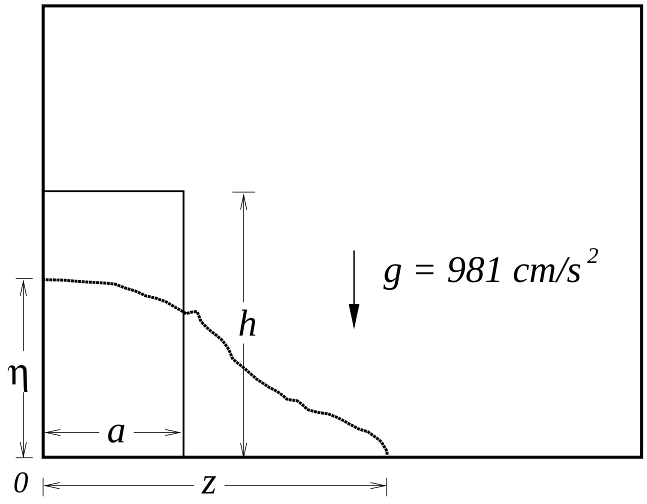

Figure 6.1 Water columns before and after a sudden collapse of the dam

Stoker[87] has sought analytical solutions for both wet and dry downstream grounds. However, the water column has an infinity extension in the other horizontal direction. Hirt and Nichols[10] made some comparisons of their numerical simulations with Martin's experimental data[86] to validate the VOF method and the H-N algorithm.

Conventionally, for a hydrodynamic problem like the broken dam problem, the characteristic flow velocity is usually defined as

$$u = \sqrt{gh}, \tag{6.1}$$

where the downward gravity $g = 981\ cm/s^2$ is the only body force acting on the water column. In Table 6.2, Reynolds number and *Galileo number* are computed, respectively, as

$$\mathbf{Re} = \frac{ua}{\nu} \qquad \text{and} \qquad \mathbf{Ga} = \frac{a^3 g}{\nu^2}, \tag{6.2}$$

where u is the characteristic velocity of flow as given in Eq. (6.1). $\mathbf{Ga}$ is ratio of body force to viscous force of fluid; $\mathbf{Re}$ has a relation with $\mathbf{Ga}$, namely $\mathbf{Re} = \sqrt{\gamma \mathbf{Ga}}$ from Eqs. (6.2) and (6.1). The capillary number calculated based on the velocity of Eq. (6.1) is $0.01 \sim 0.014$.

Lateral Profile	Aspect Ratio γ	Base a (*inch*)
rectangular	1 : 1	$2\frac{1}{4}^*$, $4\frac{1}{2}$
	2 : 1	$1\frac{1}{8}^*$, $2\frac{1}{4}^*$
	4 : 1	$1\frac{1}{8}$
semicircular	1 : 1	2
vertical circular	1 : 1	$2\frac{1}{4}$
cylinder	2 : 1	$2\frac{1}{4}$

Table 6.1 Experiments for the broken dam problem

The following dimensionless quantities of length describe the water column:

$$Z \equiv \frac{z}{a} \qquad \text{and} \qquad H \equiv \frac{\eta}{h} \tag{6.3}$$

where z is the front position and η is the residual height of fluid column (see Figure 6.1).

We often use $\sqrt{L/g}$ as the characteristic time scale for a typical hydrodynamic problem, where L is a characteristic length. In the computations of front motion and discharge rate of the fluid column, we choose $L = h$ or a, which is consistent with our common sense that the higher the water column is, the faster the water front moves; the

Aspect Ratio γ	Base a (*in.*)	ν (cm^2/s)	**Re**	**Ga**
1 : 1	$2\frac{1}{4}$	9793.7×10^{-6}	43693	1.9091×10^9
2 : 1	$1\frac{1}{8}$	9793.7×10^{-6}	21847	0.2386×10^9
2 : 1	$2\frac{1}{4}$	9793.7×10^{-6}	61791	1.9091×10^9

Table 6.2 Numerical simulations for the broken dam problem

larger the water base is, the slower the water volume discharges. We also find that the front motion relates to the aspect ratio of water column γ. Accordingly, we have two dimensionless times[86], respectively,

$$T \equiv t\gamma\sqrt{\frac{g}{h}} = t\sqrt{\gamma\frac{g}{a}} \qquad \text{and} \qquad \tau \equiv t\sqrt{\frac{g}{a}}, \tag{6.4}$$

for front motion and volume discharge in the problem.

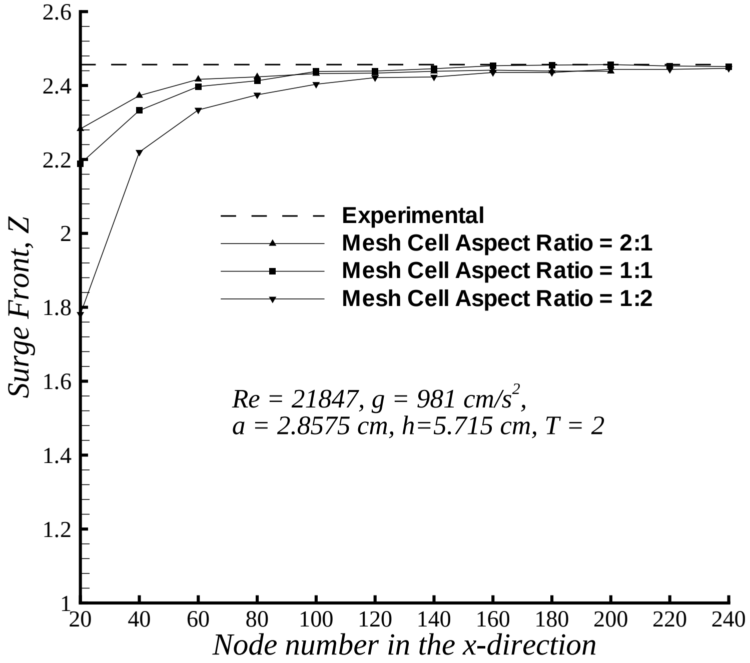

Figure 6.2 The surge front Z obtained on various mesh resolutions along the x-direction

The sensitivity of numerical solutions to grid resolution is examined in Figures 6.2 and 6.3 at $T = 2$ or $\tau = 1.414$ for the rectangle water with base $a = 1\frac{1}{8}$ in, where the mesh aspect ratio is defined as $\delta x/\delta y$. The physical domain of 16 $cm \times 6.4$ cm is thus divided into 160×64 uniform meshes ($\delta x = \delta y = 0.1$ cm). In the rest simulations ($a = 2\frac{1}{4}$ in), we chose $\delta x = \delta y = 0.2$ cm from the independence analysis of mesh resolution which is not shown. In the simulations, the computer program automatically adjusted the time steps. Despite the absence of water viscosity in [86], a water viscosity $\nu = 0.0097937$ cm^2/s at indoor temperature 20°C and a surface tension coefficient 73.05

dynes/cm were used. The experimental data in Figures 6.2 and 6.3 are quoted from Martin and Moyce[86], and so are those in Figures 6.5 through 6.9.

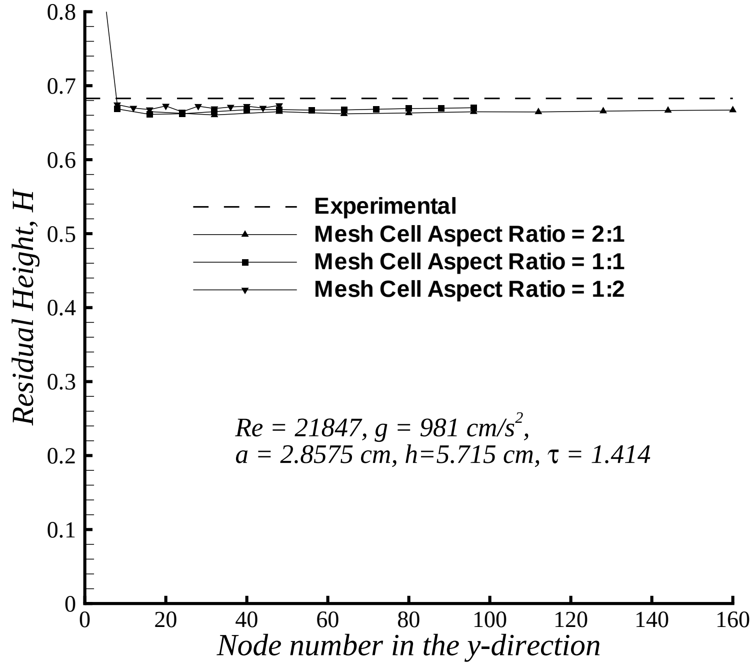

Figure 6.3 The residual height H obtained on various mesh resolutions along the y-direction

The configuration development of water column with time is shown in Figure 6.4. The ambient pressure p_1 is imposed on those not-immersed cell centers (refer to Section 5.4 of Chapter 5). The modification is thus verified by comparing the numerical data with those from the uncorrected approach, and the experimental data as demonstrated in Figure 6.5 through 6.9. Figures 6.5 through 6.7 present the water front positions with time at $\mathbf{Re} = 43693$, 21847, and 61791, respectively. Figures 6.8 and 6.9 show that the program simulations agree well with the experimental measurements of residual height of water column.

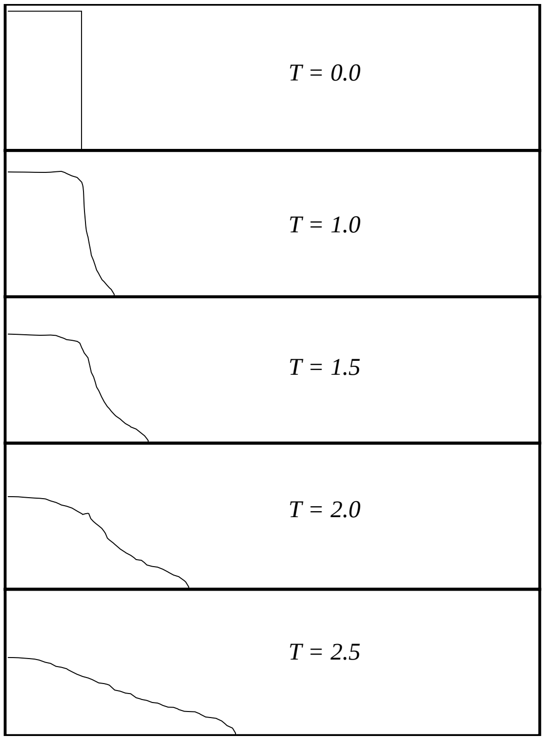

Figure 6.4 Free surface changing with time in the broken dam problem

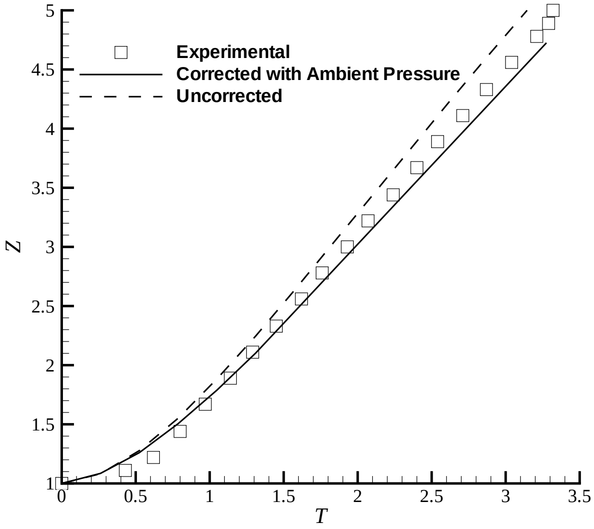

Figure 6.5 Water front moving with time, the aspect ratio of the column $\gamma = 1:1$ with base $a = 2\frac{1}{4}$ *in.*, $\mathbf{Re} = 43693$, $\mathbf{Ga} = 1.9091 \times 10^9$

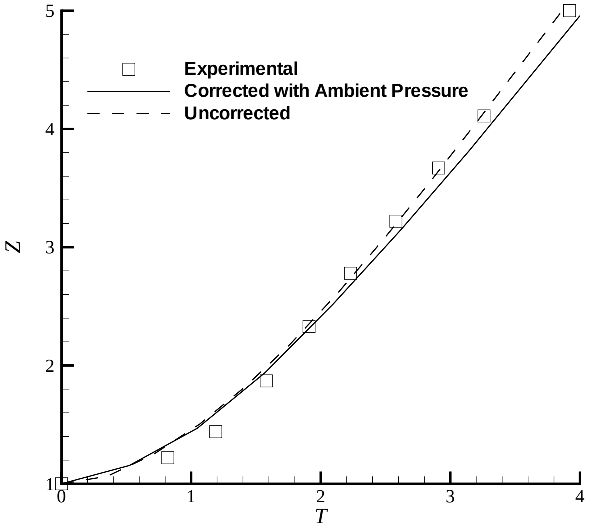

Figure 6.6 Water front moving with time, the aspect ratio of the column $\gamma = 2:1$ with base $a = 1\frac{1}{8}$ *in.*, $\mathbf{Re} = 21847$, $\mathbf{Ga} = 0.2386 \times 10^9$

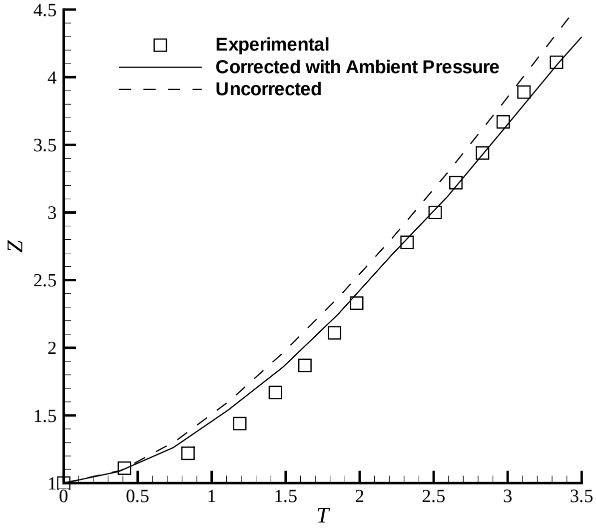

Figure 6.7 Water front moving with time, the aspect ratio of the column $\gamma = 2:1$ with base $a = 2\frac{1}{4}\ in.$, $\mathbf{Re} = 61791$, $\mathbf{Ga} = 1.9091 \times 10^9$

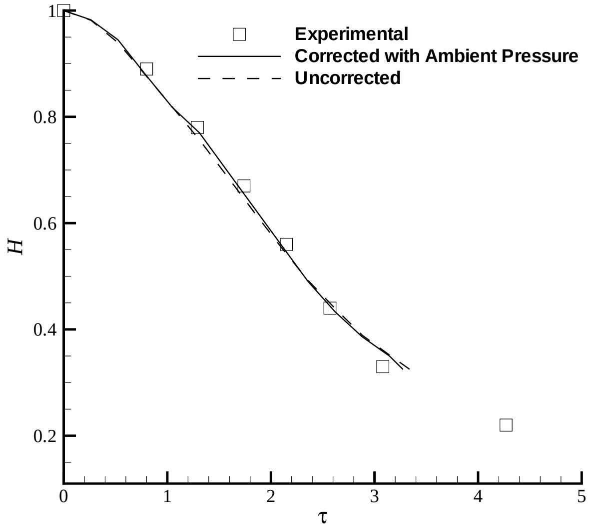

Figure 6.8 Height of the residual square column of water, base $a = 2\frac{1}{4}\ in.$

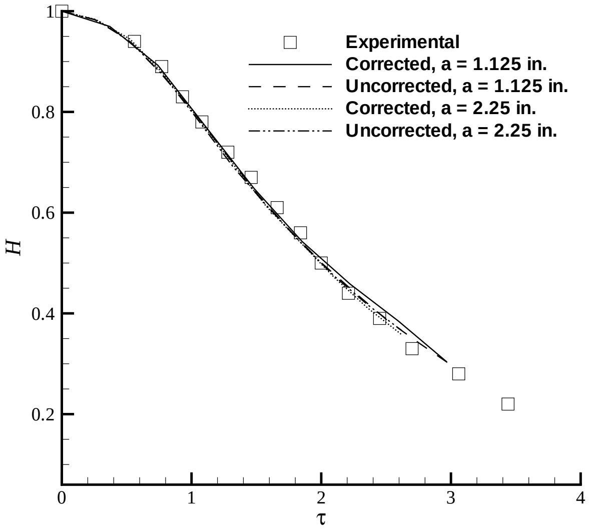

Figure 6.9 Height of the residual rectangular column of water with aspect ratio $\gamma = 2:1$

6.2 Undular Bore Problem

An undular bore is a well-behaved gravity wave with an advancing steep front formed from nonlinear solitary shallow water waves. The undular bore is a simplified hydrodynamic problem in which a bulk of water with constant depth under gravity moves toward a solid vertical wall at an initial constant velocity. This example imitates an undular bore formation that often happens when incoming sea water is reflected by a harbor wall, as shown in Figure 6.10.

Froude number is defined as follows:

$$\mathbf{Fr} \equiv \frac{U}{\sqrt{gh}} \tag{6.5}$$

where h is the bore depth and U is the flow velocity relative to the bore. The characteristic velocity $\sqrt{gh}$ is referred to, in the shallow water theory, as the propagation speed of small disturbances in analogy to *sound speed* in gas dynamics. A bore is analogous to a shock wave of gas dynamics in terms of the discontinuity in proximity of the bore front and wave propagation speed. Froude number is the hydrodynamics analogy of *Mach*

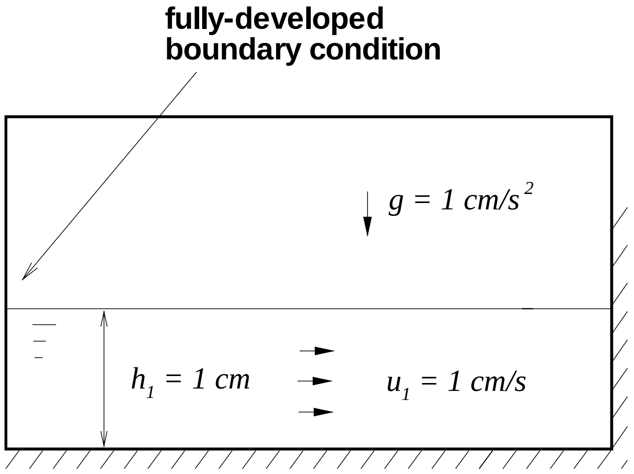

Figure 6.10 A bore reflected from a rigid wall

number in aerodynamics. When **Fr** > 1, the flow is supercritical; when **Fr** < 1, it is subcritical.

If a bore has a Froude number less than 1.7, the bore front has a regular shape and does not break. Hence it is termed *undular*. Lynch[88] presents a detailed description of various Froude numbers, in which an undular bore has an extent of **Fr** from 1 to 1.7. Stoker[87] provides fundamentals for bores, but no analytical solutions were derived for this example.

Figure 6.11 shows a typical bore with constant depths h_1 and h_2, and velocities u_1 and u_2 for both sides, where a control volume framed in the dashed lines is investigated to yield relations across the bore front. The subscripts 1 and 2 represent the front and the back sides of bore, respectively. The discontinuity or the bore front is featured by an elevation jump at the front position $x = \xi(t)$ from side 1 to side 2. Applying the conservation laws of mass and momentum on the control volume gives

$$\rho h_1 v_1 = \rho h_2 v_2 \tag{6.6}$$

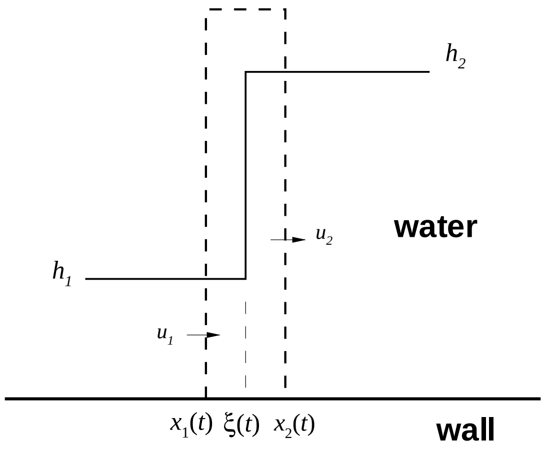

Figure 6.11 Illustration of a bore front

and

$$\rho h_1 v_1^2 + \frac{\rho g h_1^2}{2} = \rho h_2 v_2^2 + \frac{\rho g h_2^2}{2}, \tag{6.7}$$

where v_1 and v_2 are velocities of the incident and the departing flows relative to the front traveling speed $\dot{\xi}$, respectively:

$$v_1 = u_1 - \dot{\xi} \qquad \text{and} \qquad v_2 = u_2 - \dot{\xi}. \tag{6.8}$$

Eq. (6.7) is derived upon an approximation of hydrostatic pressure commonly employed in the shallow water theory and by integrating the hydrostatic pressure along the two vertical ends $x = x_1(t)$ and $x = x_2(t)$, at the limit when $x_2(t) \to x_1(t)$ in such a way that the front stays inside the control volume. Because the fluid is incompressible and is brought to still behind the front of the reflected bore, we have $u_2 = 0$ and $v_2 = -\dot{\xi}$. Then Eqs. (6.6) and (6.7) reduce, respectively, to

$$h_1(u_1 - \dot{\xi}) = h_2(-\dot{\xi}) \tag{6.9}$$

and

$$h_1(u_1 - \dot{\xi})^2 + \frac{g h_1^2}{2} = h_2(-\dot{\xi})^2 + \frac{g h_2^2}{2}. \tag{6.10}$$

Eqs. (6.9) and (6.10) can be directly obtained from Eq. (2.4).

The solution of $\dot{\xi}$ in terms of h_1, h_2, and u_1 from Eqs. (6.9) and (6.10) is

$$\dot{\xi} = -\frac{u_1}{\dfrac{h_2}{h_1} - 1} = \pm\sqrt{\frac{gh_1}{2}\left(1 + \frac{h_1}{h_2}\right)}, \tag{6.11}$$

where the signs on the RHS correspond to the direction in which the bore front moves. Eq. (6.11) can also estimate bore height h_2, given two incident conditions (h_1 and u_1), moving velocity of bore front $\dot{\xi}$, and g.

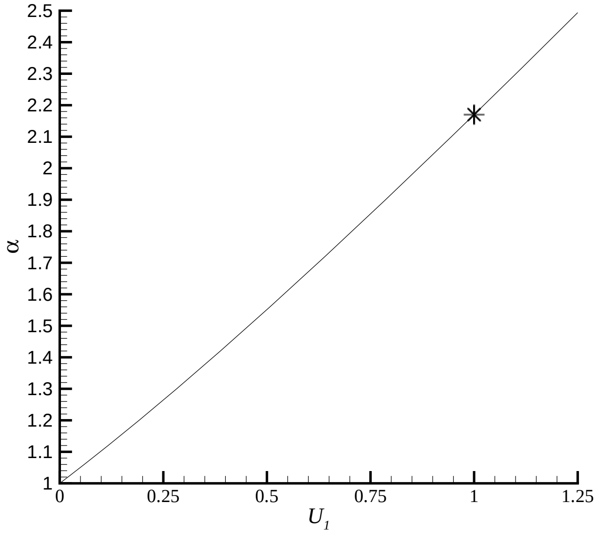

Figure 6.12 Height ratio versus dimensionless incident velocity

If we use

$$U_1 = \frac{u_1}{\sqrt{gh_1}} \qquad \text{and} \qquad \alpha = \frac{h_2}{h_1}. \tag{6.12}$$

to rewrite Eq. (6.11), we have

$$\frac{\dot{\xi}}{\sqrt{gh_1}} = -\frac{U_1}{\alpha - 1} = \pm\sqrt{\frac{1}{2}\left(1 + \frac{1}{\alpha}\right)}. \tag{6.13}$$

The Froude number of the incident flow, namely the LHS of Eq. (6.13), can be expressed in terms of U_1 and α:

$$\mathbf{Fr} = \left(\frac{\alpha}{\alpha - 1}\right) U_1 = \sqrt{\frac{\alpha(1+\alpha)}{2}}. \tag{6.14}$$

Accordingly, $\mathbf{Fr} > 1$ when $\alpha > 1$, and vice versa. Thus the incident flow is always supercritical, since $h_2 > h_1$ in the undular bore problem. At the critical Froude number for undular bore $\mathbf{Fr} = 1.7$, $\alpha = 1.9556$ and $U_1 = 0.8307$, upon which we can predict an undular reflected bore in nature.

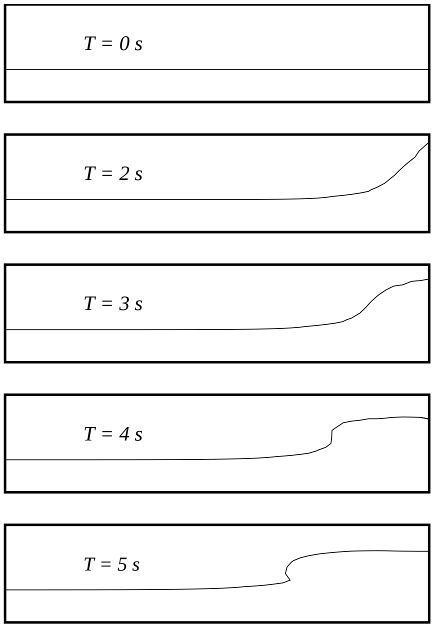

Figure 6.13 A reflected bore formation

The Froude number of the departing flow is given as follows:

$$\mathbf{Fr} = \sqrt{\frac{(1+\alpha)}{2\alpha^2}}, \tag{6.15}$$

which always falls between 0 and 1. Thus the departing flow is a subcritical flow.

Given $h_1 = 1\ cm$, $u_1 = 1\ cm/s$, and $g = 1\ cm/s^2$ as shown in Figure 6.10, we have solved Eq. (6.11) for h_2 or $h_2/h_1 = 2.1701$ using trial and error (see Figure 6.12). The second solution of h_2/h_1 to Eq. (6.11) is for a receding bore in Eq. (6.16), and the third is of no physical significance since it is less than zero. Consequently, the reflected bore will advance at a speed of $0.8547\ cm/s$ to the left as shown in Figure 6.13.

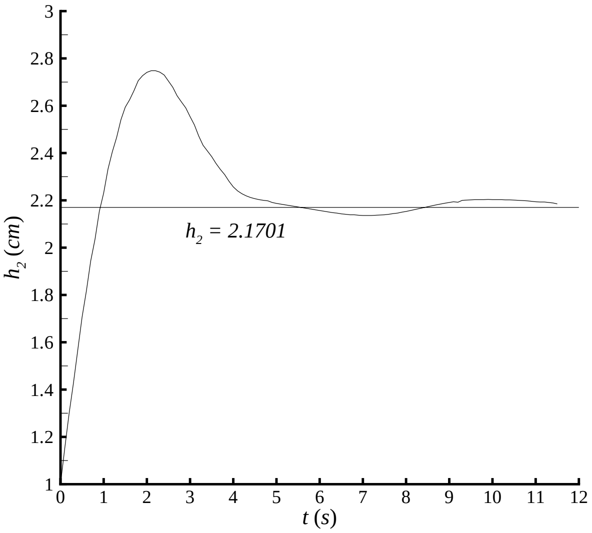

Figure 6.14 Hydraulic height of the reflected bore

Figure 6.13 shows variations of the reflected bore from the right rigid wall with time. Notice the bore breaks because the incident flow has **Fr** $= 1.8547 > 1.7$. From Figure 6.13, the crest of the bore advances faster than the trough after 5.0 s. Therefore the crest is to roll down ahead of the trough and the bore begins to break. Those are consistent with Lynch's description[88]. The water climbs the rigid wall when the wall reflects the incoming flow. The height of water onto the wall is named *hydraulic jump height*, which is approximated to the height of the back side of bore in an analytical solution; for instance, $h_2 = 2.1701$ cm in the example. Figure 6.14 shows that the numerical results of hydraulic height converges to the analytical prediction. The positions of the bore front have been recorded from the numerical results as shown in Figure 6.15; they agree with the analytical solution, which is given by Eq. (6.13).

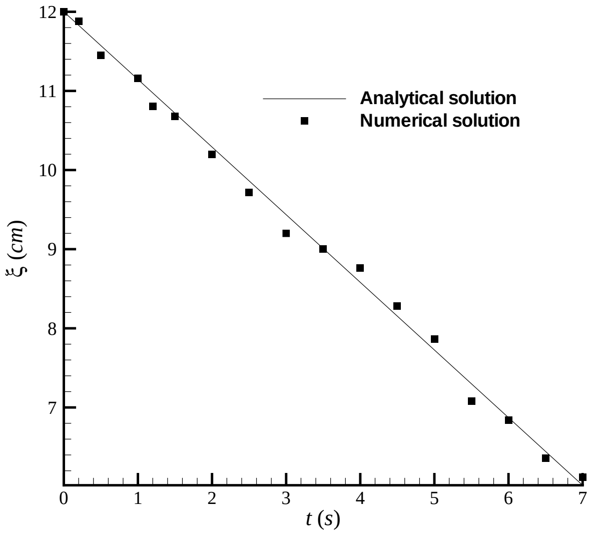

Figure 6.15 Traveling of the reflected bore front with time

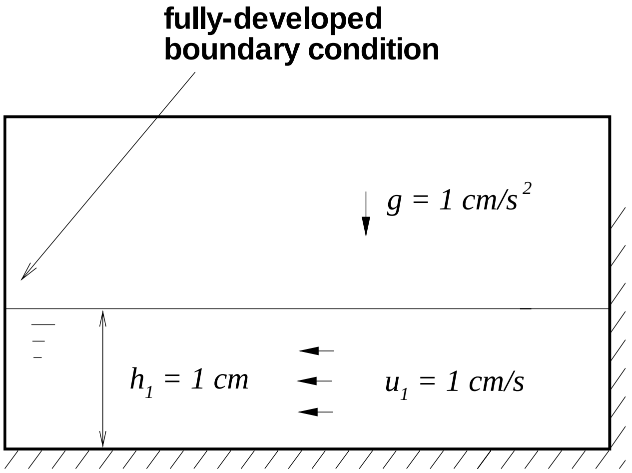

Figure 6.16 A receding bore problem

In Figure 6.13, the traveling velocity of the bore front is opposite to the incident flow, therefore the bore depth is higher than that of the incident flow. If a bore travels in the direction of the incident flow, the result is a *receding bore*, as shown in Figure 6.16 with the depth ratio $\alpha < 1$, namely $h_2 < h_1$. Eq. (6.11) also gives traveling velocity of a receding bore but in a different form,

$$\dot{\xi} = \frac{u_1}{1 - \dfrac{h_2}{h_1}} = \pm\sqrt{\frac{gh_1}{2}\left(1 + \frac{h_1}{h_2}\right)}. \tag{6.16}$$

The signs on RHS of Eq. (6.16) are determined according to the direction in which the bore travels. In Figure 6.11 for the receding bore problem, one may either change the height on both sides of the discontinuity or switch the subscripts 1 and 2 to guarantee $\alpha < 1$.

The Froude numbers for incident and departing flows, respectively, in terms of dimensionless incident velocity U_1 and height ratio α are given:

$$\mathbf{Fr} = \left(\frac{\alpha}{1-\alpha}\right) U_1 = \sqrt{\frac{\alpha(1+\alpha)}{2}} \tag{6.17}$$

and

$$\mathbf{Fr} = \sqrt{\frac{1+\alpha}{2\alpha^2}}. \tag{6.18}$$

Contrary to the advancing bore, a receding bore has $\mathbf{Fr} < 1$ for incident flow and $\mathbf{Fr} > 1$ for departing flow since $\alpha < 1$ from Eqs. (6.17) and (6.18).

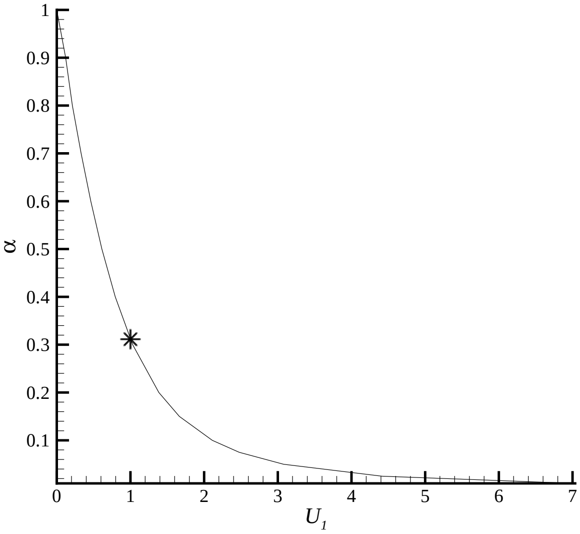

Figure 6.17 The ratio of flow heights as a function of the dimensionless incident velocity

The height of water behind the receding bore can be estimated using Eq. (6.16); for instance, $\alpha = 0.31113$ as shown in Figure 6.17, if $g = 1\ cm/s^2$, $h_1 = 1\ cm/s$, and $u_1 = -1\ cm/s$, as noted in Figure 6.16. It is validated by the numerical solution in Figure 6.18, where the height of 0.31113 cm is denoted by the dashed lines. Consequently, the bore traveling velocity $\dot{\xi} = 1.452 > 1\ cm/s$, meaning that the bore travels faster than the flow. Interestingly, this velocity is also greater than that of the reflected bore front 0.8547 cm/s, obtained earlier.

In hydraulics, the supercritical region of the flow is customarily designated as the front side of the discontinuity of height and the subcritical region as the back side. Receding bore is thus named in terminology for the discontinuity of height that recedes backward, as shown in Figure 6.18.

The simulations of undular and receding bores were made on a 12 cm × 4.8 cm physical domain with a grid resolution of 50 × 24 ($\delta x/\delta y = 1.2$), where convergent solutions have been obtained.

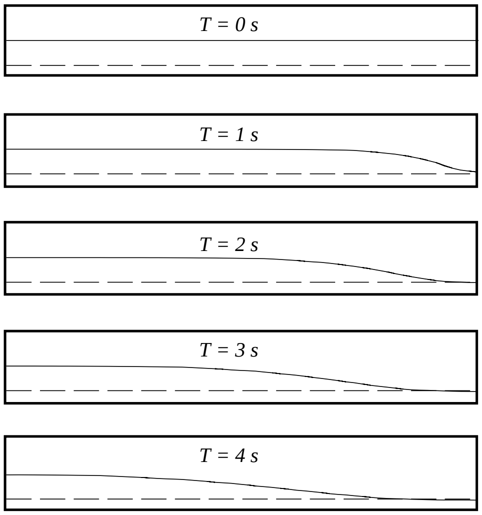

Figure 6.18 The development of a receding bore

6.3 Sluice Gate Problem

Sluice gates (Figure 6.19) are widely used to regulate and measure flow rate in open channels or rivers for hydro power plants or irrigation systems. In this example calculation, we compare contraction coefficient, defined as follows, by simulating the downstream free surface of a sluice gate flow:

$$C_c = \frac{h_2}{b} \tag{6.19}$$

where h_2 is the water height at *vena contracta* downstream and b is the sluice gate opening height (refer to Figures 6.19 and 6.20).

The value of C_c ranges from 0.61 to 1.0, depending on the angle of the gate with respect to the horizontal direction[89, 90]. The contraction coefficients for radial slide

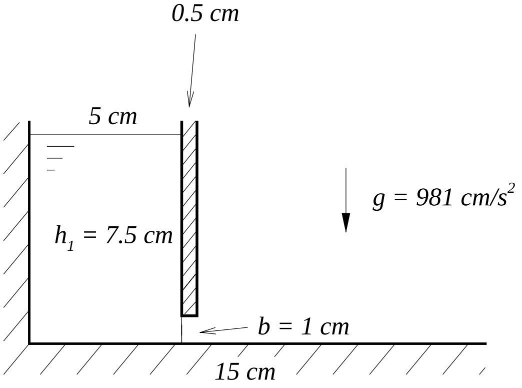

Figure 6.19 Diagram of a sluice gate

gates ($0.648 \sim 0.724$) are higher than those for sharp gates ($0.58 \sim 0.63$). A typical sharp-edged contraction coefficient is 0.61. Lin et al (2002) demonstrated the experimental contraction coefficients in good agreement with the theoretical or reported data[90].

L_x	L_y	U	V
$5\ cm$	$1\ cm$	$85.78\ cm/s$	$17.16\ cm/s$

Table 6.3 Parameters in scaling of the sluice gate problem

In the simulation, the sharp edge with 0.5 cm thickness was chosen for the sluice gate shown in Figure 6.19. Unlike in [89] and [90], water is stored in a $7.5\ cm \times 5.0\ cm$ container. The water will drop from the initial height $h_1 = 7.5\ cm$ to zero after the sluice gate is open (see Figure 6.19). We can expect an unsteady C_c because the water volume is not semi-infinite and it escapes through the sluice gate from a state of rest. However, some of h_2 at *vena contracta* during the time interval of $0.125\ s < t < 0.225\ s$ were recorded from the numerical results; they can be regarded as pseudo steady-state. The contraction coefficient C_c of 0.635 to 0.67 were observed for both the unscaled and scaled domains as shown in Figure 6.20.

Appropriate parameters were selected to satisfy the continuity equation as listed in Table 6.3, and two grid resolutions were implemented on the scaled domains as well as an unscaled case (see Table 6.4). Notice that the characteristic speed U is computed according to Eq. (6.1). The discrepancies in Figure 6.20 are ascribed to the different resolutions on unscaled and scaled domains.

domain	unscaled	scaled	scaled
resolution	450×240	90×240	180×480

Table 6.4 Resolutions on the unscaled and scaled domains

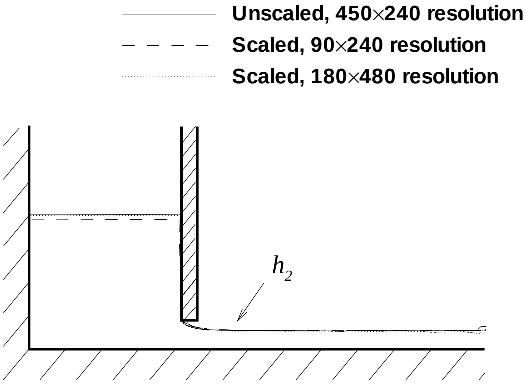

Figure 6.20 Water height 0.225 s after the sluice gate is open

6.4 Normal and Curvature Calculations

To seek an accurate and reliable scheme for evaluating curvature, two extreme examples, planar and circular free surfaces, are analyzed as illustrated in Figure 6.21. In Figure 6.21(a) the planar surface tilts at an inclined angle θ; undoubtedly, any planar surface has a zero curvature. The curvature of a circular surface is the inverse of its radius R and independent of the cylindrical coordinate ϕ, as depicted in Figure 6.21(b).

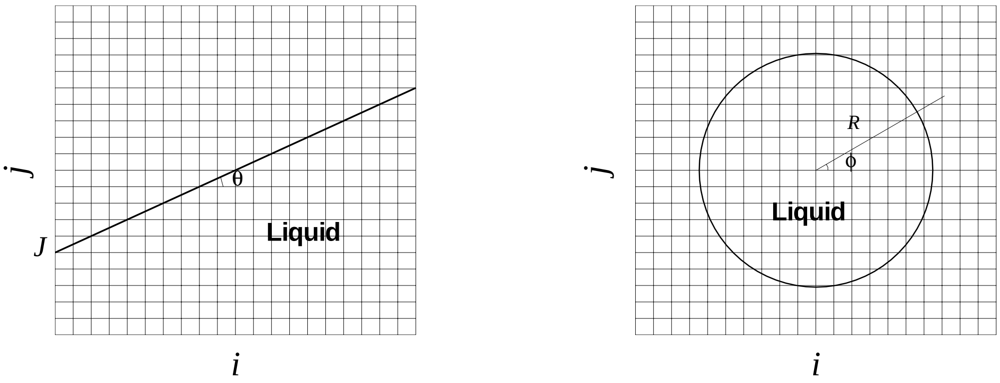

(a) An inclined planar free surface with $\kappa = 0$ and $\tan^{-1}\theta = 1/2$

(b) A circular free surface with $\kappa = 1/R$, where R is the radius of the circle

Figure 6.21 Two extreme examples of free surface

Along the inclined plane, any VOF function describing the free surface varies periodically. If the free surface is aligned with the diagonal direction of two horizontally adjoining cells, as seen in Figure 6.21(a), we have

$$F_{i,j} = \begin{cases} 0.25 & i = 1, 3, 5, ... \quad j = J, J+1, J+2, ...; \\ 0.75 & i = 2, 4, 6, ... \quad j = J, J+1, J+2, ..., \end{cases} \tag{6.20}$$

where J is the y-direction index of the leftmost cell. Any planar free surface has periodical distribution of F unless $\theta = \pm 0°$ or $\pm 90°$. Notice that the periodicity cannot simply be mitigated by higher grid resolutions. Eq. (6.20) suggests that the local surface curvature is independent of grid size.

From Eq. (3.10) or (5.11), we find the order of magnitude of curvature computed on a grid having size h:

$$\kappa = \mathcal{O}(1/h) \quad \text{or} \quad \text{a constant.} \tag{6.21}$$

It demonstrates that a finite value can be sought for curvature if the algorithm implemented is convergent; otherwise, the computed curvature diverges with finer grid sizes.

The diverging errors come from inaccurate estimates of gradient of $\hat{n}$ in the normal direction. Because $\vec{n}$ and $\hat{n}$ are continuous only in the tangential direction of a free surface, surface curvature reflects the variations of unit normal along the tangential direction. Absolutely, the contribution of the normal direction to κ should vanish in Eq. (3.10), namely in Eq. (5.11) $\hat{n}_{xi+1/2,j} = \hat{n}_{xi-1/2,j}$ or $\hat{n}_{yi,j+1/2} = \hat{n}_{yi,j-1/2}$, which is consistent with the normals in the DA algorithm formulations (see Eqs. (5.7) and (5.8)). The convolution of Eq. (5.3) also ensures a mollified VOF or color function to yield equal component of unit normal in the normal direction.

Grid Resolution	$\partial F/\partial x$	$\partial F/\partial y$	θ
100×100	50	-100	26.5651°
200×200	100	-200	26.5651°

Table 6.5 Gradients and normal by the DA algorithm at cell of $F = 0.75$ on an inclined planar free surface with $\theta = 26.5651°$

Grid Resolution	$\partial F/\partial x$	$\partial F/\partial y$	θ
100×100	37.500	-50.000	36.8699°
200×200	75.000	-100.000	36.8699°

Table 6.6 Gradients and normal by the MAC scheme at cell of $F = 0.75$ on an inclined planar free surface with $\theta = 26.5651°$

Grid Resolution	$\partial F/\partial x$	$\partial F/\partial y$	θ
100×100	21.875	-46.875	25.0169°
200×200	43.750	-93.750	25.0169°

Table 6.7 Gradients and normal by the ALE scheme at cell of $F = 0.75$ on an inclined planar free surface with $\theta = 26.5651°$

A constant normal direction of θ and a zero curvature have been obtained using the DA method for the inclined plane example in comparison with the MAC and ALE schemes as shown in Tables 6.5 through 6.7. The ALE scheme yielded some non-zero curvatures, ± 11.465 on 100×100 grid and ± 22.930 on 200×200 grid, respectively, as plotted in Figure 6.22.

Both ALE[20] and MAC[21] schemes in Appendix B and textbook[71] failed for the inclined planar free surface even with a smoothed F computed using Eq. (B.23). The errors grow greatly with higher grid resolutions because the frequency of F may increase on finer grids. Higher resolutions worsen the numerical results of curvature according to Eqs. (6.20) and (6.21).

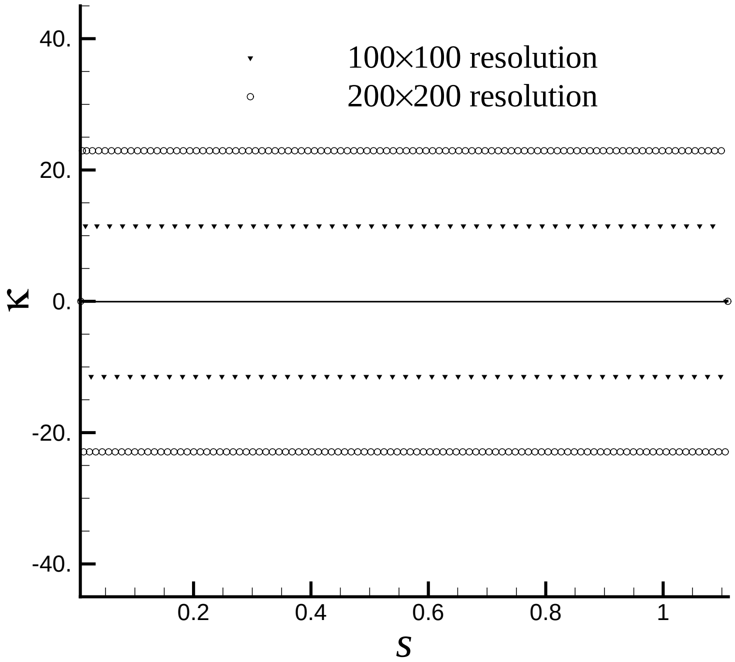

Figure 6.22 Curvature calculation using the ALE scheme for an inclined planar free surface with $\theta = 26.5661°$ on 100×100 and 200×200 grids

Table 6.8 gives results of angle ϕ and curvature κ computed for a circular droplet of $R = .25$ ($\kappa = 4.0$, see Figure 6.21(b)) using the DA and ALE methods. The errors from the ALE method grow fast on finer grids as expected, whereas the results of ϕ and κ from the DA method converge to the exact values, respectively. Notice that Table 6.8 only lists some results near $\phi = 20°$, $30°$, and $45°$. In this example some negative curvatures are found if the ALE method is used with $\tilde{c} = F$. Additional observation concludes that some curvatures by the ALE method increase greatly with higher grid resolutions (see Table 6.8). As a result, spurious or *parasitic currents* reported in [8, 17, 25] occur within a circular water drop in equilibrium and with zero initial velocity.

6.5 Elimination of Spurious Currents

Spurious currents are found not only in the surface tension simulation for a circular droplet but also along the inclined plane of zero curvature perpendicular to gravity, as

Grid	Angle	DA		ALE	
Resolution	ϕ_{exact}	ϕ	κ	ϕ	κ
30 × 30	20.7722535°	21.5832020°	4.00678072	18.0678429°	-4.03614702
40 × 40	18.4349476°	19.0001060°	4.00346803	15.3145517°	-4.66110668
80 × 80	19.7988752°	19.7336973°	4.00088752	19.4134637°	13.5760513
100 × 100	20.6235302°	20.4934169°	4.00058348	18.8418308°	31.0885104

Grid	Angle	DA		ALE	
Resolution	ϕ_{exact}	ϕ	κ	ϕ	κ
30 × 30	30.9637555°	30.1238560°	4.01000643	28.2994535°	13.2466290
40 × 40	28.4956376°	28.4221038°	4.00514380	27.4053610°	7.96860282
80 × 80	30.7189033°	30.8486414°	4.00145432	29.4021396°	-4.73743286
100 × 100	28.3792420°	28.0440938°	4.00080537	25.8834186°	27.2777916

Grid	Angle	DA		ALE	
Resolution	ϕ_{exact}	ϕ	κ	ϕ	κ
30 × 30	45°	45°	4.02651539	45°	9.65894247
40 × 40	45°	45°	4.01741378	45°	3.21078864
80 × 80	45°	45°	4.00391085	45°	6.19854908
100 × 100	45°	45°	4.00245581	45°	7.54760344

Table 6.8 Surface normal directions and curvatures computed using the DA and ALE methods for a circular droplet ($\kappa_{\text{exact}} = 4.0$)

shown in Figures 6.24 through 6.26 if using the MAC or ALE method. Both methods are unable to yield correct curvature in the circular droplet example. The miscalculation of density at the interfacial control cell centers is another source of the spurious currents. Surface tension force is evaluated by linear interpolation, namely Eqs. (B.21) and (B.22), which are physically incorrect. The numerical approach for the PPE presented in section 3.4 of Chapter 3 may incur some spurious currents as well. Consequently, the spurious currents grow with time and become denser on grids of higher resolution in both examples (see Figures 6.24 to 6.26 and Figures 6.27 to 6.29). The pressures inside the circular free surface are distorted using the CSF model. Hence, the pressure jump of $\sigma\kappa$ in Laplace's formula is never observed as shown in Figures 6.30 through 6.32.

Recalling Eqs. (3.28) and (3.29), we let the velocity, viscous, and gravity terms equal

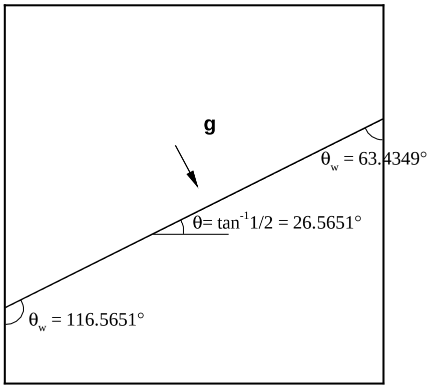

Figure 6.23 A motionless inclined planar free surface with gravity perpendicular to the surface

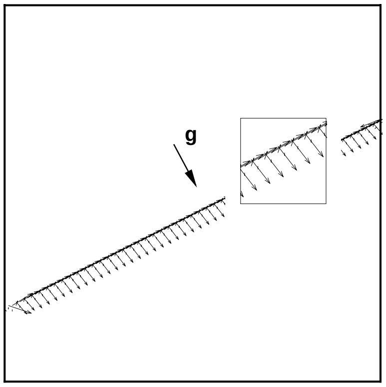

Figure 6.24 Spurious currents found along an inclined plane, on 100 × 100 grid, when $t = 0.001\ s$

to zero at time level n, then we can have

$$\nabla p^{\mathrm{n}+1} = \vec{F}^{\mathrm{n}}_{\mathrm{sv}} = \sigma\kappa\nabla F^{\mathrm{n}} \tag{6.22}$$

if the velocity $\vec{V}^{\mathrm{n}+1} = 0$. Eq. (6.22) is a sufficient-necessary condition to be satisfied that spurious currents are not induced after time advances δt^{n}. For a configuration of free surface with $\delta x_i = \delta y_j$, as shown in Figure 6.33, it yields as follows from Eq. (6.22) on control cell $(i+1/2, j)$ and $(i+1, j+1/2)$ without losing generality:

$$-\sigma\kappa_{i+1,j}(c_1 + c_2)\left(\frac{\partial F}{\partial y}\right)_{i+1,j} = \sigma\kappa_{i,j}a\left(\frac{\partial F}{\partial x}\right)_{i,j} + \sigma\kappa_{i+1,j}b\left(\frac{\partial F}{\partial x}\right)_{i+1,j} \tag{6.23}$$

where a, b, and c are immersed depth, $c_1 + c_2 = c$, $p_{i+1,j+1} = p_{i,j}$, and the superscript of time level n is ignored. Finally, simplification of Eq. (6.23) gives,

$$\kappa_{i,j} = \kappa_{i+1,j} \tag{6.24}$$

for two interfacial cells, because the free surface is assumed to be horizontally oriented as illustrated in Figure 6.33, namely

$$a\left(\frac{\partial F}{\partial x}\right)_{i,j} = c_2\left(-\frac{\partial F}{\partial y}\right)_{i,j}, \qquad b\left(\frac{\partial F}{\partial x}\right)_{i+1,j} = c_1\left(-\frac{\partial F}{\partial y}\right)_{i+1,j}, \tag{6.25}$$

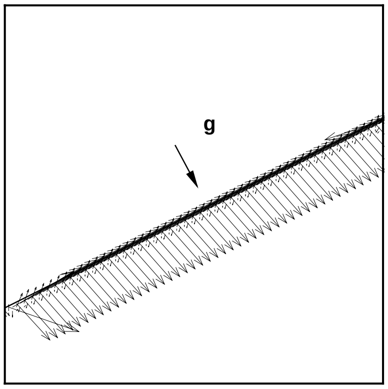

Figure 6.25 Spurious currents found along an inclined plane, on 100 × 100 grid, when $t = 0.005\ s$

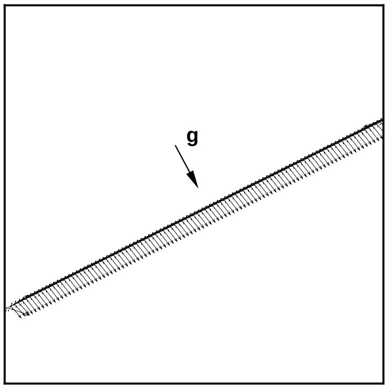

Figure 6.26 Spurious currents found along an inclined plane, on 100 × 100 grid, when $t = 0.005\ s$

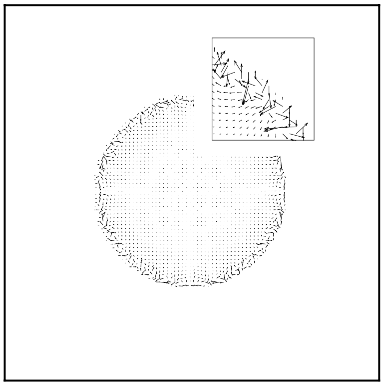

Figure 6.27 Spurious currents on a circular droplet, on 100×100 grid, when $t = 0.001\ s$

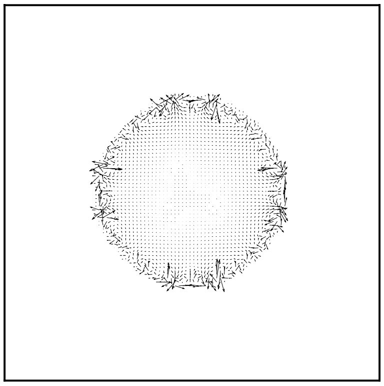

Figure 6.28 Spurious currents on a circular droplet, on 100×100 grid, when $t = 0.005\ s$

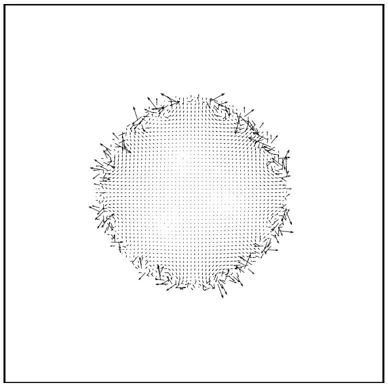

Figure 6.29 Spurious currents on a circular droplet, on 200×200 grid, when $t = 0.001\ s$

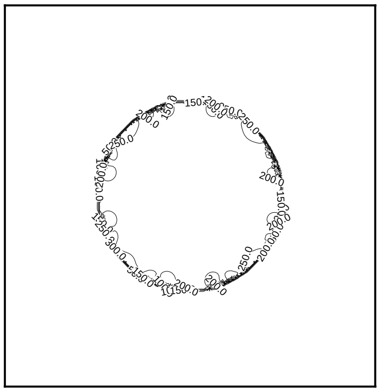

Figure 6.30 Isobaric diagram of a droplet with spurious currents, on 100×100 grid, when $t = 0.001\ s$

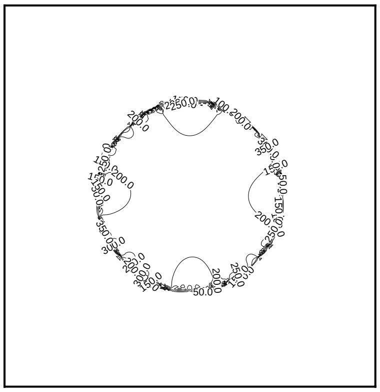

Figure 6.31 Isobaric diagram of a droplet with spurious currents, on 100×100 grid, when $t = 0.005\ s$

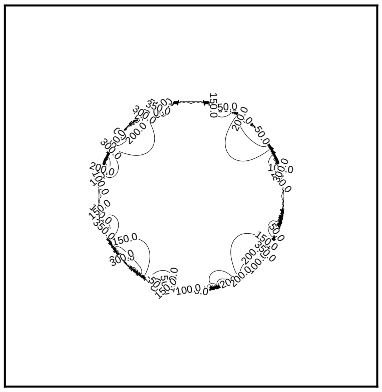

Figure 6.32 Isobaric diagram of a droplet with spurious currents, on 200×200 grid, when $t = 0.001\ s$

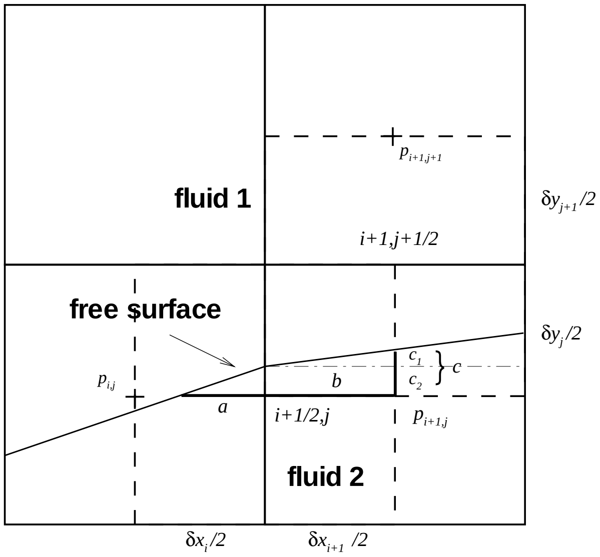

Figure 6.33 A horizontally tilted configuration of free surface

and

$$\left(\frac{\partial F}{\partial y}\right)_{i,j} = \left(\frac{\partial F}{\partial y}\right)_{i+1,j} = -\frac{1}{\delta y_j}. \tag{6.26}$$

Eq. (6.24) can be extended to any other interfacial cells due to transitivity. The proposition of equal curvature on a circular free surface must be satisfied in any algorithms for a circular droplet simulation; otherwise, spurious currents are incurred. By the new method given in Section 5.2 of Chapter 5, a constant local curvature $1/R$ is obtained for a circular droplet with radius R.

Another corollary derived from the proceeding approach is that in a well-represented circular droplet by the VOF method, F functions near hybrid sublayer cells (refer to Figure 5.8) should be symmetric about the diagonal direction of $\phi = \pm 45^\circ$ or $\pm 135^\circ$, as shown in Figure 5.5. Otherwise, restoring force, namely surface tension force, is reproduced due to the curvature difference to recover the free surface to be a symmetric droplet.

The maximum spurious currents listed in Table 6.9 shows the magnitude of the residual currents is found as low as 10^{-4} cm/s at $t = 10^{-6}$ s on a unity domain with two grid resolutions if using the modified approach and thus the truncation errors $\mathcal{O}(h^2)$

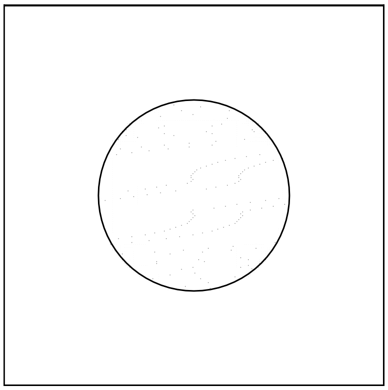

Figure 6.34 Velocity distribution on a circular droplet with the improved approach, at $t = 0.001\ s$, on 100×100 grid

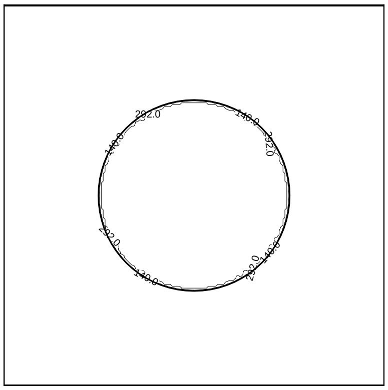

Figure 6.35 Isobaric diagram of a droplet with the improved approach, at $t = 0.001\ s$, on 100×100 grid

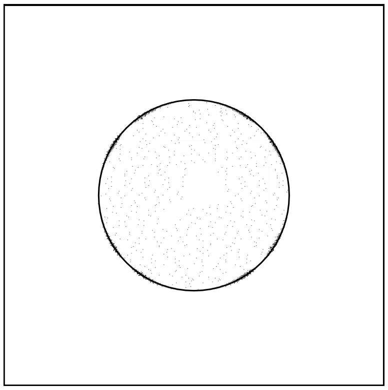

Figure 6.36 Velocity distribution on a circular droplet with the improved approach, at $t = 0.001\ s$, on 200×200 gird

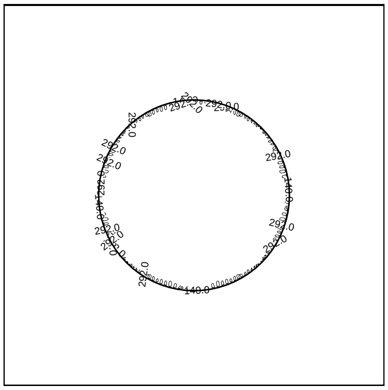

Figure 6.37 Isobaric diagram of droplet with the improved approach, at $t = 0.001\ s$, on 200×200 grid

Resolution	Grid Size	CSF	Reconstructed CSF
100×100	10^{-2}	10^{-2}	10^{-4}
200×200	$.5 \times 10^{-2}$	10^{-1}	10^{-4}

Table 6.9 Maximum velocity (cm/s) in spurious currents at $t = 10^{-6}\ s$

of the second-order accurate algorithms primarily appear in the simulation (also see Figure 6.38). From Figure 6.38, the magnitude of spurious currents is suppressed by up to three orders. Besides, the improved pressure approach attains the pressure jump $\sigma\kappa(=292\ dynes/cm^2)$ as in Laplace's formula near the free surface and over the entire flow field, where $\sigma = 73\ cm/s$ and $\kappa = 4\ cm^{-1}$ as shown in Figures 6.35 and 6.37.

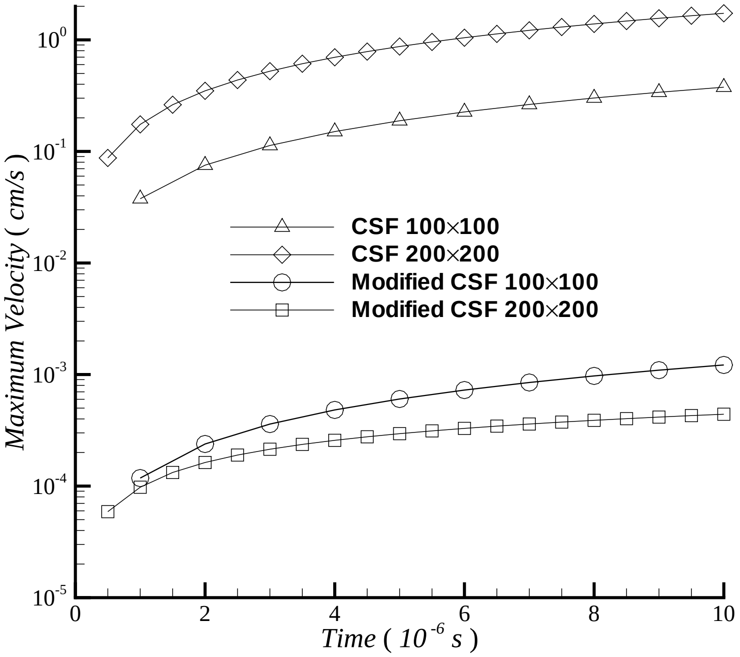

Figure 6.38 A comparison of spurious currents growth

CHAPTER 7 ANALYSIS OF MELT SPINNING

Section 7.1 presents physical and thermodynamical properties for Fe_{75}-Si_{10}-B_{15} (at.%) alloy, some of which are calculated using theoretical or experimental method. The nucleation temperature and critical cooling rate for production of amorphous alloy are estimated in Section 7.2 in two different ways. Two TTT diagrams also appear in the section for the alloy.

Clarification of the upstream and downstream of a melt pool, as discussed in Section 7.3, runs contrary to those in the papers[2, 34–36]. In Section 7.4, I enunciate some transformations of a 3D free-jet melt spinning to 2D simulation and calculation. The computer program simulates the melt jet impingement on a rotating wheel, and yields numerical results of velocity and temperature, as shown in Section 7.5. An estimate of ribbon thickness is derived in Section 7.6. From the thermal analysis of melt spinning and glass formation in Section 7.7, two thermal conditions for amorphous production emerge along with a work range of the wheel speed. Section 7.8 proves the postulation of 1D thermal diffusion in melt spinning. Heat transfer coefficients and melt cooling rates are computed in Section 7.9, and criteria are established in Section 7.10 for amorphous formation of Fe_{75}-Si_{10}-B_{15} (at.%).

7.1 Physical and Thermodynamical Properties of Fe-Si-B

Some physical properties of elements Fe, Si, and B are summarized in Tables 7.1. Physical and thermodynamical properties of Fe_{75}-Si_{10}-B_{15} (at.%) alloy are calculated or quoted, as listed in Tables 7.2 and 7.3, respectively. The density ρ in Table 7.3 is for an amorphous state; however, it is reasonable to assume the alloy volume does not change in phase transition. The atomic weight of Fe_{75}-Si_{10}-B_{15} (at.%) is calculated by the molar or atomic weight and at.% of each element given in Table 7.1. The molar volume of Fe-Si-B is calculated by

$$V_a = \frac{\text{Atomic Weight}}{\rho} \tag{7.1}$$

and the effective molecular diameter d_m is approximately estimated by

$$V_a = \frac{1}{6}\pi d_m^3 N. \tag{7.2}$$

	Fe	Si	B
Atomic Radius ($picometer$)	124.1	117	83
Atomic Weight (g/mol)	55.847	28.086	10.81
Liquidus Density (g/cm^3)	6.98	2.57	2.08
Melting Temperature (K)	1811	1687	2349
Latent Heat (kJ/mol)	13.81	50.21	50.2
Heat Capacity at 298K ($J/molK$)	25.10	19.789	11.087
Thermal Conductivity (W/mK)	80	150	27

Table 7.1 Physical properties of Fe, Si, and B

ρ (kg/m^3)	$7.3 \sim 7.5 \times 10^3$[91]
Atomic Weight (g/mol)	46.314
V_a (m^3/mol)	$6.34 \sim 6.18 \times 10^{-6}$
N_v ($1/m^3$)	$9.498 \sim 9.744 \times 10^{28}$
d_m (m)	$2.720 \sim 2.695 \times^{-10}$
$\theta,\ f(\theta)$	$37°,\ 0.0284$
ν at T_m (m^2/s)	2.8×10^{-6}[91], 2.35×10^{-5}[76]
μ at T_m (kg/ms)	0.0207[91], 0.1736[76]

Table 7.2 Physical properties of Fe_{75}-Si_{10}-B_{15} (at.%) alloy

We lack experimental data of wetting angle θ. It is assumed to be 37° in Table 7.2 and the reduced factor $f(\theta)$ is thus 0.0284 from Eq. (4.19). The viscosity μ is given in the Vogel-Fulcher-Tammann form if μ_0 is determined using Eq. (4.25)[76],

$$\mu = 6.374 \times 10^{-5} \exp\left(\frac{3.35 \times 1419}{T - 818}\right) \qquad kg/ms, \tag{7.3}$$

where $T_m = 1419\ K$ and $T_g = 818\ K$ are chosen from [48] (see Table 7.3), and $b = 3.35$ in Eq. (4.24). Accordingly, the dynamic viscosity of the alloy μ reaches 10^{12} kg/ms at $T_a = 945.5\ K$ by Eq. (7.3), around which the melt is in an amorphous state[4].

T_m (K)	1419[48], 1456[91]
T_g (K)	818[48]
T_a (K)	945.5[76]
L (kJ/mol)	22.91
L (kJ/kg)	4.9467×10^2
σ_{LS} (N/m)	0.3674
k (W/mK)	80
c_S, c_L (kJ/kgK)	0.485

Table 7.3 Thermodynamical properties of Fe_{75}-Si_{10}-B_{15} (at.%) alloy

Notice in Tables 7.2 and 7.3, those quoted from [48] are for Fe_{79}-Si_{10}-B_{11} (at.%) and those from [91] are for Fe_{80}-Si_{15}-B_{15} (at.%). Interestingly, the viscosities at the melting temperature from [48] are ten times greater than that from [91]. The latent heat L in kJ/mol (see Table 7.3) is computed by the latent heat and at.% of each element from Table 7.1. The surface tension at the solid/liquid interface is obtained using Eq. (4.16), where $\alpha = 0.62$. The specific heat of melt (liquidus) is assumed to be equal to that of a solidus state, which is estimated by the heat capacity and at.% of each element at 298 K, also shown in Table 7.1.

7.2 Nucleation Temperature and Critical Cooling Rate

The role of the rotating wheel in melt spinning is twofold: a heat sink to undercool the molten flow and a catalyst to crystallization. Based on the nucleation theory in Section 4.3 of Chapter 4 and the physical and thermodynamical properties given in Section 7.1, we can estimate the nucleation temperature and the critical cooling rate of Fe_{75}-Si_{10}-B_{15} (at.%) alloy.

Generally, the melt begins to crystallize under some conditions through heterogeneous nucleation. If there is no impurity in the melt, the nuclei form first on the contact surface of the spinning wheel, as illustrated in Figure 7.1. Following are the criteria of the occurrence of nuclei on the quench contact surface according to Eqs. (4.23), (4.26), and (4.27):

$$n = \int_{T_m}^{T_n} \frac{I_s \Delta x^2}{\dot{T}} dT = 1 \tag{7.4}$$

where the characteristic length Δx is chosen $3.741 d_m \approx 10^{-9}$ m, as given in Table 4.2

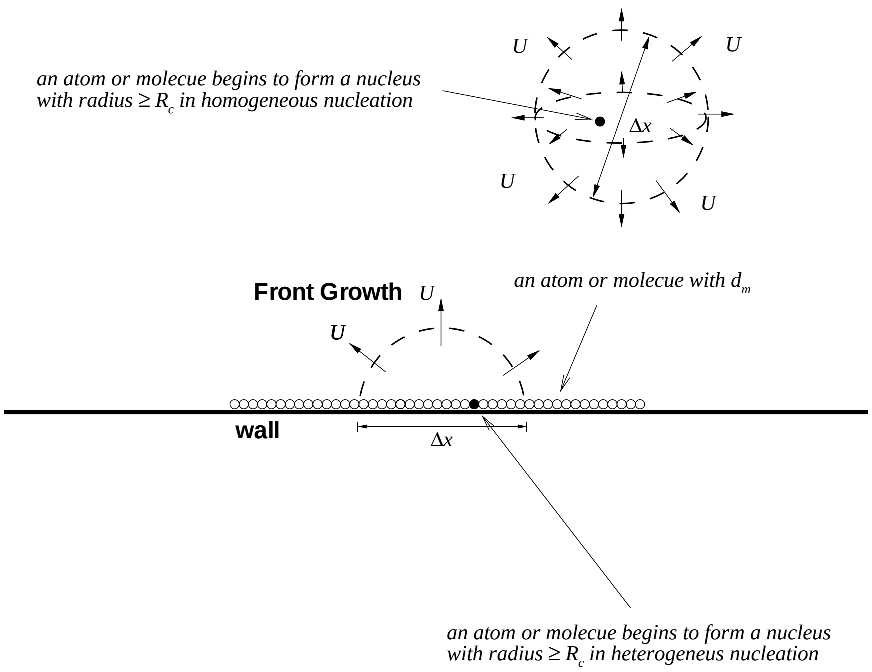

Figure 7.1 Nucleation in the melt or on the wall surface (not to scale)

for the melt. The nucleation temperature T_n is computed by numerical integration of Eq. (7.4) at a series of cooling rates. As listed in Table 7.4, there is at least one occurrence of nucleation found in the control area until the cooling rate $\dot{T}$ reaches 10^6 K/s. Therefore, 10^6 K/s can be seen as the critical cooling rate ε_{cr}, and the corresponding lowest temperature 1069 K is the nucleation temperature T_n from the table.

$\dot{T}$ (K/s)	10^{-1}	10^0	10^1	10^2	10^3	10^4	10^5	10^6
T_n (K)	1224	1214	1202	1188	1168	1140	1069	–

Table 7.4 Nucleation temperatures under given cooling rates for Fe-Si-B

The Time Temperature Transformation (TTT) diagrams are plotted in Figures 7.3 and 7.2 by setting the fraction of crystal as $1\%^{2/3}$ of the contact area, namely

$$x = \frac{\pi}{3} I_s U^2 t^3 = 1\%^{\frac{2}{3}}, \tag{7.5}$$

where U is the growth rate of crystallization on a quench wheel (refer to Eq. (4.31) and Figure 7.1).

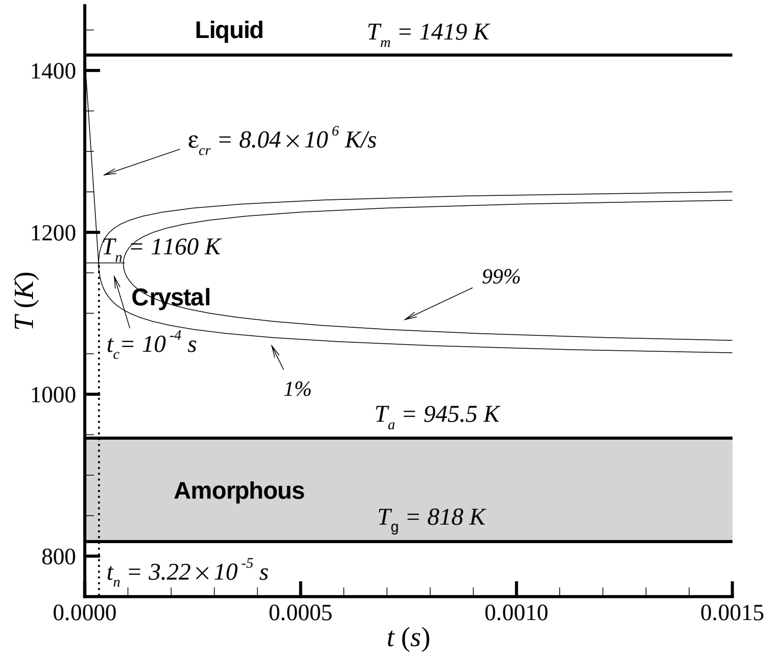

Figure 7.2 The TTT Diagram for Fe_{75}-Si_{10}-B_{15}

The critical cooling rate $\varepsilon_{cr} = (T_m - T_n)/t_n = 8.04 \times 10^6\ K/s$, and the nucleation temperature $T_n = 1160\ K$ from Figure 7.2. This ε_{cr} is consistent with the one obtained using Eq. (7.4) (see Table 7.4) in order of magnitude. Figures 7.2 and 7.3 also present the 99% fraction of crystal. If the cooling rate in rapid solidification is lower than the critical cooling rate, the crystallization may occur at a temperature higher than the nucleation temperature. But below the nucleation temperature, a lower cooling rate is allowed.

At the nucleation temperature the crystal grows very rapidly in $10^{-4}\ s$ to reach 99% crystallization once the nucleation is activated. The time period between the TTT curves is larger if temperature is below or above T_n. Henceforth, we symbolize the minimum time period of crystallization at the nucleation temperature T_n by t_c, namely the time interval between two nose points of the C-shaped curves as shown in Figure 7.2.

The nucleation temperature T_n estimated by Eq. (7.5) is 100 K higher than the mini-

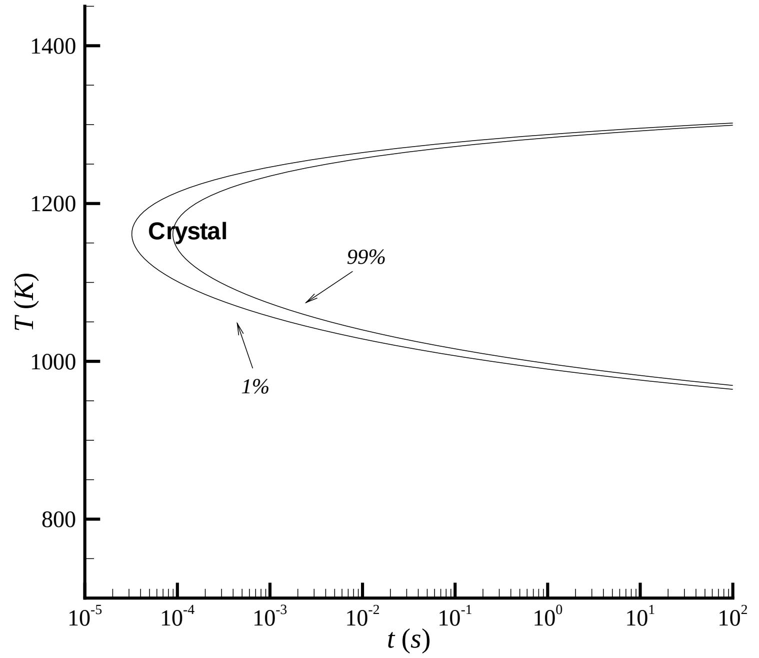

Figure 7.3 The TTT Diagram for Fe_{75}-Si_{10}-B_{15} (Time in Log scale)

mum one obtained by Eq. (7.4). The discrepancy is ascribed to the different computation of control volume or area chosen in the methods and the augment of magnitude being applied for the cooling rate in the first method. The predicted critical cooling rates, 10^6 K/s and 8×10^6 K/s, agree with Kramer's experimental result 5×10^6 K/s[5].

7.3 Melt Spinning Process

Henceforward, in our illustrations of melt spinning, the wheel rotates clockwise and the ribbon is spun out to the right, the conventional positive direction of x-axis (see Figure 1.1).

Unlike planar flow casting, in free-jet melt spinning a molten metallic stream under a certain pressure travels some distance before it impinges on a highly spinning wheel at some velocity. According to Kramer's observation[5], a molten flow in free-jet melt spinning experiences three distinct sections: free-stream, wheel-contact, and free-flight, as shown in Figure 7.4. In the free-stream section, the stream shape remains unchanged;

however, in the leading side (see **DC** in Figure 7.4), the spinning wheel may accelerate the flow. In the wheel-contact section, the quench wheel undercools the melt alloy by conduction so that the melt viscosity increases exponentially. In the third section, the ribbon departs the wheel and amorphous alloy forms mainly due to radiation and convection with the ambient gas.

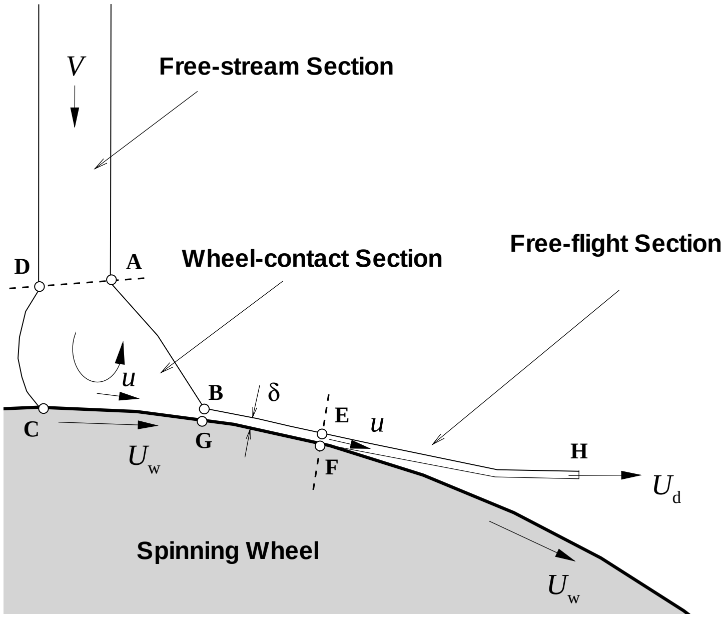

Figure 7.4 Three sections in a steady melt spinning process

The previous researchers unanimously presumed that the molten jet upstream is the leading convex meniscus (**DC**) and the downstream is located on the other side (**AB**), as shown in Figure 7.4[2, 34–36]. We determine the upstream or downstream of a flow according to the relative motion between the flow and its body of reference. If the body of reference is faster than the flow when they both move in a direction, the upstream is in the direction toward which they move. In the region of melt-wheel boundary, the rotating wheel is selected to be the reference frame more precisely than the nozzle. If the wheel speed U_w is greater than the flow speed u next to the moving wheel, the upstream is where the ribbon is delivered, i.e., point **H** relative to point **C**. In all melt spinning processes, we have $U_\mathrm{w} \gg u$ in the melt pool and $U_\mathrm{w} \geqslant u$ in the ribbon, although we may find more scenarios where $U_\mathrm{w} < u$, like ground water streams formed by falling rain. Apparently, the nozzle where the molten jet is released is also upstream. The upstream, midstream, and downstream are so indicated in Figure 7.5.

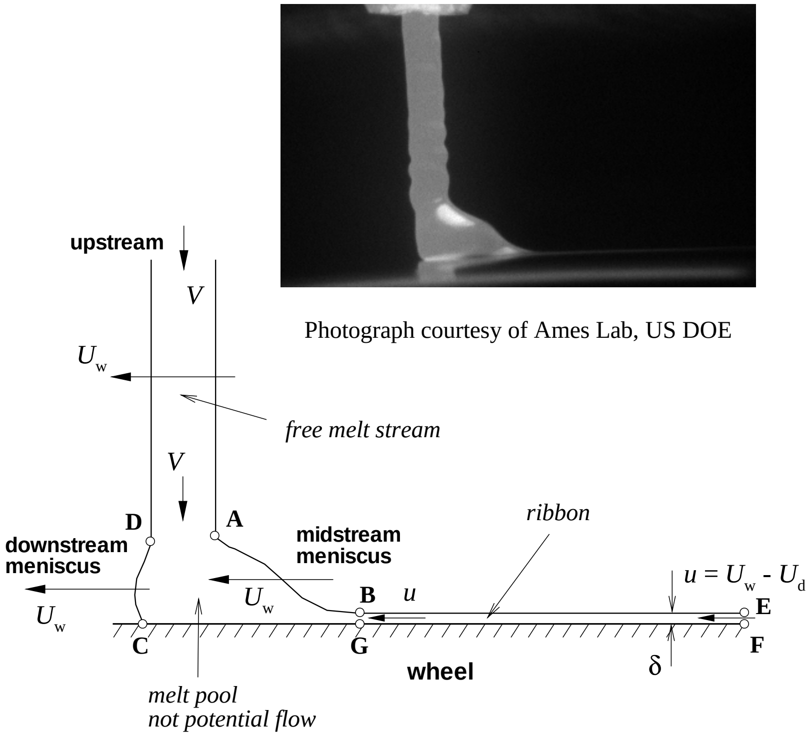

Photograph courtesy of Ames Lab, US DOE

Figure 7.5 A steady-state melt spinning (not to scale)

The Eulerian methodology is commonly used in fluid mechanics and CFD. In Figure 7.5, if the Eulerian system is fixed to the wheel, the wheel remains motionless in the system. The molten stream moves at U_{w} and the ribbon moves at u to the left. The ribbon forms under surface tension, viscous force, and very fast flow motion of the melt relative to the wheel. The molten flow is cooled by the quench wheel; the flow temperature near point **F** is lower than those points near wheel surface left of **F**, for instance, **C** and **G** as shown in Figure 7.5. Amorphorization (undercooling) begins at the end of ribbon, point **H** in Figure 7.4, whereas melt particles initially cool near point **C** and then move to the ribbon from the Lagrangian viewpoint. Accordingly, the flow within the ribbon comes from the direction of the ribbon end **H** (see Figure 7.4) where the melt has cooled earliest. The ribbon top surface is cooled through heat transfer, not only by the chamber gas but also by the incident 'cooler' flow from **EF** if the ribbon is still in liqidus state..

7.4 Dynamical Similarity in Free-Jet Melt Spinning

The melt spinning is a 3D problem because the orifice is circular, whereas the ribbon can be regarded as a 2D flow from the lateral direction. Supposing that ribbon is steadily produced at an average delivery velocity U_d, also called *casting rate*, from the mass conservation, the ribbon thickness δ is:

$$\frac{\delta}{Z} = \frac{\pi}{4}\left(\frac{Z}{w}\right)\left(\frac{\bar{V}}{U_\mathrm{d}}\right), \tag{7.6}$$

where $\bar{V}$ is the average ejection velocity at the nozzle, Z the orifice diameter, and w the ribbon width as shown in Figure 7.6.

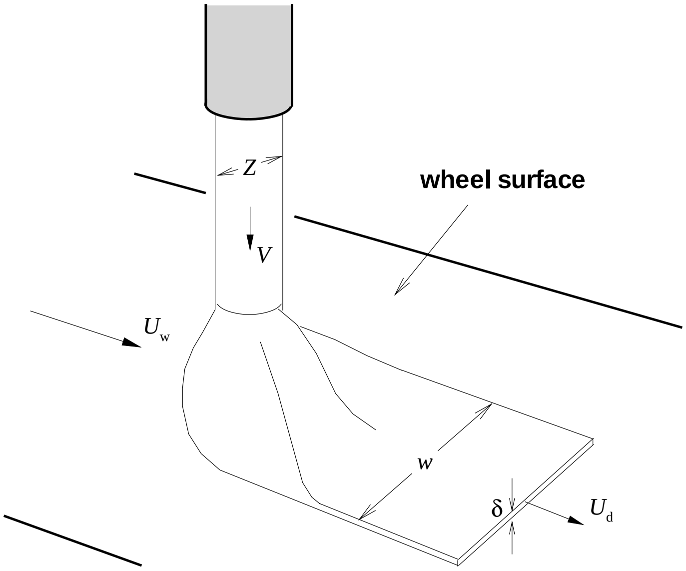

Figure 7.6 Illustration of a ribbon formation on a spinning wheel

U_w (cm/s)	500	600	700	750	800	900	1000	2000	3000	4000
Z/w	.2376	.1980	.1398	.1064	.0868	.0720	.0604	.0524	.0469	.0448
$\pi Z/4w$	.1866	.1555	.1098	.0836	.0682	.0565	.0474	.0411	.0368	.0352

Table 7.5 Ratio of orifice diameter to ribbon width

Unlike ribbon thickness, the ratio Z/w exhibits less variability among multiple runs or within one run for each wheel speed as listed in Table 7.5 and Figure 7.7 from [5].

Z/w decreases with increasing wheel speed, but the magnitudes of decrease are lower at wheel speeds larger than 10 m/s, a knee point as shown in Figure 7.7. It is impossible to estimate ribbon thickness from Eq. (7.6), because Z/w and U_d are both unknown.

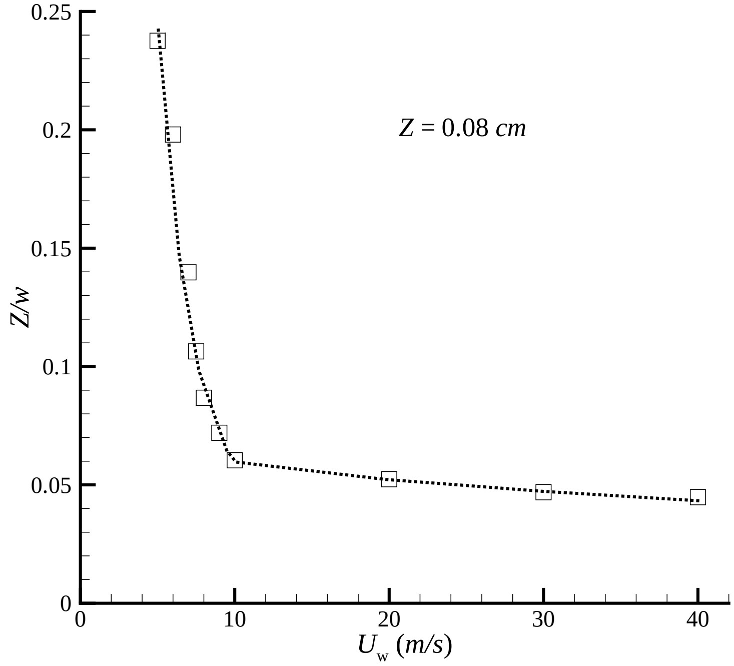

Figure 7.7 Ratio Z/w as a function of wheel speed

The ratio $(\pi/4)(Z/w)$ can be seen as a transformation factor between the 3D free jet and 2D ribbon formation in the study of free-jet melt spinning. If we choose a smaller ejection velocity

$$\bar{V}' = \frac{\pi}{4}\left(\frac{Z}{w}\right)\bar{V} \quad \text{such that} \quad \frac{\delta}{Z} = \frac{\bar{V}'}{U_\mathrm{d}}, \tag{7.7}$$

or a larger delivery velocity

$$U_\mathrm{d}' = U_\mathrm{d} \Big/ \frac{\pi}{4}\left(\frac{Z}{w}\right) \quad \text{such that} \quad \frac{\delta}{Z} = \frac{\bar{V}}{U_\mathrm{d}'}, \tag{7.8}$$

a 3D free-jet melt spinning seems to be successfully converted to a 2D flow problem; however, they are not economical in simulation. Smaller $\bar{V}'$ (see Eq. (7.7)) results in longer computation time for the jet traveling the gap, which is not to our benefit. Larger U_d' (see Eq. (7.8)) as well as larger U_w' may lead to numerical difficulty. Here we assume

U_{d} is proportional or equal to U_{w}. The viscosity μ is thus modified with the factor $(\pi/4)(Z/w)$ to keep the U'_{w}-based Reynolds number in the 2D simulation equal to the U_{w}-based Reynolds number of the 3D process. The modified viscosity μ' is given from:

$$\mathbf{Re} = \frac{U'_{\mathrm{w}}\delta\rho}{\mu} = \frac{U_{\mathrm{w}}\delta\rho}{\dfrac{\pi}{4}\left(\dfrac{\delta}{w}\right)\mu} = \frac{U_{\mathrm{w}}\delta\rho}{\mu'}, \tag{7.9}$$

where

$$U'_{\mathrm{w}} = U_{\mathrm{w}} \Big/ \frac{\pi}{4}\left(\frac{Z}{w}\right) \qquad \text{and} \qquad \mu' = \frac{\pi}{4}\left(\frac{Z}{w}\right)\mu. \tag{7.10}$$

From Table 7.5 or Figure 7.7, the factor $(\pi/4)(Z/w)$ is of $\mathcal{O}(10^{-2})$ in order of magnitude when $1000 \leqslant U_{\mathrm{w}} \leqslant 4000$ *cm/s*. The viscosity is thus decreased by 10^2 as in Eq. (7.11) from Eq. (7.3). For $U_{\mathrm{w}} < 1000$ *cm/s*, the decreased viscosity of Eq. (7.11) is used in the 2D simulation for simplicity, although the factor is found $\mathcal{O}(10^{-1})$ as shown in Table 7.5. The decreased viscosity is beneficial because the exponential increases in viscosity with temperature drops require smaller time step in the simulation.

7.5 Simulation of Jet Impingement on Wheel

A 2D numerical simulation of melt spinning is performed on a physical domain of $2\ cm \times 0.4\ cm$ as shown in Figure 7.8. The ejection velocity V, orifice diameter Z, gap height G, and wheel speed U_{w} are the design parameters for a typical melt spinning. The ejection velocity of the molten jet V instead of the initial pressure is imposed in parabolic distribution at the nozzle. Then we have the average ejection velocity $\bar{V} = 2/3V$. Consistent with the experiments in [49] and [5], Z and G are chosen 0.08 *cm* and 0.4 *cm*, respectively, in the simulation. Because the radius of the wheel 12.5 *cm* is larger than the gap height G, the wheel surface is assumed to be a plane.

V (cm/s)	$\bar{V}$ (cm/s)	**Re**	**Ca**	**Web**
195	130	2.7486×10^4	3.033×10^{-4}	8.3373

Table 7.6 Dimensionless numbers based on $\bar{V}$ and Z at the nozzle

Physical properties of the alloy are given in Figure 7.8. The alloy density and surface tension coefficient are both constant. The temperature-dependent viscosity of the jet is calculated according to Eq. (7.3) and the dynamical similarity (refer to Section 7.4) in

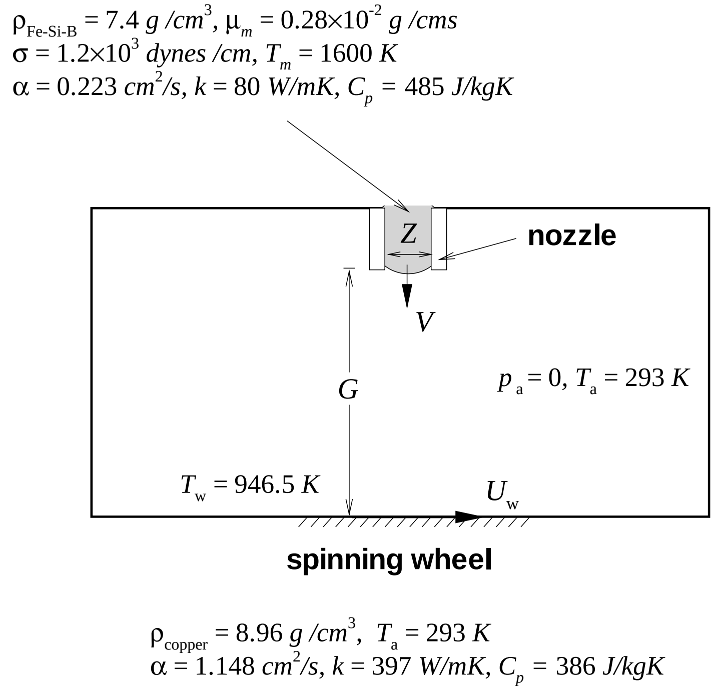

Figure 7.8 Melt spinning chamber

the *g-cm-s* unit system as follows:

$$\mu = 6.374 \times 10^{-6} \exp\left(\frac{3.35 \times 1419}{T - 818}\right) \qquad g/cms, \tag{7.11}$$

also shown in Figure 7.9 in exponential scale. For simplicity, the superscript prime is ignored in Eq. (7.11). Accordingly, we have viscosity $\mu_m = 0.0028\ g/cms$ at the melting point $T_m = 1600\ K$, and $\mu = 0.01736\ g/cms$ at the lower limit of melting point $T_m = 1419\ K$.

The indoor temperature 293 K is chosen as the ambient temperature T_{a} as well as the wheel center temperature T_{wheel}. They all remain constant in the simulation. The melt-wheel temperature T_{w} is the average value of T_m and T_{a} because heat transfer near the melt-wheel boundary is mainly thermal conduction. That is discussed in Sections 7.7 and 7.8. Unlike μ, the thermal diffusivity of the molten alloy α is assumed to remain constant in the melt pool.

According to Figure 7.9, at the nucleation temperature the viscosity is about 2500 times that at the melting temperature and it increases exponentially while the temper-

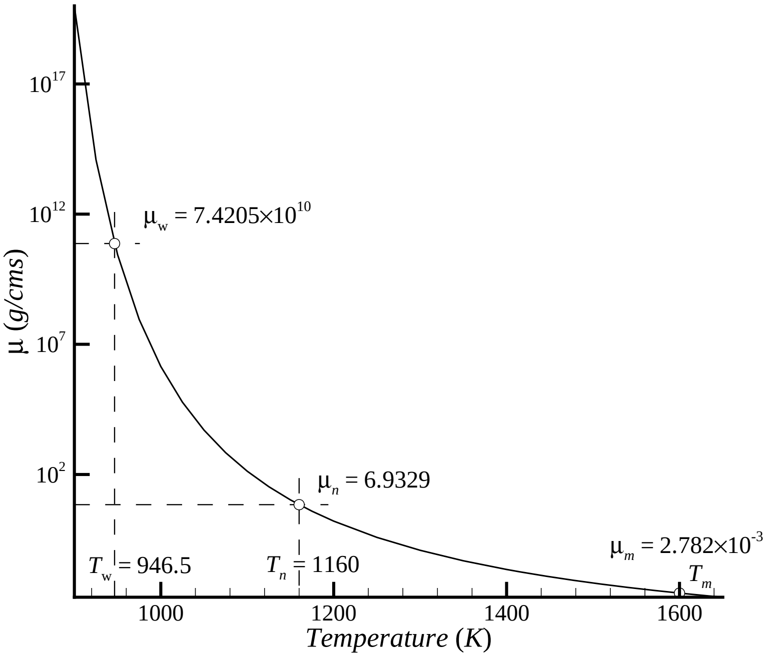

Figure 7.9 Viscosity of Fe_{75}-Si_{10}-B_{15} in the Vogel-Fulcher-Tammann form

ature drops to T_{w}. The tremendous viscosity often leads to numerical failure in the melt spinning simulation. In addition, higher wheel speed requires smaller time step. The larger viscosity and the higher wheel speeds significantly complicate the simulation (see Section 3.6 of Chapter 3), despite the scaling-up of equations as introduced in Section 5.6 of Chapter 5. The program is modified using Eq. (7.11), namely the exponential temperature-viscosity relation for simulating the thermal transport, as shown in Figure 7.14. But to investigate the evolution and dynamical characteristics of the melt pool as in Figures 7.12 and 7.13, the viscosity near the wheel surface is assumed to increase linearly to an acceptable extent with temperature decreases and U_{w} is chosen 200, 400, and 1000 cm/s for comparison.

Grid sensitivity analysis is made at $U_{\mathrm{w}} = 400$ cm/s and $t = 3.25$ ms as seen in Figure 7.10. Grid resolutions of 400×80 and 500×100 are found to yield a convergent ribbon thickness and a convergent melt pool shape. Hence, δx and δy are both chosen 0.005 cm to generate 400×80 meshes in the simulation.

By means of induced electrical currents, the alloy is heated to liquid by the coils

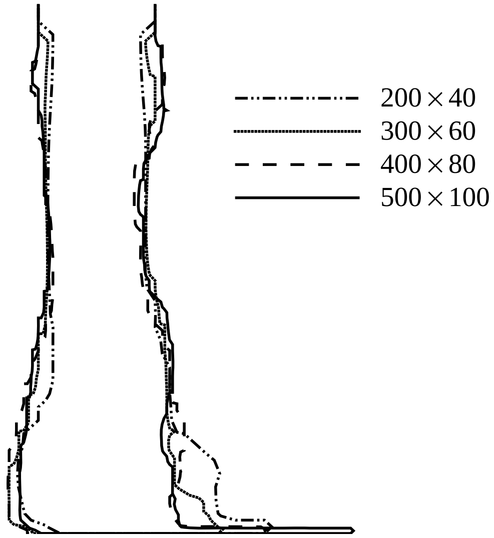

Figure 7.10 Melt pool and ribbon evolution on various grid resolutions, $U_{\mathrm{w}} = 400\ cm/s$ and $t = 3.25\ ms$

ouside the crucible. Once it is released from the crucible at initial ejection velocity 130 cm/s, in about 3.225×10^{-3} s, the molten free jet impinges on the rotating wheel, as shown in Figures 7.11 to 7.13. As seen in these figures, the configurations of molten stream are not smooth because the H-N algorithm employs a stair-stepped approximation of free surface. In the simulation of the free jet traveling, Eq. (7.3) is chosen as the viscosity at temperature 1600 K, namely 0.2782 g/cms because before impinging on the wheel the axisymmetric molten flow has no contact with the wheel and no heat radiation to vacuum.

From Figure 7.13, we find the flow in free stream accelerates at the leading side and decelerates at the other side due to wheel rotation. The molten alloy flow in the pool begins to roll counter-clockwise after the jet contacts the clockwise rotating wheel in the simulation. A flow circulation forms within the pool because $U_{\mathrm{w}} \gg V$ in a typical melt spinning (see Figure. 7.13). Stronger but smaller circulations are visible under higher wheel speeds. The melt pool bulges along **AB** as a result of the circulation. Near the nozzle, the jet also bulges because the imposed velocity V is not uniform distributed at the nozzle. The geometry of a melt pool is larger in size under lower wheel speeds, as

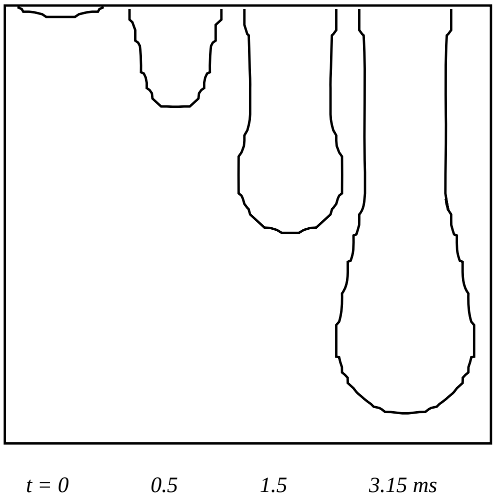

Figure 7.11 Free melt jet evolution before touchdown

shown in Figure 7.13 (also see [5, 49]). Thinner and longer ribbon is spun out under higher wheel speeds, while those particles away from the wheel are expelled from the ribbon. The flow velocity on the ribbon top is less than U_{w}; consequently, the delivery velocity U_{d} is less than the U_{w}. In order to deliver an amorphous ribbon, the wheel speed must be larger than a certain value to enable a circulation, under which the not-undercooled alloy particles merge with the particles from the crucible to prevent the crystallization from occurring within the pool.

Figure 7.14 shows temperature and velocity distribution within the melt pool under wheel speeds of 400 and 800 cm/s, and subject to the melt-wheel temperature $T_{\mathrm{w}} = 946.5\ K$. The temperature-dependent viscosity of the alloy follows Eq. (7.11) in the simulation of Figure 7.14. In addition to thermal diffusion, thermal convection and viscous dissipation are considered in the 2D simulation of momentum and thermal transport.

From the figures, the isotherms are approximately parallel to the wheel surface. The isotherm of 1600 K quickly moves up soon after the jet touches down the quench wheel. The region of the molten alloy jet next to the wheel is thus rapidly cooled. Nucleation layers of $T_n = 1160\ K$ develop from the melt-wheel boundary toward the melt pool with time. Unlike the isotherms predicted using the 1D thermal diffusion model in Section 7.7, the isotherms of melting and nucleation temperatures are away from the wheel surface,

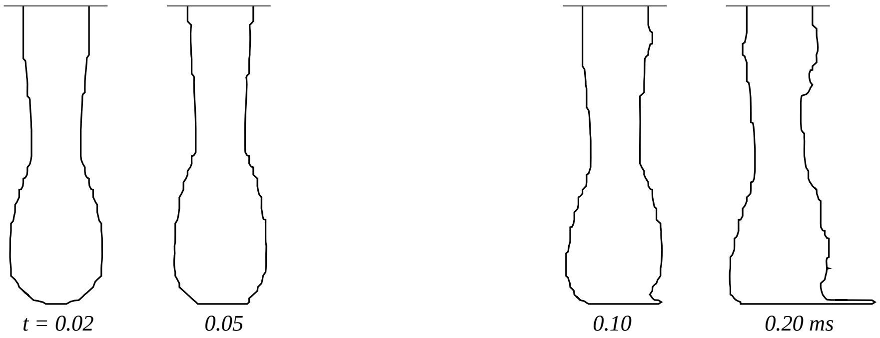

(a) $U_{\rm w} = 400\ cm/s$

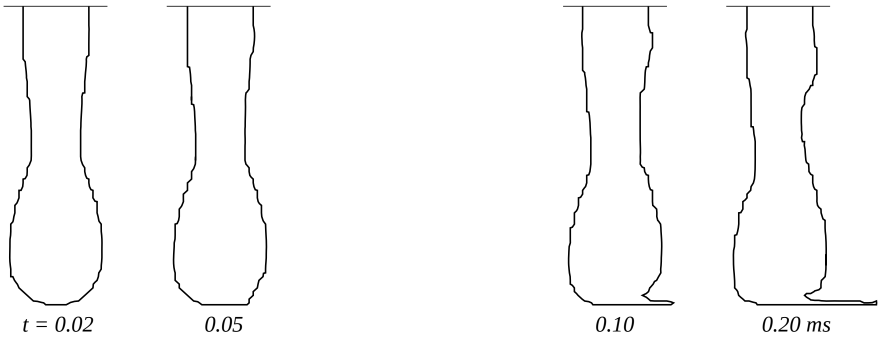

(b) $U_{\rm w} = 1000\ cm/s$

Figure 7.12 Melt pool and ribbon evolution

not starting at point **C**. Notice that at $t = 0.15\ ms$ the molten flow circulates near the pool-ribbon conjunction at $U_{\rm w} = 800\ cm/s$, as shown in Figure 7.14(d). The little flow circulations near the pool-ribbon conjunction play an important role as a filter that blocks not-undercooled particles from entering the ribbon.

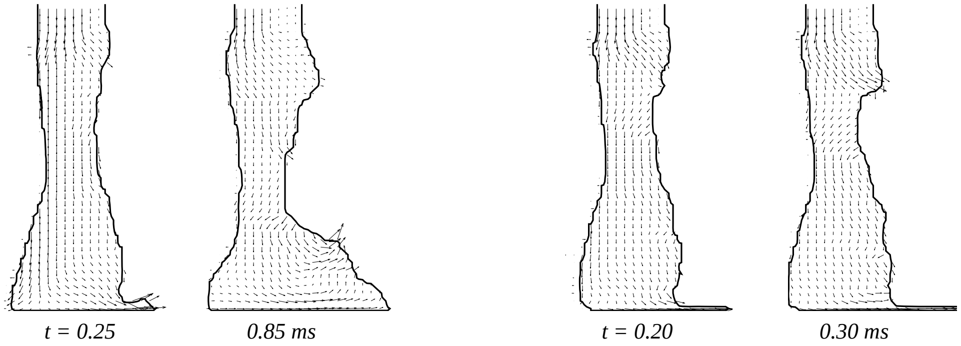

(a) $U_{\mathrm{w}} = 200\ cm/s$

(b) $U_{\mathrm{w}} = 400\ cm/s$

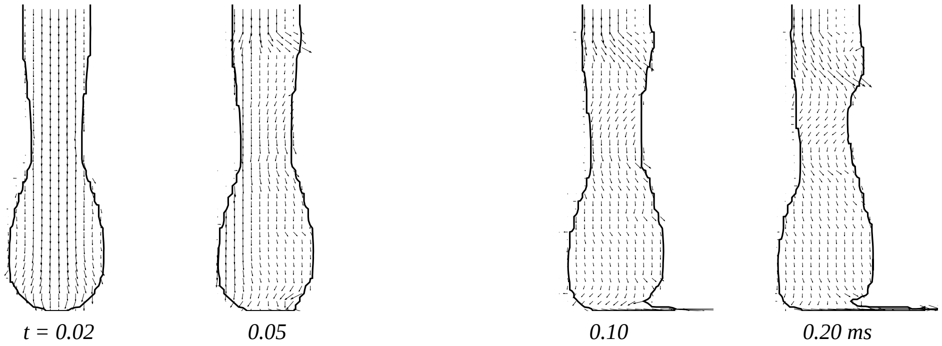

(c) $U_{\mathrm{w}} = 1000\ cm/s$

Figure 7.13 Flow velocity vectors within melt pool

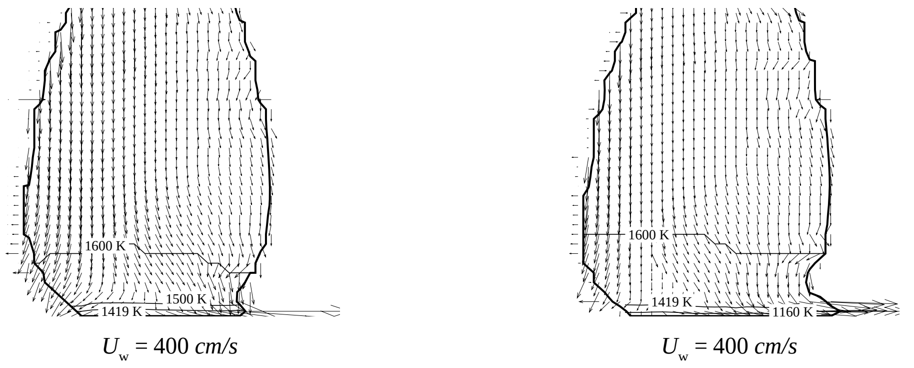

(a) 0.10 *ms* after touchdown (b) 0.15 *ms* after touchdown

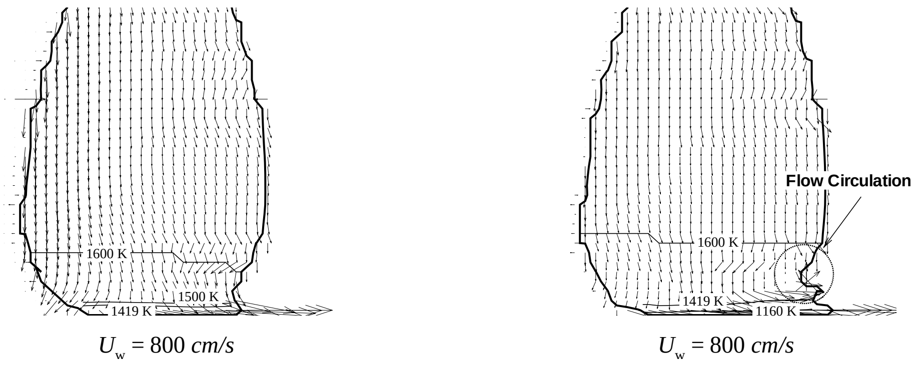

(c) 0.10 *ms* after touchdown (d) 0.15 *ms* after touchdown

Figure 7.14 Isotherm and velocity in melt pool

7.6 Estimate of Jet Ribbon Thickness

For free-jet melt spinning, ribbon thickness is reported as proportional to ${U_\mathrm{w}}^{-1/2}$[32] or U_w^{-1}[5, 33]. Kramer et al gave a best-fit ribbon thickness estimate associated with boundary layer thickness and experiment measurements[5]. The ribbon thickness varies within one run and across multiple runs, as reported in [49] and [5]. The scatter of the measured ribbon thickness reflects its dependence on various physical or process parameters.

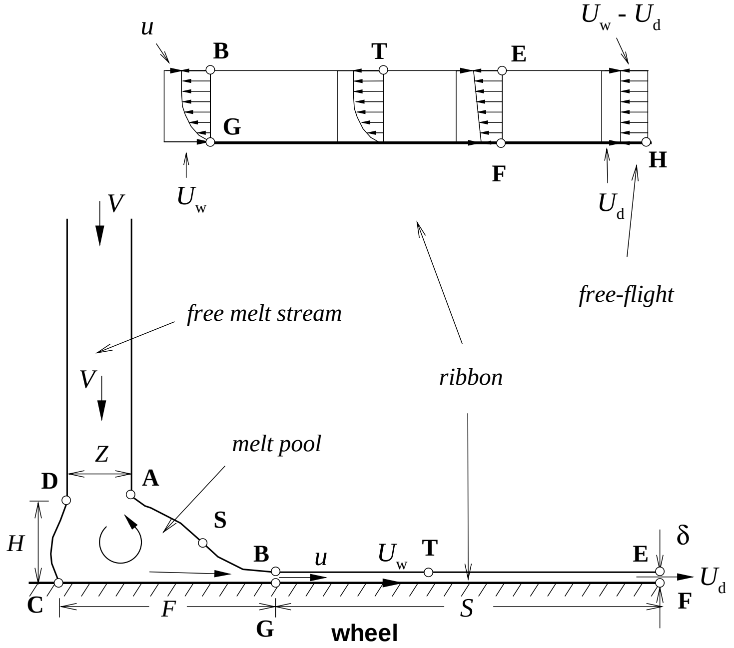

Figure 7.15 Melt spinning geometry estimates (not to scale)

As demonstrated in Figure 7.15, the spinning wheel casts the ribbon through friction force. The momentum flux of molten flow at the cross-section **BG** is equal to the average momentum the wheel exerts to the melt pool over the contact section **CG**. The ribbon is dragged by viscous friction in the form of a momentum layer; not a boundary layer and a displacement layer. If the molten stream has a complete contact with the wheel with no gas entrapped between them, ribbon thickness is established from Blasius' flat plate friction coefficient or momentum thickness[92–94] as follows:

$$\frac{\delta}{Z} = 0.664 \left[\left(\frac{S+F}{Z} \right) \mathbf{Re}_{S+F}^{-1/2} - \left(\frac{S}{Z} \right) \mathbf{Re}_{S}^{-1/2} \right], \tag{7.12}$$

where the Reynolds number is computed based on velocity $U_{\mathrm{w}} - u$ and wet distance ($S + F$ or S). u is the flow velocity next to the wheel (see Figure 7.15). When $U_{\mathrm{w}} \gg u$, the velocity in Reynolds number is U_{w}. The viscosity in Reynolds number varies with local temperature. For simplicity, we can either choose the viscosity at point **B** or the average viscosities over the wet distances $S + F$ and S for the Reynolds numbers, respectively. The friction is calculated from the detachment point **F** rather than the leading point **C**. Eq. (7.12) is valid only when the surface flow along **AB** is stagnant at point **B** (see Section 7.5).

It is not easy to predict ribbon thickness only using Eq. (7.12) but we have two simplified equations as follows:

$$\frac{\delta}{Z} = \frac{0.275\left(\frac{F}{Z}\right)}{\sqrt{\mathbf{Re}_{Z,U_{\mathrm{w}},\mu_{\mathbf{B}}}\left(1-\frac{U_{\mathbf{B}}}{U_{\mathrm{w}}}\right)\left(\frac{S}{Z}\right)}} \qquad \text{if} \quad S = F, \tag{7.13}$$

and

$$\frac{\delta}{Z} = \frac{0.332\left(\frac{F}{Z}\right)}{\sqrt{\mathbf{Re}_{Z,U_{\mathrm{w}},\mu_{\mathbf{B}}}\left(1-\frac{U_{\mathbf{B}}}{U_{\mathrm{w}}}\right)\left(\frac{S}{Z}\right)}} \qquad \text{if} \quad S \gg F, \tag{7.14}$$

where the Reynolds number **Re** is calculated on orifice diameter Z, wheel speed U_{w}, and viscosity at point **B**. The prefactors such as in Eqs. (7.13) and (7.14) should fall between 0.274 and 0.332 for $S > F$. In the derivation of Eq. (7.14) from (7.12) the following approximate algebraic identity is implemented:

$$\sqrt{S+F} - \sqrt{S} \approx \frac{F}{2\sqrt{S}} \qquad \text{if} \quad S \gg F. \tag{7.15}$$

As shown in Eqs. (7.13) and (7.14), ribbon thickness is proportional to melt pool length. Eqs. (7.12) to (7.14) show the variability of the melt ribbon in thickness. Ribbon thickness is not a single-value function of wheel speed but depends on flow temperature and the wheel wetting distance of the melt as well. Thinner ribbons may result if the ribbons reside longer on the wheel. Ribbon thickness increases greatly with decreasing wheel speed.

We have $S/Z = 14.815$ ($S = 1.2\ cm$ for $U_{\mathrm{w}} = 2000\ cm/s$ and $Z = 0.081\ cm$) from [5], and assume $u \ll U_{\mathrm{w}}$ at point **B**, such that Eq. (7.14) reduces to

$$\frac{\delta}{Z} = \frac{0.2343}{\sqrt{\mathbf{Re}}} \quad \text{and} \quad \frac{\delta}{Z} = \frac{0.2130}{\sqrt{\mathbf{Re}}} \tag{7.16}$$

for $U_{\mathrm{w}} = 1500$ and $2000\ cm/s$, with $F/Z = 2.716$ and 2.4691, respectively. Ribbon thickness is plotted according to Eq. (7.16) for two wheel speeds 1500 and 2000 cm/s with the experimental observation from [5] (also refer to Table 7.9).

Re = 10.7272 and 14.3029 in Figure 7.16 respectively correspond to the wheel speeds. Using Eq. (7.11), the viscosity 83.815 g/cms in Reynolds number is computed at the convergent temperature 1108 K for both wheel speeds, quoted from Kramer[5].

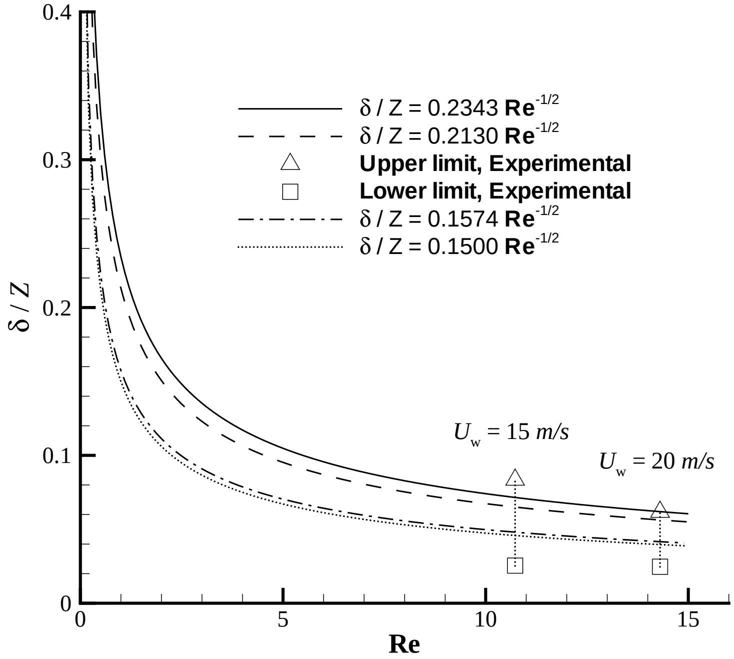

Figure 7.16 Ribbon thickness as a function of Reynolds number

Apparently, from Figure 7.16, the estimates of ribbon thickness are close to the upper limit of the measurements. The reason lies in that the viscosity at point **B** is higher for the whole wetting contact.

If Karman's integral form of boundary-layer equations[94],

$$\delta = \frac{1}{\rho U_\infty^2} \int_0^F \tau_{\mathrm{w}} dx = 0.332 \int_0^F \frac{dx}{\mathbf{Re}_x^{1/2}}, \tag{7.17}$$

is applied in the calculation, using the viscosity at the nucleation temperature 1160 K in the Reynolds number, we have

$$\frac{\delta}{Z} = \frac{0.332}{\sqrt{\mathbf{Re}}} \sqrt{\frac{F}{Z}} \sqrt{\frac{\mu_{1160\ K}}{\mu_{\mathbf{B}}}}, \tag{7.18}$$

where **Re** is consistently calculated on orifice diameter Z, wheel speed U_{w}, and viscosity at point **B**. In Eq. (7.17) if $S \gg F$, $\mathbf{Re}_x$ is approximated as a constant based on F and the viscosity at the nucleation temperature 1160 K. Again, for $U_{\mathrm{w}} = 1500$ and 2000 cm/s, with $F/Z = 2.716$ and 2.4691, respectively, the estimates of ribbon thickness are given,

$$\frac{\delta}{Z} = \frac{0.1574}{\sqrt{\mathbf{Re}}} \quad \text{and} \quad \frac{\delta}{Z} = \frac{0.1500}{\sqrt{\mathbf{Re}}}. \tag{7.19}$$

As shown in Figure 7.16, the thickness estimates given by Eq. (7.19) are closer to the lower limits of the experimental results.

7.7 Thermal Analysis of the Melt Spinning Process

Near the wheel where nucleation is activated, those crystalline particles and the molten particles with temperature higher than T_n are lifted by the flow circulation and pushed by the midstream meniscus. Then the particles rejoin the melt flow; their temperature rises to the melting point by momentum and thermal transport in the melt pool. Large friction force due to high relative motion and lower temperature on the melt-wheel contact provides enough upward momentum to form the circulation in the melt pool, along with strong surface tension by the midstream meniscus (see Figure 7.13). The melt pool actually acts as a heat exchanger where those not-undercooled and crystalline particles are re-melted to liquidus state. Temperature of the molten alloy in the crucible should be higher enough to suppress the nucleation in the circulation.

According to Figure 7.2, the cooling rate of the alloy melt needn't be greater than the critical cooling rate for an alloy particle having $T < T_n$. But in the first time period $t_n = 3.22 \times 10^{-5}$ s after the melt touches down the wheel, the temperature should drop 440 K from the melting point T_m (1600 K) to the predicted nucleation temperature T_n (1160 K). Only in this period, the melt cooling rate must be greater than the critical cooling rate.

From the critical cooling rate, we have the requirement of temperature variation along the x-direction near the melt-wheel boundary (refer to Figure 7.17):

$$-\frac{\partial T}{\partial x} \geqslant \frac{\varepsilon_{cr}}{U_{\mathrm{w}}}, \tag{7.20}$$

where the negative sign is present since ε_{cr} is defined as a positive value (temperature drop over time). Eq. (7.20) shows that a faster wheel speed lowers the temperature gradient requirement.

The ribbon should be thinner than the nucleation layer δ_n, within which the alloy flow is undercooled below the nucleation temperature such that

$$T \leqslant T_n \quad \text{at point } \mathbf{B}, \tag{7.21}$$

as shown in Figure 7.17. The hollow arrows in the figure indicates the heat flow direction.

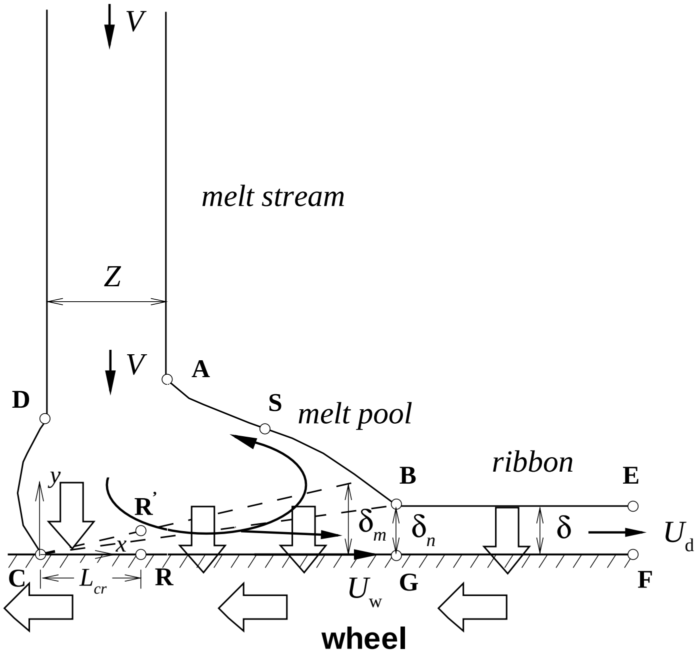

Figure 7.17 Momentum and thermal transport in the melt pool

A stable nucleation layer δ_n formed from point **C** along the wheel surface is vital to the amorphous alloy formation. Poor heat conduction between the chill wheel and the molten alloy due to gas entrapment allows an unstable thinner nucleation layer δ_n with many not-undercooled particles. It is supported by the experimental observation that the entrapment of gas pockets at the wheel-side surface results in a crystalline phase in the ribbon[49]. When the ribbon departs the wheel, the temperature should be less than T_n. Amorphous alloy is mainly observed in the free-flight period from Kramer's experiments in [5], whereas some crystals grow from the ribbon bottom surface and are quenched half way to the top surface if the roller speed is less than a certain value, according to [37].

We can determine the wheel speed limits from the thermal analysis in Section 7.9:

$$\frac{Z}{0.6061 t_n + t_c} \leqslant U_{\mathrm{w}} \leqslant \frac{F}{0.6061 t_n}, \tag{7.22}$$

where $t_c = 10^{-4}\ s$ and $t_n = 3.22 \times 10^{-5}\ s$ from Figure 7.2. Eq. (7.22) requires that the wheel speed be low enough for the midstream meniscus to wipe all the not-undercooled melt particles out of the ribbon, but large enough such that the upstream jet from the crucible is not influenced by crystallization.

The minimum wheel speed is 678 *cm/s* for the amorphous alloy formation if $Z = 0.081$ *cm*. Conversely, given wheel speed U_{w}, we can determine the orifice size Z from Eq. (7.22). It is complicated to determine the upper wheel speed limit according to Eq. (7.22), because F is larger at a lower wheel speed than at a higher wheel speed.

7.8 Analytical Solutions of Thermal Layers

It is reasonable to ignore the convection terms of flow and wheel rotation in the melt-wheel contact region because the flow soon solidifies as temperature drops. If we ignore the viscous dissipation terms in Eq. (4.2) and assume no latent heat is liberated in the melt pool (because undercooling is a non-equilibrium solidification), we have a 1D heat diffusion equation along the y-direction for the alloy melt flow (see Figure 7.17):

$$\frac{\partial T}{\partial t} = \alpha \frac{\partial^2 T}{\partial y^2}, \tag{7.23}$$

where α is thermal diffusivity of Fe_{75}-Si_{10}-B_{15} alloy, and the subscript 'alloy' is ignored for simplicity. The equation is subject to constant boundary conditions

$$T(G, t) = T_m, \quad \text{and} \quad T\left[-\frac{D_{\mathrm{w}}}{2}\left(\frac{\alpha_{\mathrm{alloy}}}{\alpha_{\mathrm{copper}}}\right)^{1/2}, t\right] = T_{\mathrm{a}}, \tag{7.24}$$

and initial conditions

$$T(y, 0) = T_m \ \text{ at } \ y \geqslant 0 \qquad \text{and} \qquad T(y, 0) = T_{\mathrm{a}} \ \text{ at } \ y < 0, \tag{7.25}$$

where G is distance between the downside of nozzle and the upside of wheel, D_{w} is wheel diameter, and α_{alloy} and α_{copper} are the thermal diffusivity of Fe_{75}-Si_{10}-B_{15} alloy and copper, respectively, as shown in Table 7.7. Notice in Eq. (7.24) the y coordinate in the copper wheel ($y < 0$) has been transformed via the thermal diffusivity ratio. The wheel diffusivity changes to the alloy diffusivity, so that Eq. (7.23) is applicable to the copper wheel.

If the following semi-infinite criterion is satisfied:

$$\frac{G}{2\sqrt{\alpha t}} \geqslant 2, \tag{7.26}$$

the constant boundary condition at $y = 0$ is halfway between the two initial conditions, i.e.,

$$T(0, t) = T_{\mathrm{w}} = (T_m + T_{\mathrm{a}})/2. \tag{7.27}$$

	$\alpha\ (cm^2/s)$	$k\ (W/mK)$	$\rho\ (g/cm^3)$	$C_p\ (J/kgK)$
Copper	1.148	397	8.96	386
Alloy	.2229	80	7.5	485

Table 7.7 Thermal diffusivity, conductivity, density, and heat specific

The solution to Eq. (7.23) subject to the initial and boundary conditions of Eqs. (7.25) and (7.27) is:

$$T^* = \frac{T - T_m}{T_\mathrm{w} - T_m} = \mathrm{erfc}\left(\frac{y}{2\sqrt{\alpha t}}\right) = \mathrm{erfc}\left[\frac{\sqrt{\mathbf{Pe}}}{2}\left(\frac{y}{Z}\right)\left(\frac{x}{Z}\right)^{-1/2}\right], \tag{7.28}$$

where the origin point $x = 0$, $y = 0$ is located at the leading point **C** (see Figure 7.17), time $t = x/U_\mathrm{w}$, and the Peclet number $\mathbf{Pe} = ZU_\mathrm{w}/\alpha$ as listed in Table 7.8. Temperature profile is plotted in Figure 7.18 using Eq. (7.28).

$U_\mathrm{w}\ (cm/s)$	500	750	850	1000	1250	1500	2000	4000
Pe	181.61	272.42	308.74	363.23	454.04	544.84	726.46	1452.91

Table 7.8 Peclet numbers based on U_w and Z

The alloy is melted up to 1600 K in the crucible and the wheel surface temperature $T_\mathrm{w} = 946.5\ K$, halfway of $T_\mathrm{a} = 293\ K$ and $T_m = 1600\ K$. $T^* = 1$, 0.6733 and 0, respectively, correspond to $T_\mathrm{w} = 946.5\ K$, $T_n = 1160\ K$, and $T_m = 1600\ K$. The thickness of the thermal layer of T_n is derived from Eq. (7.28):

$$\frac{\delta_n}{Z} = \frac{0.5963}{\sqrt{\mathbf{Pe}}}\sqrt{\frac{x}{Z}} \tag{7.29}$$

as shown in Figure 7.18, and so is the thickness of the thermal layer of $T_m = 1600\ K$:

$$\frac{\delta_m}{Z} = \frac{4}{\sqrt{\mathbf{Pe}}}\sqrt{\frac{x}{Z}}. \tag{7.30}$$

Thermal layers δ_n and δ_m are depicted in Figure 7.17.

The third thermal layer of $T = 1419\ K$ is the lower limit of the alloy melting temperature:

$$\frac{\delta_{1419\ K}}{Z} = \frac{1.5374}{\sqrt{\mathbf{Pe}}}\sqrt{\frac{x}{Z}}. \tag{7.31}$$

The temperature profiles measured in [5, 37] exhibit a similar distribution. They are plotted in dimensionless temperature as shown in Figure 7.18 and Table 7.9. It clearly

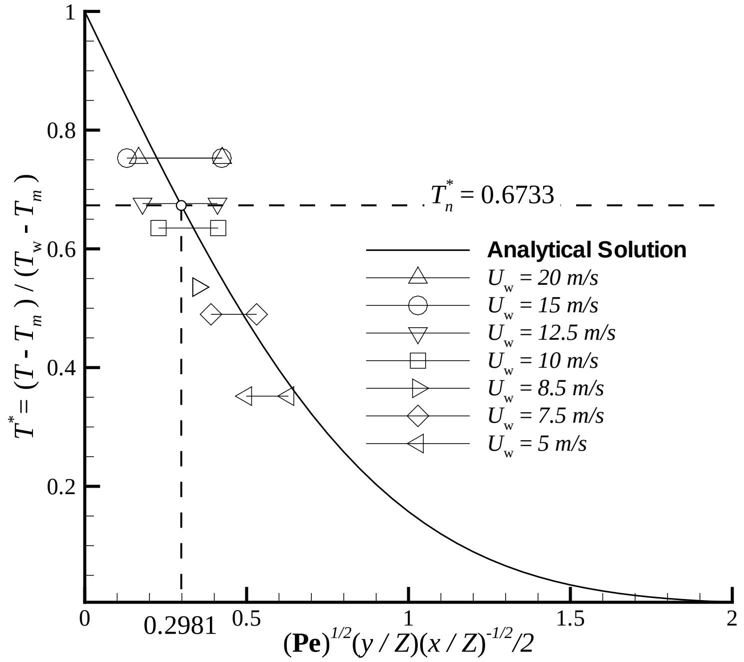

Figure 7.18 Normalized temperature profile due to heat conduction

indicates that heat conduction dominates near the melt-wheel contact area (compare with the analytical solution of Eq. (7.28)).

As demonstrated in Figure 7.19, when $850 \leqslant U_{\mathrm{w}} \leqslant 2000$ cm/s, the nucleation thickness δ_n falls between the upper and lower limits of the ribbon thickness, and when $2000 \leqslant U_{\mathrm{w}} \leqslant 4000$ cm/s δ_n is close to the lower limit from Kramer's experimental data[5], where δ_n is calculated according to Eq. (7.29) and the dimensionless foot length F/Z is quoted from [5]. For a stable delivery of amorphous ribbon, the lower limit of nucleation thickness δ_n should be greater than the lower limit of ribbon thickness δ. Figure 7.19 shows it is not satisfied at lower wheel speeds, namely $U_{\mathrm{w}} < 850$ cm/s.

The theoretical temperature at the wheel surface is halfway between the melting and the ambient temperatures. However, it is very difficult to predict the actual temperature at the melt-wheel boundary because heat transfer across the boundary is not as perfect as in one respective material – the molten alloy or the copper wheel. In practice, some gas or vacuum may be entrapped by the wheel and the free stream. These gas or vacuum pockets reduce the cooling rate greatly because they insulate the melt pool from

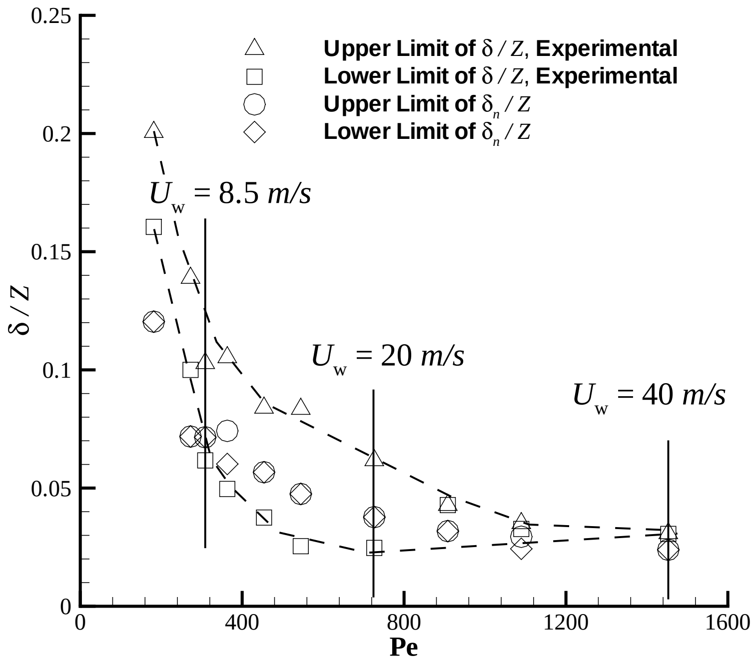

Figure 7.19 Ribbon layer δ and thermal layer δ_n with Peclet numbers

the wheel. It has also been observed from the experiments[49] that the temperature at the melt-wheel varies with the wetting contact condition among various runs and even within a single run. Besides, as a result of residual heat in the copper wheel the wheel surface temperature is higher than the ambient temperature after revolutions.

7.9 Estimates of the Cooling Rate and the Heat Transfer Coefficient

If the viscous dissipation is assumed to be contributed mainly by the velocity variation that follows Blasius' similar solution along the x-direction, the cooling rate near the wheel from viscous dissipation reduces to

$$\frac{\partial T}{\partial t} = \frac{2U_{\mathrm{w}}^3}{C_p x}\left(\frac{y}{x}\right)^2 f''^2 \tag{7.32}$$

from Eq. (4.2), where f is the nondimensional stream function and f' is the nondimensional velocity in the x-direction[92–94]. Interestingly, the cooling rate in Eq. (7.32) is

U_{w} (m/s)	20	15	12.5
Pe	726.46	544.84	454.04
Surface temperature T (K)	1108	1108	1158
T^{*}	.7529	.7529	.6763
μ (g/cms)	83.815	83.815	7.5236
Re	14.303	7.152	99.587
δ (cm)	.00196	.00196	.00294
	$\sim$ .005	$\sim$ .00637	$\sim$ .00676
δ/Z	.0242	.0242	.0363
	$\sim$ .06173	$\sim$ .0786	$\sim$ .0836
x/Z	3.8395	4.7037	4.7037
$\frac{\mathbf{Pe}^{1/2}}{2}\left(\frac{y}{Z}\right)\left(\frac{x}{Z}\right)^{-1/2}$	.1664	.1302	.1783
	$\sim$ .4245	$\sim$ .4231	$\sim$ .4100

Table 7.9 Measured surface temperature of pool and ribbon

independent of viscosity. According to the calculation and data in the previous sections, we find $\eta = 7.495$ on the isotherm of 1419 K, where η is the nondimensional similarity variable in the flat plate boundary layer solution given by

$$\eta = \frac{y}{\sqrt{\nu t}}. \tag{7.33}$$

Then $f'' = 0$ at $T = 1419$ K from [92] because in Blasius' solution, $f'' = 0$ at $\eta \geqslant 4.91$, where is outside the boundary layer. Hence, the temperature increase by viscous dissipation can be ignored where $T \geqslant 1419$ K in the melt pool.

From Eq. (7.28) we have cooling rate for Fe_{75}-Si_{10}-B_{15} alloy on the isotherm of $T = 1419$ K:

$$-\left.\frac{\partial T}{\partial t}\right)_{T=1419\ K} = 156.97\left(\frac{U_{\mathrm{w}}}{x}\right) \tag{7.34}$$

as plotted in Figure 7.20 under various wheel speeds.

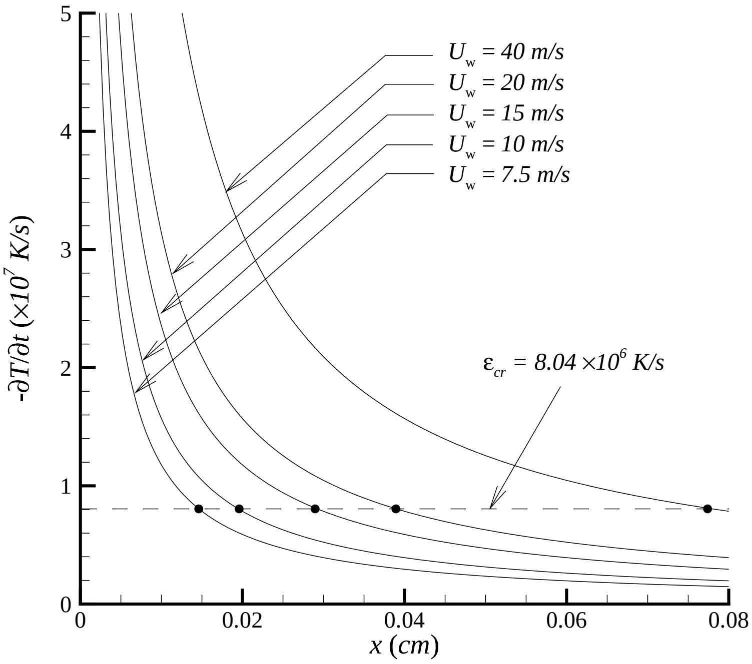

Figure 7.20 Cooling rate of the alloy at $T = 1419\ K$

Accordingly, the critical distance from point **C** on the wheel surface is defined in Figure 7.17 and as follows:

$$L_{cr} = 156.97 \left(\frac{U_{\mathrm{w}}}{\varepsilon_{cr}} \right) \quad \text{or} \quad 0.6061 U_{\mathrm{w}} t_n, \tag{7.35}$$

because $\varepsilon_{cr} = (1419 - 1160)/t_n$ (refer to Figure 7.2). Over a distance of L_{cr} from point **C**, the molten alloy cooling rate at the lower limit of melting temperature 1419 K must be greater than ε_{cr} to allow stable amorphous production from Eq. (7.34). Eq. (7.35) and Figure 7.20 demonstrate higher wheel speed creates larger L_{cr}. Apparently, L_{cr} relies on the wetting condition on the wheel as well.

Then we have two critical points, as indicated by points **R** and **R′** in Figure 7.17, both having an x-distance of L_{cr} to point **C**. Point **R** is on the wheel surface and point **R′** is on the isotherm of 1419 K. The cooling rate at point **R′** in the melt pool is equal to ε_{cr}, as denoted by the black dots in Figure 7.20. On the isotherm of 1419 K, the cooling rate is greater than ε_{cr} at $x < L_{cr}$, whereas it is less than ε_{cr} and crystallization may occur at $x > L_{cr}$.

Because we are unable to prevent nucleation occurring at $x > L_{cr}$ and $y > \delta_n$, we should lift the particles between the thermal layers δ_n and $\delta_{1419\ K}$ away the nucleation layer and force them to merge with the free stream of temperature higher than 1419 K. These particles having temperature of 1160 $K \leqslant T \leqslant 1419$ K should not influence the molten alloy within the free stream near the wheel surface. Accordingly, it is required that the wheel move a distance of $Z - L_{cr}$ in time less than t_c, namely,

$$Z - L_{cr} \leqslant U_{\mathrm{w}} t_c, \tag{7.36}$$

or

$$U_{\mathrm{w}} \geqslant \frac{Z}{0.6061 t_n + t_c}. \tag{7.37}$$

The actual flow velocity at point $\mathbf{R}'$ is less than U_{w}, but U_{w} is used instead in Eq. (7.36) for simplicity. The RHS of Eq. (7.37) underestimates the lower wheel speed limit, because we assume nucleation begins to happen at point $\mathbf{R}'$ on a perfect wetting condition. If nucleation is activated at point $\mathbf{C}$, the following modified formula

$$U_{\mathrm{w}} \geqslant \frac{Z}{t_c} \tag{7.38}$$

gives another lower wheel speed limit 810 cm/s, which is closer to the value of 800 cm/s observed in the experiments[5]. Eqs. (7.37) and (7.38) provide an estimated range of lower wheel speed limit.

$L_{cr} \leqslant F$ is necessary as shown in Figure 7.17; otherwise, the particles at the critical point $\mathbf{R}$ having the crystallization time t_c are inside the ribbon. We then reach the upper limit of wheel speed by

$$U_{\mathrm{w}} \leqslant \frac{F}{0.6061 t_n} \tag{7.39}$$

from Eq. (7.35).

Substitution of Eq. (7.28) into the 1D Newton's cooling law at melt-wheel boundary,

$$\left. k\frac{\partial T}{\partial y}\right)_{y=0} = h(T_m - T_{\mathrm{w}}), \tag{7.40}$$

yields the heat transfer coefficient along melt-wheel boundary:

$$h = \sqrt{\frac{\mathbf{Pe}}{\pi}} \left(\frac{k}{Z}\right) \left(\frac{x}{Z}\right)^{-1/2} = k\sqrt{\frac{U_{\mathrm{w}}}{\pi \alpha x}}. \tag{7.41}$$

Notice the heat transfer coefficient on the wheel surface is independent of Z. At the critical point $\mathbf{R}$, the heat transfer coefficient $h = 2.1635 \times 10^6$ W/m^2K, which is a constant, as denoted by the dashed line in Figure 7.21.

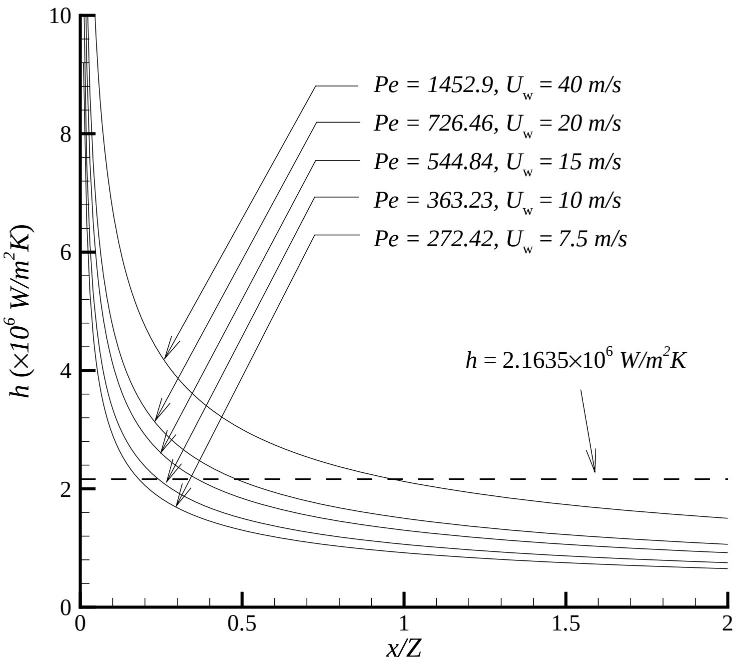

Figure 7.21 Heat transfer coefficient along the melt-wheel contact

7.10 Criteria for Amorphous Ribbon Formation

Crystalline alloy was often found on the air-side surface of the ribbon at low wheel speeds[5] because the alloy particles above T_n are dragged to the air-side surface. If δ is greater than δ_n at the pool-ribbon conjunction, namely cross-section **BG**, crystallization may be activated within the ribbon. From the temperature profile given in [5], at point **B** on free-side of ribbon, the measured temperatures are below T_n when $U_\mathrm{w} \geqslant 1250$ cm/s.

Better contact of melt pool with the wheel may produce larger δ_n and δ. Association of Eq. (7.29) with (7.18) gives a condition

$$\mathbf{Pr} \equiv \frac{\mathbf{Pe}}{\mathbf{Re}} \leqslant 3.226 \left(\frac{\mu_{\mathbf{B}}}{\mu_{1160\ K}} \right), \tag{7.42}$$

which guarantees $\delta_n \geqslant \delta$ for Fe$_{75}$-Si$_{10}$-B$_{15}$ alloy with the initial melting temperature 1600 K and $T_n = 1160$ K. The Prandtl number at **BG** should be less than the RHS of Eq. (7.42).

At $U_\mathrm{w} = 2000$ cm/s, **Pr** is found 50.791 based on the measured temperature 1108 K

at point **B**, and the RHS of Eq. (7.42) is 39.001 computed using the experimental data (refer to Table 7.9)[5]. Eq. (7.42) is not satisfied because the ribbon thickness predicted by Eq. (7.18) is larger than the lower limit of the experimental observation (refer to Figure 7.16).

If the predicted ribbon thickness by Eq. (7.14) is instead used for higher wheel speeds, the derived condition for $\delta_n \geqslant \delta$, namely

$$\mathbf{Pr} \leqslant 3.226 \left(\frac{S}{F}\right) \tag{7.43}$$

is still not met. But with the upper wheel speed limit as in Eq. (7.39) and $T \leqslant T_n$, we have

$$4.2605 \leqslant \mathbf{Pr} \equiv \frac{\mu}{\rho\alpha} \leqslant 5.3226 \left(\frac{S}{U_{\mathrm{w}} t_n}\right). \tag{7.44}$$

The temperature limits are given from Eq. (7.44) with (7.11):

$$1097\ K \leqslant T \leqslant 1160\ K \qquad \text{at point } \mathbf{B} \tag{7.45}$$

when $U_{\mathrm{w}} = 2000\ cm/s$, $t_n = 3.22 \times 10^{-5}\ s$, $S = 1.2\ cm$, $\rho = 7.4\ g/cm^3$, and $\alpha = 0.223\ cm^2/s$. The measured temperature of 1108 K at $U_{\mathrm{w}} = 2000\ cm/s$ falls within the temperature limits of Eq. (7.45). Likewise, the conditions can be obtained through the same method for $U_{\mathrm{w}} = 1500\ cm/s$ and other wheel speeds. The lower temperature limit exists as in Eq. (7.45) for amorphous production because lower temperature induces stronger viscous force and accordingly, larger ribbon thickness.

CHAPTER 8 CONCLUSION

A robust and efficient free surface flow solver has been developed and used in the analysis and design of free-jet melt spinning. The evolutions of pool and ribbon in a free-jet melt spinning were simulated; some important flow dynamics and heat transfer within the pool were found from the velocity and temperature distributions.

The molten alloy jet is undercooled by the quench copper wheel by means of heat conduction. The wheel casts a thin ribbon through viscous and adhesive forces. A flow circulation forms within the melt pool under stronger viscous friction and molten alloy surface tension force. The flow circulation transports the particles that are not undercooled away the ribbon pipe and mixes them with the melt stream so that crystallization is prevented in the melt pool and the ribbon. A successful process must have a wheel speed large enough to give rise to a stable circulation inside the melt pool, and viscosity and surface tension large enough to drag a thin layer out of the pool. Meanwhile, the wheel speed is lower than a criterion that amorphous alloy can evolve fast to be a stable layer before it is spun out. The wetting condition at the melt-wheel boundary is crucial because it affects the cooling rate and the viscous friction.

The VOF method is widely used as a CFD technique for interface tracking; however, some facts about VOF function are often overlooked in the applications. VOF function varies smoothly in the tangential direction of a free surface, whereas it exhibits sharpness in the normal direction simply because VOF function experiences variations from zero to unity value over no more than three grid cells in this direction. The sharpness cannot be mitigated but intensified by higher mesh resolutions. Accordingly, the accuracy of numerical solutions can by no means be improved if the finite difference or finite volume scheme applied is divergent. One should ensure the convergence of numerical solutions before he improves the accuracy of the numerical methods for the discontinuity convection. The DA algorithm developed in this work offers second-order accurate convergent surface normal and curvature, and formulations of surface tension force for free surface advection.

Although surface tension is constructed to be a continuous volumetric force over the entire flow, the CSF model fails to recover the pressure jump that appears in Laplace's formula. According to the physical observation, surface tension is found only within a very thin region between two immiscible fluids. The classifications of grid cells and control cells restrict surface tension to reside a narrow layer along the free surface, and attain the integral effect of surface tension in flow pressure over the rest flow field.

The idea of immersed length proposed in this work comes originally from hydrostatics. It is first introduced in the evaluations of density and volumetric surface tension force. The numerical approach for pressure solution is also improved in that the pressure is sought only at those immersed grid cell centers. Spurious currents have been successfully eliminated using the modified numerical approach, the reconstructed CSF model, and the DA algorithm.

CHAPTER 9 RECOMMENDATIONS

The DA algorithm can be extended in 3D computations for surface normal and curvature when a free surface is approximated by planar patches in a cubic-celled flow field. Two surface principal curvatures are estimated with some additional calculations for 3D free surfaces. The 'immersed length' concept can also be implemented in the numerical approach for 3D surface flows. The modified pressure approach is applicable to 3D surface flow simulations, though, after a validation of the 3D CSF model.

The H-N algorithm for free surface evolution is an explicit stair-stepped approximation. Absolutely, a linear approximation is more accurate and furthermore, I would suggest a development of an implicit scheme for free surface evolution.

For future research on free-jet melt spinning, here are some recommendations.

- If the wheel curvature or surface roughness is considered as a factor influencing the molten alloy flow and the wetting distance, the y-component velocity of wheel speed should be included in the translation terms.

- In a free-jet melt spinning, the melt alloy evolves from an axisymmetric stream to a thin ribbon flow with large width. Further investigation using 3D surface flow models is thus needed to reveal the relationships among the wheel speed, the ejection velocity, the Reynolds number of molten jet, surface tension force, and the ratio of orifice diameter to ribbon width.

- A mathematical model is desired to analyze the stability of molten flow temperature at the melt-wheel boundary relating to gas pockets, and seek the dependence of gas pocket formation on wheel speed, wheel curvature, wheel surface roughness, molten flow pressure, and the meniscus of molten stream.

- Research into viscous friction and heat transfer (hidden heat released) in the phase change between the solidified alloy and the molten flow is suggested.

Finally, the author would like to see any experimental measurements of velocity and temperature of melt spinning.

APPENDIX A A FINITE DIFFERENCE SCHEME FOR THERMAL CONVECTION AND DIFFUSION

Finite volume method is employed to compute the conservative convection term $\nabla \cdot (\vec{V}T)$ in Eq. (4.2), if the neighboring cell centers are all immersed:

$$\begin{aligned}\nabla \cdot (\vec{V}T)_{i,j} =& \frac{1}{r_i^\delta \delta x_i} \left[(r^\delta u)_{i+1/2,j} \langle T \rangle_{\mathrm{R}} - (r^\delta u)_{i-1/2,j} \langle T \rangle_{\mathrm{L}} \right] \\ &+ \frac{1}{\delta y_j} \left[v_{i,j+1/2} \langle T \rangle_{\mathrm{T}} - v_{i,j-1/2} \langle T \rangle_{\mathrm{B}} \right].\end{aligned} \tag{A.1}$$

In Eq. (A.1) the temperature at the center of right face of the control volume $\langle T \rangle_{\mathrm{R}}$, for instance, shown in Figure A.1, is given by interpolation:

$$\langle T \rangle_{\mathrm{R}} = \frac{\delta x_i}{\delta x_\alpha} (1 - \alpha s_u)\, T_{i+1,j} + \frac{\delta x_{i+1}}{\delta x_\alpha} (1 + \alpha s_u)\, T_{i,j} \tag{A.2}$$

and

$$\delta x_\alpha = \delta x_i + \delta x_{i+1} + \alpha s_u (\delta x_{i+1} - \delta x_i), \qquad s_u = \mathrm{sign}(u_{i+1/2,j}), \tag{A.3}$$

where the upstream differencing control parameter α satisfies $0 \leqslant \alpha \leqslant 1$ if its right neighbor, namely cell $(i+1, j)$, has $F \geqslant 0.5$. If one of the neighboring cells has $F < 0.5$, the finite volume method is no longer valid because the temperature may not be continuous across the interface. The temperature at a control cell center is approximately equal to that at its neighboring grid cell center if both grid cell centers are not immersed.

For the approximation of the nonconservative heat convection term, it is computed as follows:

$$(\vec{V} \cdot \nabla T)_{i,j} = \left\langle u \frac{\partial T}{\partial x} \right\rangle_{i,j} + \left\langle v \frac{\partial T}{\partial y} \right\rangle_{i,j}. \tag{A.4}$$

The quantities in the RHS of Eq. (A.4) are estimated by interpolation:

$$\begin{aligned}\left\langle u \frac{\partial T}{\partial x} \right\rangle_{i,j} =& \frac{1}{2} (1 - \alpha s_u)\, u_{i+1/2,j} \left(\frac{\partial T}{\partial x} \right)_{i+1/2,j} \\ &+ \frac{1}{2} (1 + \alpha s_u)\, u_{i-1/2,j} \left(\frac{\partial T}{\partial x} \right)_{i-1/2,j}\end{aligned} \tag{A.5}$$

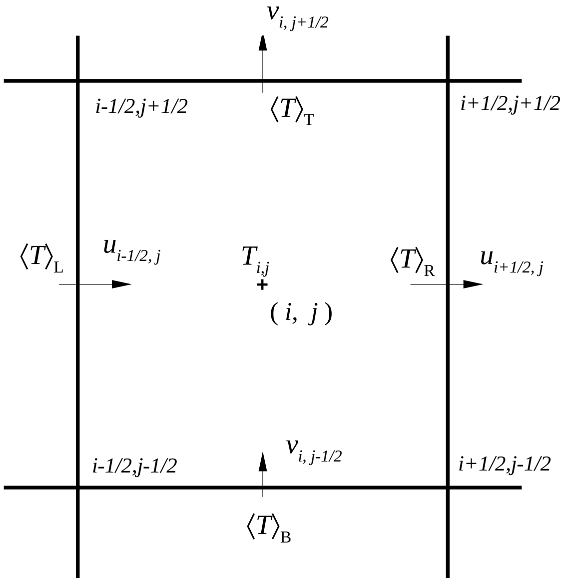

Figure A.1 Temperature location and heat convection terms in a cell (i, j)

and

$$\left\langle v\frac{\partial T}{\partial y}\right\rangle_{i,j} = \frac{1}{2}\left(1-\alpha s_v\right) v_{i,j+1/2}\left(\frac{\partial T}{\partial y}\right)_{i,j+1/2} + \frac{1}{2}\left(1+\alpha s_v\right) v_{i,j-1/2}\left(\frac{\partial T}{\partial y}\right)_{i,j-1/2} \tag{A.6}$$

where s_u is given as in Eq. (A.3) and so is s_v. The gradients of temperature in Eqs. (A.5) and (A.6), for example, at points $(i+1/2, j)$ and $(i, j+1/2)$, respectively, are computed by Eq. (A.9) if the both grid cell centers are immersed.

In Section 4.2 of Chapter 4, the temperature gradients on free surface are given in Eqs. (4.10) and (4.11). Then the coefficient 1/2 in Eq. (A.5) or (A.6), for example, should be modified as $\delta x_i/\delta x_\alpha$; δx_i and δx_α are also modified according to the immersed length (refer to Figure 5.7).

For the thermal diffusive term in Eq. (4.2), the same algorithm is adopted as in the estimation of the viscosity term in [16].

$$\left[\frac{\alpha}{r^\delta}\frac{\partial}{\partial x}\left(r^\delta\frac{\partial T}{\partial x}\right)\right]_{i,j} = \frac{\alpha}{r^\delta_{i,j}\delta x_i}\left[r^\delta_{i+1/2,j}\left(\frac{\partial T}{\partial x}\right)_{i+1/2,j} - r^\delta_{i-1/2,j}\left(\frac{\partial T}{\partial x}\right)_{i-1/2,j}\right] \tag{A.7}$$

and

$$\left[\alpha\frac{\partial^2 T}{\partial y^2}\right]_{i,j} = \frac{\alpha}{\delta y_j}\left[\left(\frac{\partial T}{\partial y}\right)_{i,j+1/2} - \left(\frac{\partial T}{\partial y}\right)_{i,j-1/2}\right], \tag{A.8}$$

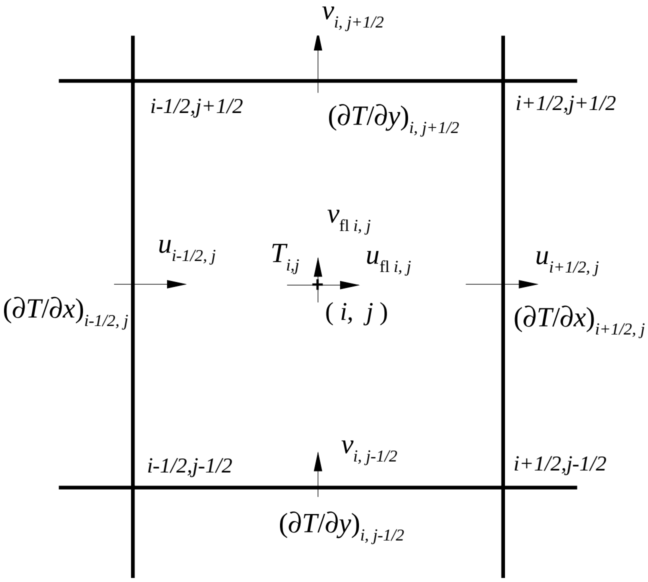

Figure A.2 Heat convection estimated in nonconservative form

where α is the thermal diffusivity and the gradients of temperature on the right and top faces, for example, are as follows, respectively:

$$\left(\frac{\partial T}{\partial x}\right)_{i+1/2,j} = \frac{T_{i+1,j} - T_{i,j}}{\delta x_{i+1/2}}, \qquad \left(\frac{\partial T}{\partial y}\right)_{i,j+1/2} = \frac{T_{i,j+1} - T_{i,j}}{\delta y_{j+1/2}} \tag{A.9}$$

for an interior cell whose four neighboring cells have $F \geqslant 0.5$. δx_i and δy_j in Eqs. (A.7) and (A.8) should be modified according to the immersed lengths if the corresponding neighboring cells have $F < 0.5$.

APPENDIX B FORMULATION OF THE CONTINUUM SURFACE FORCE (CSF) MODEL

In the CSF model[14], we let the color function $\tilde{c}(\vec{x})$ equal to the VOF function $F(\vec{x})$, then

$$\vec{F}_{\text{sv}} = \sigma\kappa\left(\vec{x}\right)\nabla F(\vec{x})g(\vec{x}), \tag{B.1}$$

where the function $g(\vec{x})$ is given:

$$g(\vec{x}) = 1 \quad \text{or} \quad F(\vec{x})/\left\langle F\right\rangle \tag{B.2}$$

with $\langle F\rangle = 1/2$, the average of the two colors of the fluids. The first option, $g(\vec{x}) = 1$, locates the force in the transition region at the point of maximum $|\nabla F|$, near the $F = 1/2$ contour; accordingly, Eq. (3.26) becomes (3.8). When the second option $g(\vec{x}) = 2F$ is chosen, the force is biased toward the fluid side of the transition region, where F is between 1 and 1/2. The second option is recommended according to [16] since the surface tension force is weighted on the free surface by VOF function F and it may result in better computational data of free surface because fluid accelerations due to surface tension are then proportional to density gradients, rather than density itself.

The volume force due to surface tension, like pressure and VOF function, is centered at each mesh cell, as are the local curvature κ, function $g(\vec{x})$, and normal vector $\vec{n}$ as shown in Figure B.1. Thus Eq. (3.26) becomes

$$\vec{F}_{\text{sv}i,j} = \sigma\kappa_{i,j}g_{i,j}\vec{n}_{i,j} \tag{B.3}$$

where $\vec{n}_{i,j}$ (see Eq. (3.12)) can be computed as follows:

$$\vec{n}_{i,j} = \frac{1}{4}\left(\vec{n}_{i+1/2,j+1/2} + \vec{n}_{i+1/2,j-1/2} + \vec{n}_{i-1/2,j+1/2} + \vec{n}_{i-1/2,j-1/2}\right). \tag{B.4}$$

In Eq. (B.4), the normal at vertex $(i+1/2, j+1/2)$, for example, is

$$\begin{aligned}\vec{n}_{i+1/2,j+1/2} = &\left[\frac{(F_{i+1,j+1} - F_{i,j+1})\delta y_j + (F_{i+1,j} - F_{i,j})\delta y_{j+1}}{(\delta y_j + \delta y_{j+1})\delta x_{i+1/2}}\right]\hat{\imath} \\ &+ \left[\frac{(F_{i+1,j+1} - F_{i+1,j})\delta x_i + (F_{i,j+1} - F_{i,j})\delta x_{j+1}}{(\delta x_i + \delta x_{i+1})\delta y_{j+1/2}}\right]\hat{\jmath}.\end{aligned} \tag{B.5}$$

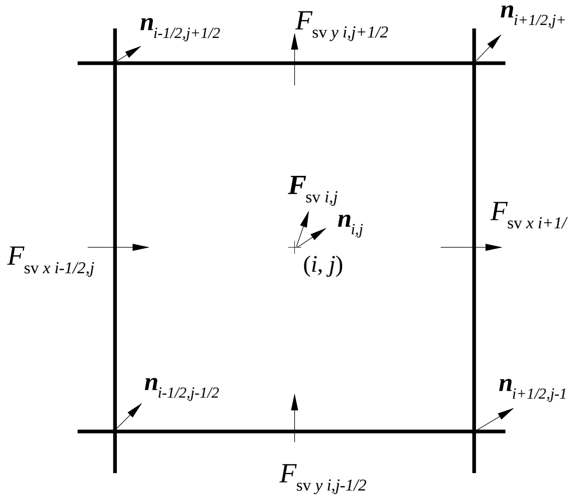

Figure B.1 Surface tension force and normals in a cell (i, j)

Then the cell-centered normals and their two components n_x and n_y can be obtained by averaging four vertex normals of each cell.

The standard formula for surface curvature of free surface is given by Eq. (3.10),

$$\kappa = -(\nabla \cdot \hat{n}) = \frac{1}{|\vec{n}|}\left[\left(\frac{\vec{n}}{|\vec{n}|} \cdot \nabla\right)|\vec{n}| - (\nabla \cdot \vec{n})\right]. \tag{B.6}$$

The first term on the RHS of Eq. (B.6) can be computed by:

$$\begin{aligned}\left(\frac{\vec{n}_{i,j}}{|\vec{n}_{i,j}|} \cdot \nabla\right)|\vec{n}| &= \left(\frac{n_x}{|\vec{n}|}\right)_{i,j}\left(\frac{\partial|\vec{n}|}{\partial x}\right)_{i,j} + \left(\frac{n_y}{|\vec{n}|}\right)_{i,j}\left(\frac{\partial|\vec{n}|}{\partial y}\right)_{i,j} \\ &= \left(\frac{n_x}{|\vec{n}|}\right)^2_{i,j}\left(\frac{\partial n_x}{\partial x}\right)_{i,j} + \left(\frac{n_x n_y}{|\vec{n}|^2}\right)_{i,j}\left(\frac{\partial n_x}{\partial y} + \frac{\partial n_y}{\partial x}\right)_{i,j} \\ &+ \left(\frac{n_y}{|\vec{n}|}\right)^2_{i,j}\left(\frac{\partial n_y}{\partial y}\right)_{i,j},\end{aligned} \tag{B.7}$$

where the derivatives of $\vec{n}$ components are listed in the following equations:

$$\left(\frac{\partial n_x}{\partial x}\right)_{i,j} = \frac{1}{2\delta x_i}\left[n_{xi+1/2,j+1/2} + n_{xi+1/2,j-1/2} - n_{xi-1/2,j+1/2} - n_{xi-1/2,j-1/2}\right], \tag{B.8}$$

$$\left(\frac{\partial n_y}{\partial y}\right)_{i,j} = \frac{1}{2\delta y_j}\left[n_{yi+1/2,j+1/2} + n_{yi-1/2,j+1/2} - n_{yi+1/2,j-1/2} - n_{yi-1/2,j-1/2}\right], \tag{B.9}$$

$$\left(\frac{\partial n_x}{\partial y}\right)_{i,j} = \frac{1}{2\delta y_i}\left[n_{xi+1/2,j+1/2} + n_{xi-1/2,j+1/2} - n_{xi+1/2,j-1/2} - n_{xi-1/2,j-1/2}\right], \qquad \text{(B.10)}$$

and

$$\left(\frac{\partial n_y}{\partial x}\right)_{i,j} = \frac{1}{2\delta x_i}\left[n_{yi+1/2,j+1/2} + n_{yi+1/2,j-1/2} - n_{yi-1/2,j+1/2} - n_{yi-1/2,j-1/2}\right]. \qquad \text{(B.11)}$$

The computation of the second term on the RHS of Eq. (B.6) follows that

$$(\nabla \cdot \vec{n})_{i,j} = \frac{1}{r_i^\delta}\frac{\partial}{\partial x}\left(r^\delta n_x\right)_{i,j} + \left(\frac{\partial n_y}{\partial y}\right)_{i,j}, \qquad \text{(B.12)}$$

where

$$\begin{aligned}\frac{1}{r_i^\delta}\left(r^\delta\frac{\partial n_x}{\partial x}\right)_{i,j} =& \frac{1}{2\delta x_i r_i^\delta}\left[r_{i+1/2}^\delta\left(n_{xi+1/2,j+1/2} + n_{xi+1/2,j-1/2}\right)\right.\\ &\left.-r_{i-1/2}^\delta\left(n_{xi-1/2,j+1/2} - n_{xi-1/2,j-1/2}\right)\right].\end{aligned} \qquad \text{(B.13)}$$

Eqs. (B.4) to (B.13) are called the ALE-like scheme of computing local normal and curvature.

In the MAC scheme as given in Eqs. (B.14) to (B.20), the curvature is evaluated by directly differentiating the unit normals at the centers of four cell sides. The cell-centered normal vector of a cell $\vec{n}_{i,j}$ is obtained by linear interpolation of its face-centered components, namely,

$$\vec{n}_{i,j} = \frac{1}{2}\left(n_{xi+1/2,j} + n_{xi-1/2,j}\right)\hat{\imath} + \frac{1}{2}\left(n_{yi,j+1/2} + n_{yi,j-1/2}\right)\hat{\jmath}, \qquad \text{(B.14)}$$

and a cell-centered curvature $(\nabla \cdot \hat{n})_{i,j}$ is given from

$$(\nabla \cdot \hat{n})_{i,j} = \frac{1}{\delta x}\left(\hat{n}_{xi+1/2,j} - \hat{n}_{xi-1/2,j}\right) + \frac{1}{\delta y}\left(\hat{n}_{yi,j+1/2} - \hat{n}_{yi,j-1/2}\right), \qquad \text{(B.15)}$$

where the unit normal at right face center $(i+1/2, j)$, for example, is

$$\hat{n}_{i+1/2,j} = \frac{n_{xi+1/2,j}\hat{\imath} + n_{yi+1/2,j}\hat{\jmath}}{|n_{xi+1/2,j}^2 + n_{yi+1/2,j}^2|^{1/2}}, \qquad \text{(B.16)}$$

as is the unit normal at the top face center $(i, j+1/2)$. The x- and y-components of normal at the right face center and top face center are computed, respectively, as follows:

$$n_{xi+1/2,j} = \frac{F_{i+1,j} - F_{i,j}}{\delta x} \qquad \text{(B.17)}$$

and

$$n_{yi,j+1/2} = \frac{F_{i,j+1} - F_{i,j}}{\delta y}, \tag{B.18}$$

while the y- and x-components of normal at the right face center and top face center are evaluated by linear interpolation, respectively:

$$n_{yi+1/2,j} = \frac{1}{4}\left(n_{yi,j+1/2} + n_{yi+1,j+1/2} + n_{yi,j-1/2} + n_{yi+1,j-1/2}\right) \tag{B.19}$$

and

$$n_{xi+1/2,j} = \frac{1}{4}\left(n_{xi+1/2,j} + n_{xi+1/2,j+1} + n_{xi-1/2,j} + n_{xi-1/2,j+1}\right). \tag{B.20}$$

The volume forces due to surface tension at the centers of the cell faces as shown in Figure B.1 are computed by interpolating the values at neighboring cell centers on both sides:

$$F_{\mathrm{sv}xi+1/2,j} = \frac{\delta x_i F_{\mathrm{sv}xi+1,j} + \delta x_{i+1} F_{\mathrm{sv}xi,j}}{\delta x_i + \delta x_{i+1}} \tag{B.21}$$

and

$$F_{\mathrm{sv}yi,j+1/2} = \frac{\delta y_j F_{\mathrm{sv}yi,j+1} + \delta y_{i+1} F_{\mathrm{sv}yi,j}}{\delta y_i + \delta y_{i+1}}. \tag{B.22}$$

RIPPLE also provides a stencil or mask matrix for the convolution kernel function of Eq. (3.27) as follows when the color function $\tilde{c}(\vec{x}) = \tilde{\rho}(\vec{x})$ for a cell and its eight neighboring cells:

$$\frac{1}{64}\begin{array}{|c|c|c|}\hline 1 & 6 & 1 \\ \hline 6 & 36 & 6 \\ \hline 1 & 6 & 1 \\ \hline\end{array} \tag{B.23}$$

which is derived from a B-spline approximation and Eq. (3.27), according to [16].

APPENDIX C FORMULATION OF HEAT EQUATION IN 2D COORDINATES

Eq. (4.2) in two-dimensional conservative forms is presented:

$$\begin{aligned}\frac{\partial T}{\partial t}+\frac{\partial}{\partial x}(uT)+\frac{\partial}{\partial y}(vT)=&\frac{\nu}{C_p}\left[2\left(\frac{\partial u}{\partial x}\right)^2+\left(\frac{\partial u}{\partial y}+\frac{\partial v}{\partial x}\right)^2+2\left(\frac{\partial v}{\partial y}\right)^2\right]\\&+\alpha\left[\frac{\partial^2 T}{\partial x^2}+\frac{\partial^2 T}{\partial y^2}\right],\end{aligned}\tag{C.1}$$

for the Cartesian coordinate system, and

$$\begin{aligned}\frac{\partial T}{\partial t}+\frac{1}{r}\frac{\partial}{\partial r}(ruT)+\frac{\partial}{\partial z}(vT)=&\frac{\nu}{C_p}\left[2\left(\frac{\partial u}{\partial r}\right)^2+\left(\frac{\partial u}{\partial z}+\frac{\partial v}{\partial r}\right)^2+2\left(\frac{\partial v}{\partial z}\right)^2\right]\\&+\alpha\left[\frac{1}{r}\frac{\partial}{\partial r}\left(r\frac{\partial T}{\partial r}\right)+\frac{\partial^2 T}{\partial z^2}\right],\end{aligned}\tag{C.2}$$

for the cylindrical coordinate system, respectively.

The nonconservative convection terms are identical for the Cartesian and the cylindrical coordinate systems (see Appendix A).

The boundary conditions on free surface, namely Eq. (2.27), for heat transfer in the cylindrical system are formulated as follows:

$$\frac{\partial T}{\partial r}n_r+\frac{\partial T}{\partial z}n_z=\frac{|\vec{n}|}{k}\left(h\left(T-T_{\mathrm{a}}\right)+\epsilon\sigma_{\mathbf{SB}}(T^4-T_{\mathrm{a}}^4)\right),\tag{C.3}$$

where (n_r, n_z) is two components of the normal $\vec{n}$ to free surface (see Eq. (3.12)):

$$n_r=\frac{\partial F}{\partial r},\qquad n_z=\frac{\partial F}{\partial z},\qquad |\vec{n}|=\sqrt{n_r^2+n_z^2}.\tag{C.4}$$

BIBLIOGRAPHY

[1] A. R. Yavari. A new look at the kinetics of formation and the stability of metallic glasses. In *Amorphous Metals and Non-Equilibrium Processing, Ed. by M. von Allmen*, les éditions de physique, June 1984.

[2] Paul H. Steen and Christian Karcher. Fluid Mechanics of Spin Casting of Metals. *Annual Review of Fluid Mechanics*, 29:373–397, 1997.

[3] M. Cohen, B. H. Kear, and R. Mehrabian. Rapid Solidification Processing - An Outlook. In *Rapid Solidification Processing, Principles and Technologies, II, Ed. Mehrabian, Kear and Cohen*, Baton Rouge, Claitor's Publishing Division, March 1980.

[4] H. Jones. *Rapid Solidification of Metals and Alloys.* The Institution of Metallurgists, Northway House, High Road, Weststone, London N20 9LW, 1982.

[5] M. J. Kramer, H. Meco, K. W. Dennis, E. Vargonova, R. W. McCallum, and R. E. Napolitano. Rapid Solidification and Metallic Glass Formation - Experimental and Theoretical Limits. *Journal of Noncrystalline Solids*, 353:3633–3639, 2007.

[6] E. M. Gutierrez and J. Szekely. Mathematical model of the planar flow melt spinning process. *Metallurgical Transactions B*, 17B:695–703, 1986.

[7] D. B. Kothe, W. J. Rider, S. J. Mosso, J. S. Brock, and J. I. Hochstein. Volume Tracking of Interfaces Having Surface Tension in Two and Three Dimensions. *AIAA Journal*, AIAA Paper 96-0859, January 1996.

[8] Ruben Scardovelli and Stéphane Zaleski. Direct Numerical Simulation of Free-surface and Interfacial Flow. *Annual Review of Fluid Mechanics*, 31:567–603, 1999.

[9] J. M. Floryan and H. Rasmussen. Numerical methods for viscous flows with moving boundaries. *Applied Mechanics Reviews*, 42(12):323–341, 1989.

[10] C. W. Hirt and B. D. Nichols. Volume of Fluid (VOF) Method for the Dynamics of Free Boundaries. *Journal of Computational Physics*, 39:201–225, January 1981.

[11] Stanley Osher and Ronald Fedkiw. *Level Set Methods and Dynamic Implicit Surfaces*. Springer-Verlag New York, Inc., New York, 2003.

[12] J. A. Sethian. *Level Set Methods and Fast Marching Methods : Evolving Interfaces in Computational Geometry, Fluid Mechanics, Computer Vision, and Materials Science*. Cambridge University Press, New York, 1999.

[13] J. A. Sethian and Peter Smereka. Level Set Methods for Fluid Interfaces. *Annual Review of Fluid Mechanics*, 35:341–72, 2003.

[14] J. U. Brackbill, D. B. Kothe, and C. Zemach. A continuum method for modeling surface tension. *Journal of Computational Physics*, 100:335–354, 1992.

[15] D. B. Kothe and R. C. Mjolsness. RIPPLE: A New Model for Incompressible Flows with Free Surfaces. *AIAA Journal*, 30(11):2694–2700, November 1992.

[16] Douglas B. Kothe, Raymond C. Mjolsness, and Martin D. Torrey. *RIPPLE: A Computer Program for Incompressible Flows with Free Surface*. Los Alamos National Laboratory, Los Alamos, New Mexico 87545, April 1991.

[17] B. Lafaurie, C. Nardone, R. Scardovelli, S. Zaleski, and G. Zanetti. Modelling Merging and Fragmentation in Multiphase Flows with SURFER. *Journal of Computational Physics*, 113(1):134–147, July 1994.

[18] Masatake Mori. *The Finite Element Methods and Its Applications*. Macmillan Publishing Company, Collier Macmillan Canada, Inc., Collier Macmillan Publishers, 1986.

[19] D. B. Kothe. PERSPECTIVE ON EULERIAN FINITE VOLUME METHODS FOR INCOMPRESSIBLE INTERFACIAL FLOWS. In *Free Surface Flows, edited by Hendrik C. Kuhlmann and Hans-Josef Rath*, Springer-Verlag Wien New York, 1998.

[20] F. H. Harlow and J. E. Welch. Numerical calculation of time-dependent viscous incompressible flow of fluid with free surface. *The Physics of Fluids*, 8:2182–2189, 1966.

[21] C. W. Hirt, A. A. Amsden, and J. L. Cook. An arbitrary Lagrangian-Eulerian computing method for all flow speeds. *Journal of Computational Physics*, 14:227–253, March 1974.

[22] W. Shyy, H. S. Udaykumar, M. M. Rao, and R. W. Smith. *Computational Fluid Dynamics with Moving Boundaries*. Tayler & Francis, Washington DC, 1996.

[23] Y. Renardy and M. Renardy. PROST: A Parabolic Reconstruction of Surface Tension for the Volume-of-Fluid Method. *Journal of Computational Physics*, 183:400–421, 2002.

[24] M. Meier, H. Yadigaroglu, and B. L. Smith. A novel technique for including surface tension in PLIC-VOF methods. *European Journal of Mechnics - B/Fluids*, 21: 61–73, 2002.

[25] A. K. Gunstensen. Lattice-Boltzmann Studies of Multiphase Flow through Porous Media. Doctorate thesis, Massachusetts Institute of Technology, Cambridge, MA, 1992.

[26] Didier Jamet, David Torres, and J. U. Brackbill. On the Theory and Computation of Surface Tension: The Elimination of Parasitic Currents through Energy Conservation in the Second-Gradient Method. *Journal of Computational Physics*, 182: 262–276, October 2002.

[27] E. Shirani, N. Ashgriz, and J. Mostaghimi. Interface pressure calculation based on conservation of momentum for front capturing methods. *Journal of Computational Physics*, 203:154–175, Febuary 2003.

[28] Stanley A. Berger and Daniel K. Ai. A simple fluid mechanical model for planar flow casting melt-spinning. *Metallurgical and Materials Transactions B*, 19(3):571–579, 1988.

[29] C. Karcher and P. H. Steen. High-Reynolds number flow in a narrow gap driven by solidification I. Theory. *Physics of Fluids*, 13(4):826–833, April 2001.

[30] C. Karcher and P. H. Steen. High-Reynolds number flow in a narrow gap driven by solidification II. Planar-flow casting application. *Physics of Fluids*, 13(4):834–840, April 2001.

[31] P. G. Zielinski and D. G. Ast. Turbulent flow in chillblock casting. Scripta Metallurgica, 17:291–294, 1983.

[32] H. Hillmann and H. R. Hilzinger. Rapidly Quenched. In *Met. Proc. Int. Conf. 3rd 1*, 1978.

[33] Howard H. Liebermann. *Rapidly Solidified Alloy.* Marcel Dekker, Inc., New York, NY, 1993.

[34] K. Takeshita and P. H. Shingu. An analysis of the ribbon formation process by the single roller rapid solidification technique. *Transactions of the Japan Institute of Metals*, 24(7):529–536, 1983.

[35] G-X Wang and E. F. Matthys. Mathematical simulation of melt flow, heat transfer and non-equilibrium solidification in planar flow casting. *Modelling and Simulation in Materials Science and Engineering*, 10:35–55, 2002.

[36] J. K. Carpenter and P. H. Steen. Heat transfer and solidification in planar-flow melt-spinning: high wheelspeeds. *Int. J. Heat Mass Transfer*, 40(9):1993–2007, 1997.

[37] K. Takeshita and P. H. Shingu. Thermal contact during the cooling by the single roller chill block casting. *Transactions of the Japan Institute of Metals*, 27(6):454–462, 1986.

[38] S. C. Huang and H. C. Fiedler. Effects of wheel surface conditions on the casting of amorphous metal ribbons. *Metallurgical Transactions A*, 12:1107–1112, 1981.

[39] M. Bussmann, J. Mostaghimi, D. W. Kirk, and J. W. Graydon. A numerical study of steady flow and temperature fields within a melt spinning puddle. *International Journal of Heat and Mass Transfer*, 45:3997–4010, 2002.

[40] T. W. Clyne. Numerical Treatment of Rapid Solidification. *Metallurgical Transactions B*, 15B:369–381, June 1984.

[41] N. H. Pryds and J. H. Hattel. Numerical Modelling of Rapid Solidification. *Modelling and Simulation in Materials Science and Engineering*, 5:451–472, 1997.

[42] T. F. Kelly, M. Cohen, and J. B. Vander Sande. Rapid Solidification of a Droplet-Processed Stainless Steel. *Metallurgical Transactions A*, 15A:819–833, May 1994.

[43] M. R. Glickstein, R. J. Patterson II, and N. E. Shockey. Rapid Solidification Effects of Mircron-size Droplets. In *Rapid solidification Processing, Principles and Technologies, Ed. Mehrabian, Kear and Cohen*, Baton Rouge, Claitor's Publishing Division, 1977.

[44] K. Takeshita and P. H. Shingu. An analysis of melt puddle formation in the single roller chill block casting. *Transactions of the Japan Institute of Metals*, 27(2):141–148, 1986.

[45] S. L. Wu, C. W. Chen, W. S. Hwang, and C. C. Yang. Analysis for melt puddle in the planar flow casting process – A mathematical modelling study. *Appl. Math. Modell.*, 16:394–403, 1992.

[46] C. W. Chen and W. S. Hwang. A three-dimensional fluid flow model for puddle formation in the single-roll rapid solidification process. *Appl. Math Modell*, 40(9): 704–712, 1995.

[47] D. R. Korzekwa, L. A. Jacobson, and H. W. Hirt. Modeling planar flow casting with FLOW-3D. In *Melt-spinning and Strip Casting: Research and Implementation TMS, Ed. E. F. Mattys*, Warrendale, PA, 1992.

[48] H. A. Davies, B. G. Levis, and I. W. Donald. COMPARISON OF ROLLER QUENCHING AND MELT SPINNING FOR CONTINUOUS CASTING OF STRIP. In *Rapid solidification Processing, Principles and Technologies, Ed. Mehrabian, Kear and Cohen*, Baton Rouge, Claitor's Publishing Division, November 1977.

[49] R. E. Napolitano and H. Meco. The Role of Melt Pool Behavior in Free-Jet Melt Spinning. *Metallurgical and Materials Transactions A*, 35A:1539–1553, May 2004.

[50] G-X Wang and E. F. Matthys. Experimental determination of the interfacial heat transfer during cooling and solidification of molten metal droplets impacting on a metallic substrate: effect of roughness and superheat. *International Journal of Heat and Mass Transfer*, 45:4967–4981, 2002.

[51] L. A. Segel. *Mathematics Applied to Continuum Mechanics.* MacMillan Publishing Co., Inc., New York, 1977.

[52] V. Alexiades and A. D. Solomon. *Mathematical Modeling of Melting and Freezing Process.* Hemisphere Publishing Corporation, 1993.

[53] A. J. Chorin and J. E. Marsden. *A Mathematical Introduction to Fluid Mechanics.* Springer-Verlag, New York, 1979.

[54] Randall J. LeVeque. *Numerical Methods for Conservation Laws.* Birkhäuser Verlag, German, 1992.

[55] L. D. Landau and E. M. Lifshitz. *Fluid Mechanics.* Pergamon, New York, 1959.

[56] G. K. Batchelor. *An Introduction to Fluid Dynamics.* Cambridge University Press, Cambridge, Britain, 1967.

[57] Yulii D. Shikhmurzaev. *Capillary Flows with Formaing Interfaces.* Chapman & Hall/CRC, Taylor & Francis Group, 2007.

[58] Sir H. Lamb. *Hydrodynamics.* Cambridge University Press and Dover Publications, Inc., New York, 6th edition, 1945.

[59] W. Rider and D. B. Kothe. Reconstructing Volume Tracking. *Journal of Computational Physics*, 141:112–152, 2998.

[60] C. de Boor. *A Practical Guide to Splines.* Springer-Verlag New York Inc., New York, 1978.

[61] Suhas V. Patankar. *Numerical Heat Transfer and Fluid Flow.* Hemisphere Publishing Corporation, 1980.

[62] T. M. Shih, C. H. Tan, and B. C. Hwang. Effects of grid staggering on numerical schemes. *International Journal for Numerical Methods in Fluids*, 9:193–212, 1989.

[63] J. C. Tannehill, D. A. Anderson, and R. H. Pletcher. *Computational Fluid Mechanics and Heat Transfer.* Tayler & Francis, Washington DC, 2nd edition, 1997.

[64] T. L. Williams. An Implicit Surface Tension Model. Master thesis, Memphis University, Memphis, Tennessee, 1993.

[65] T. Y. Hou, S. J. S. Lowengrub, and M. J. Shelley. Removing the stiffness from interfacial flows with surface tension. *Journal of Computational Physics*, 114:312–338, 1994.

[66] R. Hoffman. A study of the advancing interface. I. Interface shape in liquid-gas systems. *Journal of Colloid Interface Science*, 50:228–241, 1975.

[67] E. B. Dussan V. On the spreading of liquids on solid surfaces: static and dynamic contact lines. *Annual Review of Fluid Mechanics*, 11:371–400, 1979.

[68] T. D. Blake. Kinetics of liquid/liquid displacement. *Journal of Colloid Interface Science*, 30:421–423, 1969.

[69] R. Aris. *Vectors, Tensors, and the Basic Equations of Fluid Mechanics.* Prentice-Hall, Inc., Englewood Cliffs, N.J., 1962.

[70] E. R. G. Eckert and Jr. Robert M. Drake. *Analysis of Heat and Mass Transfer.* McGraw-Hill Book Company, 1972.

[71] Wei Shyy. *Computational Modeling for Fluid Flow and Interfacial Transport.* ELSEWIER, New York, 1994.

[72] David Turnbull. Correlation of Liquid-Solid Interfacial Energies Calculated from Supercooling of Small Droplets. *Journal of Chemical Physics*, 18:768, 1950.

[73] David Turnbull. Kinetics of Solidification of Supercooled Liquid Mercury Droplets. *Journal of Chemical Physics*, 20(3):411–424, March 1952.

[74] Frans Spaepen and David Turnbull. Formation of Metallic Glasses. In *Rapid Quenched Metals, Second International Conference Section I, Ed. Grant and Giessen*, The Massachusetts Institute of Technology, 1976.

[75] Augusto Visintin. *Models of Phase Transition.* Birkhäuser, Boston Basel Berlin, 1996.

[76] C. A. Angell. Formation of Glasses from Liquids and Biopolymers. *Science*, 267: 1924, 1995.

[77] W. Kurz and D. J. Fisher. *Fundamentals of Solidification.* Trans Tech Publications Ltd., Switzerland, 1998.

[78] David A. Porter and Kenneth E. Easterling. *Phase Transformation in Metals and Alloys.* Van Nostrand Reinhold (UK) Co. Ltd., Molly Millars Lane, Wokingham, Berkshire, England, 1982.

[79] H. W. Bergmann and H. U. Fritsch. Kinetics and Morphology in Rapid Solidification. In *Rapidly Solidified Metastable Materials*, North-Nolland, New York, Amsterdam, Oxford, 1984.

[80] R. Willnecker, D. M. Herlach, and B. Feuerbacher. Evidence of Nonequilibrium Processes in Rapid Solidification of Undercooled Materials. *Physical Review Letters*, 62(23):2707–2710, June 1989.

[81] K. R. Castleman. *Digital Image Processing.* Prentice-Hall, Englewood Cliffs, N.J., 1996.

[82] R. C. Gonzalez and P. Wintz. *Digital Image Processing.* Addison-Wesley Publishing Company, Reading, Massachusetts, 1977.

[83] B. K. P. Horn. *Robot Vision.* The MIT Press and McGraw-Hill Book Company, Cambridge, Massachusetts and New York, 1986.

[84] E. R. Davies. *Machine Vision, THEORY, ALGORITHM, PRACTICALITIES.* Morgan Kaufmann, San Francisco, CA 94111, 3$^{\text{rd}}$ edition, 2005.

[85] S. J. Cummins, M. M. Francois, and D. B. Kothe. Estimating curvature from volume fractions. *Computers and Structures*, 2005.

[86] J. C. Martin and W. J. Moyce. An Experimental Study of the Collapse of Liquid Columns on a Rigid Horizontal Plane. *Philosophical Transactions of the Royal Society of London. Series A, Mathematical and Physical Sciences*, 244(882):312–324, March 1952.

[87] J. J. Stoker. *Water Waves.* Interscience, New York, 1957.

[88] D. K. Lynch. Tidal Bores. *Scientific American*, 247(4):146–157, October 1982.

[89] F. M. Henderson. *Open Channel Flow.* MacMillan, New York, 1966.

[90] C. H. Lin, J. F. Yen, and C. T. Tsai. Influence of Sluice Gate Contraction Coefficient on Distinguishing Condition. *Journal of Irrigation and Drainage Engineering*, 128 (4):252–249, August 2002.

[91] H. Chiriac, M. Tomut, and M. Grigorica. On the viscosity near the melting point of some liquid glass-forming transition metal alloys. *Journal of Non-Crystalline Solids*, 15B(205-207):504–507, 1996.

[92] Hermann Schlichting. *Boundary-layer theory.* McGraw-Hill, New York, 1979.

[93] Alec David Young. *Boundary Layers.* Blackwell Scientific, Oxford, England, 1989.

[94] R. L. Panton. *Incompressible Flow.* Wiley Interscience, New York, 2^{nd} edition, 1996.